

Computational Modelling Studies of Lithiated TiO₂ Nano-architected Structures at Different Temperatures, for Energy Storage Applications.

by

BLESSING NKATEKO RIKHOTSO

RESEARCH DISSERTATION

Submitted in fulfilment of the requirements for the degree of

MASTER OF SCIENCE

in

CHEMISTRY

in the

FACULTY OF SCIENCE AND AGRICULTURE

(School of Physical and Mineral Sciences)

at the

UNIVERSITY OF LIMPOPO

SUPERVISOR: Prof. P. E. Ngoepe

CO-SUPERVISOR: Dr. M.G. Matshaba

2019

DECLARATION

I declare that the thesis hereby submitted to the University of Limpopo, for the degree of Masters of Philosophy in Chemistry has not previously been submitted by me for a degree at this or any other University; that it is my work in design and in execution, and that all material contained herein has been duly acknowledged.

Rikhotso B. N

Date

DEDICATION

To my parents Laurence and Mervis Rikhotso, my four brothers, two sisters and most of all my son Ndzalo Nathan Mboweni.

ACKNOWLEDGEMENTS

There are many I have to be grateful for I must say that I could not have done it without their great support and love. I would like to express my heartfelt words of gratitude to Prof P.E Ngoepe for allowing me to study material sciences with my chemistry background. Your guidance and patience have help a lot over this years. It was a great honour for me to work with you and gained some of your deep knowledge in discussions and meetings. Your advice, inspiration and encouragement enabled me to enjoy all the scientific seminars, workshops and talks that were held in and out of Material Modelling Centre. I would also like to thank Dr. M.G. Matshaba for his extensive guidance throughout my study. Not forgetting Prof R.R. Maphanga and Prof H.R. Chauke for their advice and words of encouragement thank you.

To my beautiful, loving and courageous colleagues at Material Modelling Centre (MMC), where all my work was done. Your discussions have helped me a lot to achieve this degree. All thanks to the University of Limpopo community for providing a good working environment throughout my research study. All conferences that I have attended throughout my study have helped me a lot in contribution to my research work.

The Centre for High Performance Computing (CHPC) in Cape Town, I would like to say thank you for allowing me to use your systems throughout my research. All calculations of this work were done using their cluster systems, I really appreciate their help. I would like to acknowledge financial assistance from the National Research Foundation (NRF). Most of all, I thank Jesus Christ the son of God for giving me strength and guidance all this years. Not forgetting my mama and papa for being there for me when I needed them most. Your presence and support helped me a lot to achieve this degree.

ABSTRACT

Nano-architecture structures of Li_xTiO_2 are very promising as anode materials for lithium rechargeable batteries due to their ability to accommodate more lithium atoms and its ability to withstand high temperatures at atomistic level through charging and discharging. In these studies, we investigated how nano-architected structures of Li_xTiO_2 behave at high temperatures through the process of amorphisation and recrystallisation. A computational method of molecular dynamics (MD) simulation was employed to recrystallise the amorphous Li_xTiO_2 nano-architectures of bulk, nanosheet, nanoporous and nanosphere, where x depicts the fraction of lithium ions, i.e. 0.03, 0.04 and 0.07. The main objective of this study was to go beyond the previous inserted lithium atoms on TiO_2 and understand the effects of concentrations, temperature, defect chemistry and charge storage properties/capacity on the overall lithium transport to improve lithium ion battery performance.

Recrystallisation of all four nanostructures from amorphous precursors were successfully achieved and was followed by the cooling process towards 0 K and finally we heated all four nano-architectures at temperature intervals of 100 K up to 500 K. The variation of configuration energies as a function of time, was used to monitor the crystal growth of all nanostructures. Calculated Ti-O radial distribution function, were used to confirm the stability interaction after cooling. Calculated X-Ray Diffraction (XRD) spectra were used to characterise and compare their patterns at cooled and above high temperatures, using the model nanostructures, and they showed polymorphic nanostructures with Li_xTiO_2 domains of both rutile and brookite in accord with experiment. Amorphisation and recrystallization showed good results in generating complex microstructures. In particular, bulk structures show few zigzag tunnels (indicative of micro twinning) with 0.03 Li but 0.04 Li and 0.07 Li show complex

patterns indicating a highly defected structure. While 0.03 and 0.04Li nanospheres show, zigzag and straight tunnels in accord with experiment, the one with 0.07 Li has melted. Lastly, nanoporous and nanosheet structures have pure straight and zigzag patterns that are well in accord with our XRD patterns at all concentrations of lithium atoms and temperatures. The lithium transport was analysed using diffusion coefficient, calculated as a function of temperature in order to confirm the mobility above the given temperatures. An increase in temperature shows an increase in diffusivity of lithium at all lithium concentrations in nanoporous and nanosheet structures. The same trend was observed in bulk but only with 0.03 and 0.07 Li ion concentrations.

1 Contents

DECLARATION.....	i
DEDICATION.....	ii
ACKNOWLEDGEMENTS.....	iii
ABSTRACT.....	iv
List of Figures.....	viii
List of Tables.....	xiii
Chapter 1.....	1
1. Introduction.....	1
1.1 Structural Properties.....	3
1.1.1 Structural Description.....	3
1.1.2 Occurrence.....	5
1.2 Literature Review.....	6
1.2.1 Applications.....	6
1.2.2 TiO ₂ Nanostructures.....	6
1.3 Motivation.....	8
1.4 Objectives.....	10
2 Theoretical Background.....	11
2.1 Atomistic Simulation.....	11
2.1.1 DL_Poly Code.....	11
2.2 Potential Models.....	12
2.2.1 Short Range Two Body Potential Functions.....	12
2.2.2 Long Range Interaction.....	13
2.3 Molecular Dynamics.....	13
2.3.1 Integration Algorithms.....	17
2.3.2 Ensembles.....	18
2.3.3 Energy.....	19
2.3.4 Temperature.....	20
2.3.5 Pressure.....	23

2.3.6	Periodic Boundary Conditions	24
2.4	Simulation Properties	25
2.4.1	Radial Distribution Functions (RDFs)	26
2.4.2	Diffusion Coefficient.....	28
2.5	X- Ray Diffractions	29
2.5.1	Determination of Crystal Size:	30
2.5.2	Multiplicity and Systematic Absences.....	32
2.5.3	Correction Factors in Powder Diffraction	34
2.6	Amorphisation and Recrystallisation Technique.....	34
2.7	Lithiation of Nanostructures	37
2.7.1	Lithiation at Octahedral Sites.....	37
2.7.2	Lithium Insertion	39
3	Results.....	41
3.1	Methodology.....	42
3.1.1	Amorphisation and Recrystallisation of Li_xTiO_2 Nanostructures.	43
3.1.2	Crystal Growth on the Li_xTiO_2 Nanostructures.....	44
3.1.3	Cooled Nano-Architecture Structures of Li_xTiO_2	54
3.1.4	Temperature Variance of Li_xTiO_2 Nano-Architecture Structures.....	65
3.1.5	X-ray Diffraction Patterns.....	68
3.1.6	Microstructures	73
3.1.7	Transportation	79
3.2	Discussions	93
4	Conclusions and Recommendations	98
4.1	Conclusions.....	98
4.2	Recommendations.....	100
	References.....	101

List of Figures

FIGURE 1: THE THREE POLYMORPHS OF TiO_2 (A) ANATASE, (B) BROOKITE AND (C) RUTILE. 5	
FIGURE 2: ILLUSTRATION OF THE CONCEPT OF PERIODIC BOUNDARY CONDITIONS..... 25	
FIGURE 3: SCHEMATIC REPRESENTATION OF THE RADIAL DISTRIBUTION FUNCTION. 27	
FIGURE 4: REPRESENTS RDFs FOR TiO_2 BULK FROM SOLID, LIQUID AND GAS PHASES. 28	
FIGURE 5: SLICES THROUGH THE NANOSTRUCTURE SHOWING DIFFERENT TUNNEL CONFIGURATIONS. THE YELLOW CIRCLE INDICATES LITHIUM INSERTION SITE..... 38	
FIGURE 6: NANOSTRUCTURES OF TiO_2 (A) NANOSPHERE, (B) NANOSHEET, (C) NANOPOROUS AND (D) BULK 41	
FIGURE 7: AMORPHOUS NANOSPHERE STRUCTURES OF TiO_2 WITH (A) 0.03, (B) 0.04 AND (C) 0.07 LITHIUM ION CONCENTRATION AT 2000 K. 44	
FIGURE 8: RECRYSTALLISED NANOSPHERE STRUCTURES OF TiO_2 WITH (A) 0.03, (B) 0.04 AND (C) 0.07 LITHIUM ION CONCENTRATION AT 2000 K. 45	
FIGURE 9: AMORPHOUS NANOSHEET STRUCTURES OF TiO_2 WITH (A) 0.03, (B) 0.04 AND (C) 0.07 LITHIUM ION CONCENTRATION AT 2000 K. 45	
FIGURE 10: RECRYSTALLISED NANOSHEET STRUCTURES OF TiO_2 WITH (A) 0.03, (B) 0.04 AND (C) 0.07 LITHIUM ION CONCENTRATION AT 2000 K. 46	
FIGURE 11: AMORPHOUS NANOPOROUS STRUCTURES OF TiO_2 WITH (A) 0.03, (B) 0.04 AND (C) 0.07 LITHIUM ION CONCENTRATIONS AT 2000 K. 46	
FIGURE 12: RECRYSTALLISED NANOPOROUS STRUCTURES OF TiO_2 WITH (A) 0.03, (B) 0.04 AND (C) 0.07 LITHIUM ION CONCENTRATION AT 2000 K..... 47	
FIGURE 13: AMORPHOUS BULK STRUCTURES OF TiO_2 WITH (A) 0.03, (B) 0.04 AND (C) 0.07 LITHIUM ION CONCENTRATION AT 2000 K. 48	
FIGURE 14: RECRYSTALLISED BULK STRUCTURES OF TiO_2 WITH (A) 0.03, (B) 0.04 AND (C) 0.07 LITHIUM ION CONCENTRATION AT 2000 K. 48	

FIGURE 15: CALCULATED CONFIGURATION ENERGY AS A FUNCTION OF TIME AFTER RECRYSTALLISATION FOR TiO ₂ NANOSPHERE STRUCTURE WITH 0.03, 0.04 AND 0.07 LI ION CONCENTRATIONS.....	50
FIGURE 16: CALCULATED CONFIGURATION ENERGY AS A FUNCTION OF TIME AFTER RECRYSTALLISATION FOR TiO ₂ NANOSHEET STRUCTURE WITH 0.03, 0.04 AND 0.07 LI ION CONCENTRATIONS.....	51
FIGURE 17: CALCULATED CONFIGURATION ENERGY AS A FUNCTION OF TIME DURING RECRYSTALLISATION FOR TiO ₂ NANOPOROUS STRUCTURE WITH 0.03, 0.04 AND 0.07 LI ION CONCENTRATIONS.....	52
FIGURE 18: CALCULATED CONFIGURATION ENERGY AS A FUNCTION OF TIME AFTER RECRYSTALLISATION FOR TiO ₂ BULK STRUCTURE WITH 0.03, 0.04 AND 0.07 LI ION CONCENTRATIONS.....	54
FIGURE 19: COOLED NANOSPHERE STRUCTURES OF TiO ₂ WITH (A) 0.03, (B) 0.04 AND (C) 0.07 LITHIUM ION CONCENTRATIONS.....	55
FIGURE 20: COOLED NANOSHEET STRUCTURES OF TiO ₂ WITH (A) 0.03, (B) 0.04 AND (C) 0.07 LITHIUM ION CONCENTRATIONS.....	56
FIGURE 21: COOLED NANOPOROUS STRUCTURES OF TiO ₂ WITH (A) 0.03, (B) 0.04 AND (C) 0.07 LITHIUM ION CONCENTRATIONS.....	57
FIGURE 22: COOLED BULK STRUCTURES OF TiO ₂ WITH (A) 0.03, (B) 0.04 AND (C) 0.07 LITHIUM IONS.....	57
FIGURE 23: TOTAL RDFs FOR (A) Ti ³⁺ -O ²⁻ AND (B) Ti ⁴⁺ -O ²⁻ IN THE TiO ₂ NANOSPHERE WITH 0.03 LITHIUM ION CONCENTRATION AT DIFFERENT TEMPERATURES.....	58
FIGURE 24: TOTAL RDFs FOR (A) Ti ³⁺ -O ²⁻ AND (B) Ti ⁴⁺ -O ²⁻ IN THE TiO ₂ NANOSPHERE WITH 0.04 LITHIUM ION CONCENTRATIONS AT DIFFERENT TEMPERATURES.....	59

FIGURE 25: TOTAL RDFs FOR (A) $Ti^{3+}-O^{2-}$ AND (B) $Ti^{4+}-O^{2-}$ IN THE TiO_2 NANOSPHERE WITH 0.07 LITHIUM ION CONCENTRATIONS AT DIFFERENT TEMPERATURES.....	60
FIGURE 26: TOTAL RDFs FOR (A) $Ti^{3+}-O^{2-}$ AND (B) $Ti^{4+}-O^{2-}$ IN THE TiO_2 NANOSHEET WITH 0.03 LITHIUM ION CONCENTRATION AT DIFFERENT TEMPERATURES.....	60
FIGURE 27: TOTAL RDFs FOR (A) $Ti^{3+}-O^{2-}$ AND (B) $Ti^{4+}-O^{2-}$ IN THE TiO_2 NANOSHEET WITH 0.04 LITHIUM ION CONCENTRATION AT DIFFERENT TEMPERATURES.....	611
FIGURE 28: TOTAL RDFs FOR (A) $Ti^{3+}-O^{2-}$ AND (B) $Ti^{4+}-O^{2-}$ IN THE TiO_2 NANOSHEET WITH 0.07 LITHIUM ION CONCENTRATION AT DIFFERENT TEMPERATURES.....	622
FIGURE 29: TOTAL RDFs FOR (A) $Ti^{3+}-O^{2-}$ AND (B) $Ti^{4+}-O^{2-}$ IN THE TiO_2 NANOPOROUS WITH 0.03 LITHIUM ION CONCENTRATION AT DIFFERENT TEMPERATURES.....	622
FIGURE 30: TOTAL RDFs FOR (A) $Ti^{3+}-O^{2-}$ AND (B) $Ti^{4+}-O^{2-}$ IN THE TiO_2 NANOPOROUS WITH 0.07 LITHIUM ION CONCENTRATION AT DIFFERENT TEMPERATURES.....	633
FIGURE 31: TOTAL RDFs FOR (A) $Ti^{3+}-O^{2-}$ AND (B) $Ti^{4+}-O^{2-}$ IN THE TiO_2 BULK WITH 0.03 LITHIUM ION CONCENTRATION AT DIFFERENT TEMPERATURES.	644
FIGURE 32: TOTAL RDFs FOR (A) $Ti^{3+}-O^{2-}$ AND (B) $Ti^{4+}-O^{2-}$ IN THE TiO_2 BULK WITH 0.07 LITHIUM ION CONCENTRATION AT DIFFERENT TEMPERATURES.	644
FIGURE 33: STRUCTURAL CHANGES OF Li_xTiO_2 NANOSPHERE WITH X OF (A) 0.03, (B) 0.04 AND (C) 0.07 LI ION CONCENTRATION WITH TEMPERATURES AT 100, 300 AND 500 K.....	655
FIGURE 34: STRUCTURAL CHANGES OF Li_xTiO_2 NANOSHEET WITH X OF (A) 0.03, (B) 0.04 AND (C) 0.07 LI ION CONCENTRATION WITH TEMPERATURES AT 100, 300 AND 500 K.....	666
FIGURE 35: STRUCTURAL CHANGES OF Li_xTiO_2 NANOPOROUS WITH X OF (A) 0.03, (B) 0.04 AND (C) 0.07 LI ION CONCENTRATIONS WITH TEMPERATURES AT 100, 300 AND 500 K....	677
FIGURE 36: STRUCTURAL CHANGES OF Li_xTiO_2 BULK WITH X OF (A) 0.03, (B) 0.04 AND (C) 0.07 LI ION CONCENTRATION WITH TEMPERATURES AT 100, 300 AND 500 K.....	688

FIGURE 37: EXPERIMENTAL XRD PATTERNS FOR 1. TiO ₂ (A) NANORODS AND (B) Co (II) TiO ₂ [47] 2. PURE TiO ₂ (A) ANATASE (B) RUTILE (C) BROOKITE [22] 3. TiO ₂ : A-PbO ₂ . 4. TiO ₂ SPHERES, MESOPOROUS TiO ₂ SPHERES, AND MTO/MWCNT COMPOSITE	699
FIGURE 38: CALCULATED XRD PATTERNS FOR NANOSPHERE Li _x TiO ₂ (0.03 AND 0.07 LI ION CONCENTRATIONS) AT 0 AND 500 K.....	70
FIGURE 39: CALCULATED XRD PATTERNS FOR NANOSHEET Li _x TiO ₂ (0.03 AND 0.07 LI ION CONCENTRATIONS) AT 0 AND 500 K.....	71
FIGURE 40: CALCULATED XRD PATTERNS FOR NANOPOROUS Li _x TiO ₂ (0.03 AND 0.07 LI ION CONCENTRATIONS) AT 0 AND 500 K.....	722
FIGURE 41: CALCULATED XRD PATTERNS FOR BULK Li _x TiO ₂ (0.03 AND 0.07 LI ION CONCENTRATIONS) AT 0 AND 500 K.....	733
FIGURE 42: POLYMORPHIC CRYSTAL STRUCTURES OF BROOKITE (A,B), RUTILE (C,D), AND ANATASE (E), SHOWING THE ZIGZAG (BROOKITE) AND STRAIGHT (RUTILE) 1 × 1 TUNNELS. VIEWS DEPICT: (A) BROOKITE [100]; (B) BROOKITE [001]; (C) RUTILE [001]; (D) RUTILE [100]; (E) ANATASE [100].	744
FIGURE 43: MICROSTRUCTURES OF NANOSPHERE TiO ₂ AT 0 AND 500 K WITH A) 0.03, B) 0.04 AND C) 0.07 LI ION CONCENTRATIONS.....	755
FIGURE 44: MICROSTRUCTURES OF NANOSHEET TiO ₂ AT 0 AND 500 K WITH A) 0.03, B) 0.04 AND C) 0.07 LI ION CONCENTRATIONS.....	766
FIGURE 45: MICROSTRUCTURES OF TiO ₂ NANOPOROUS AT 0 AND 500 K WITH A) 0.03, B) 0.04 AND C) 0.07 LI ION CONCENTRATIONS.....	777
FIGURE 46: MICROSTRUCTURES OF BULK TiO ₂ AT 0 AND 500 K WITH A) 0.03, B) 0.04 AND C) 0.07 LI ION CONCENTRATIONS.	788
FIGURE 47: VARIATION OF Ti ³⁺ , Li, Ti ⁴⁺ AND O DIFFUSION COEFFICIENT WITH TEMPERATURE IN THE NANOSPHERE OF TiO ₂ WITH 0.03 LI ION CONCENTRATION.	799

FIGURE 48: VARIATION OF Ti^{3+} , Li, Ti^{4+} AND O DIFFUSION COEFFICIENTS WITH TEMPERATURES IN THE NANOSPHERE OF TiO_2 WITH 0.04 LI ION CONCENTRATION.	80
FIGURE 49: VARIATION OF Ti^{3+} , Li, Ti^{4+} AND O DIFFUSION COEFFICIENT WITH TEMPERATURE IN THE NANOSPHERE OF TiO_2 WITH 0.07 LI ION CONCENTRATION.	81
FIGURE 50: VARIATION OF Ti^{3+} , Li, Ti^{4+} AND O DIFFUSION COEFFICIENT WITH TEMPERATURE IN THE NANOSHEET TiO_2 WITH 0.03 LI ION CONCENTRATION.	822
FIGURE 51: VARIATION OF Ti^{3+} , Li, Ti^{4+} AND O DIFFUSION COEFFICIENT WITH TEMPERATURE IN THE NANOSHEET TiO_2 WITH 0.04 LI ION CONCENTRATION.	822
FIGURE 52: VARIATION OF Ti^{3+} , Li, Ti^{4+} AND O DIFFUSION COEFFICIENTS WITH TEMPERATURES IN THE NANOSHEET TiO_2 WITH 0.07 LI ION CONCENTRATION.	833
FIGURE 53: VARIATION OF Ti^{3+} , Li, Ti^{4+} AND O DIFFUSION COEFFICIENTS WITH TEMPERATURES IN THE NANOPOROUS TiO_2 WITH 0.03 LI ION CONCENTRATION.	844
FIGURE 54: VARIATION OF Ti^{3+} , Li, Ti^{4+} AND O DIFFUSION COEFFICIENTS WITH TEMPERATURES IN THE NANOPOROUS TiO_2 WITH 0.04 LI ION CONCENTRATIONS.....	855
FIGURE 55: VARIATION OF Ti^{3+} , Li, Ti^{4+} AND O DIFFUSION COEFFICIENTS WITH TEMPERATURES IN THE NANOPOROUS TiO_2 WITH 0.07 LI ION CONCENTRATIONS.	866
FIGURE 56: VARIATION OF Ti^{3+} , Li, Ti^{4+} AND O DIFFUSION COEFFICIENTS WITH TEMPERATURES IN THE BULK TiO_2 WITH 0.03 LI ION CONCENTRATIONS.....	866
FIGURE 57: VARIATION OF Ti^{3+} , Li, Ti^{4+} AND O DIFFUSION COEFFICIENTS WITH TEMPERATURES IN THE BULK TiO_2 WITH 0.04 LI CONCENTRATIONS.	877
FIGURE 58: VARIATION OF Ti^{3+} , Li, Ti^{4+} AND O DIFFUSION COEFFICIENTS WITH TEMPERATURES IN THE BULK TiO_2 WITH 0.07 LI ION CONCENTRATIONS.....	888
FIGURE 59: VARIATION OF LI DIFFUSION COEFFICIENT WITH TEMPERATURE IN THE NANOSPHERE, NANOSHEET, NANOPOROUS AND BULK TiO_2 INSERTED WITH 0.03 LI IONS.	899

FIGURE 60: VARIATION OF LI DIFFUSION COEFFICIENT WITH TEMPERATURE IN THE NANOSPHERE, NANOSHEET, NANOPOROUS AND BULK TiO_2 INSERTED WITH 0.04 LI IONS. 899

FIGURE 61: VARIATION OF LI DIFFUSION COEFFICIENTS WITH TEMPERATURES IN THE NANOSPHERE, NANOSHEET, NANOPOROUS AND BULK TiO_2 WITH 0.07 LI ION CONCENTRATIONS..... 90

FIGURE 62: VARIATION OF LI DIFFUSION COEFFICIENTS WITH TEMPERATURES IN THE NANOSPHERE TiO_2 WITH 0.03, 0.04 AND 0.07 LITHIUM ION CONCENTRATIONS. 90

FIGURE 63: VARIATION OF LI DIFFUSION COEFFICIENTS WITH TEMPERATURES IN THE NANOSHEET TiO_2 WITH 0.03, 0.04 AND 0.07 LITHIUM ION CONCENTRATIONS. 91

FIGURE 64: VARIATION OF LI DIFFUSION COEFFICIENTS WITH TEMPERATURES IN THE NANOPOROUS TiO_2 WITH 0.03, 0.04 AND 0.07 LITHIUM ION CONCENTRATIONS..... 922

FIGURE 65: VARIATION OF LI DIFFUSION COEFFICIENTS WITH TEMPERATURES IN THE BULK TiO_2 WITH 0.03, 0.04 AND 0.07 LITHIUM ION CONCENTRATIONS. 922

List of Tables

TABLE 1. STRUCTURE INFORMATION OF TiO_2 POLYMORPHS 4

TABLE 2: BUCKINGHAM POTENTIALS USED FOR LITHIATED TiO_2 42

Chapter 1

1. Introduction

Rechargeable battery technologies have been constantly improving to keep up with the huge advancements in performance of portable electronics, making it a heavily researched topic in the science community. The huge majority of batteries in portable electronics use lithium-based chemistry, the most common being lithium-ion (Li-ion). Li-ion batteries replaced the use of rechargeable nickel-cadmium batteries (Ni-Cad) in the late 20th century [1] with drastically higher capacities and reductions in weight. Li-ion batteries are generally mass-produced as button cells or as long metal cylinders (similar shape and size as an AA battery) which are stacked and inserted into battery packs like the one in our mobile phones. This packing gives an inefficiently low ratio of battery to volume; however, most of lithium-based batteries work on a chemical process where lithium ions (Li^+) move from the anode (positive electrode) to the cathode (negative electrode) through an electrolyte solution, releasing electricity to the circuit [2]. Thus powering your phone or tablet. During charging, the process is reversed and the anode absorbs the Li^+ ions. The number of Li^+ ions the anode can absorb essentially dictates the capacity of a battery. Almost all modern consumer-grade lithium batteries have anodes made out of graphite, with a highly regular surface to maximize absorption [3].

However, lithium batteries degrade over time, and this process speeds up at higher temperatures, especially by the ambient temperature increase caused by charging. (Not to mention actually using your device, which also generates heat.) That is why it is beneficial to use a low amperage charger for overnight charging, as faster charging causes a greater increase in battery temperature. This aging process is down to chemical and structural changes to the electrodes, one of which is the movement of

the Li^+ ions can over time damage the highly ordered surface of the electrodes [4]. Over time, the lithium salts that make up the electrolyte can crystallise on the electrodes, which can clog up the pores and prevent the uptake of Li^+ ions. The degradation of batteries are commonly being referred to as the “Coulombic efficiency”, describing the ratio of number of electrons extracted from the anode to the number of electrons able to be put in during charging. Usually a battery needs to have a coulombic efficiency of over 99.9% in order for it to be commercially viable [5].

A major concern with Li-ion is the risk of fire if they overload, overheat, short or puncture. Charging circuits in portable devices are designed to prevent the first three effects, but if they fail, it can be extremely dangerous [6] as it can cause heat build-up, which eventually starts a thermal runaway. Punctures are rare as batteries tend to be packaged inside the devices they are powering, but they are also a potential hazard [7]. Ventilation is one of the factor that sometimes overlooked. Ventilation is required to help dissipate heat generated by the battery, and can prevent the build-up of the flammable solvents if they were to leak, reducing the risk of an explosion [8]. TiO_2 occurs in nature as well-known mineral and recrystallises into three polymorphs such as rutile, anatase and brookite at temperatures range of 400 -1200 °C [9]. Rutile is stable under thermal treatment while anatase and brookite undergo a non-reversible phase transition into rutile when heated at high temperature ~ 500 – 550 °C[10].

Many successful materials consisting of one-dimensional nanostructures are reported in the recent literatures [11]. These structures have the potential to offer good conductivity, since they have contact with the rest of the nano-architecture energy storage applications. Various forms of TiO_2 are potential ideal host for reversible lithium insertion/removal, and are promising anode material for LIB's. In theory, TiO_2

can host many lithium and deliver a specific theoretical capacity of 330 m Ah/g (corresponding to the composition LiTiO_2 ~1mol of lithium) [12]. This study uses computer simulation method to investigate the performance of rechargeable Li-ion batteries, in particular the LiTiO_2 nano-structures. Furthermore, their performance at increased temperature was evaluated.

1.1 Structural Properties

1.1.1 Structural Description

Lithium (Li) is a chemical element with atomic number 3. It belongs to the alkali metal group in the periodic table of elements [13]. Lithium is also the lightest and least dense solid element (under standard conditions) with a soft silver-white appearance [14]. Like most alkali metals, lithium is highly reactive and flammable. Because of its high reactivity, lithium never occurs freely in nature; instead, it appears only in compounds [15]. The most significant properties of lithium are its high specific heat (calorific capacity), huge temperature interval in the liquid state, high thermic conductivity, low viscosity and very low density [16].

Titanium dioxide has eight modifications – in addition to rutile, anatase, and brookite, three metastable phases can be produced synthetically (monoclinic, tetragonal and orthorhombic), and five high-pressure forms (α - PbO_2 -like, baddeleyite-like, cotunnite-like, orthorhombic OI, and cubic phases) also exist:

Table 1. Structure information of TiO₂ polymorphs

Crystal form	Space group	Density	Synthesis method	Lithiation amount at bulk	Lithiation amount at nano
Anatase	Tetragonal, I41/amd	3.79	–	0.5	1.0
Rutile	Tetragonal, P42/mnm	4.13	–	0.1	0.85
Brookite	Orthorhombic, Pbca	3.99	–	–	1.0
TiO ₂ (B), bronze[17]	Monoclinic, C2/m	3.64	Hydrolysis of K ₂ Ti ₄ O ₉ followed by heating	0.71	1.0
TiO ₂ (H), hollandite-like form[18]	Tetragonal, I4/m	3.46	Oxidation of the related potassium titanate bronze, K _{0.25} TiO ₂	–	–
TiO ₂ (R), ramsdellite-like form[19]	Orthorhombic, Pbnm	3.87	Oxidation of the related lithium titanate bronze Li _{0.5} TiO ₂	–	–
TiO ₂ (II)-(α-PbO ₂ -like form_[20]	Orthorhombic, Pbcn	4.33	High pressure	–	–
TiO ₂ (III) (baddeleyite-like form, 7 coordinated Ti) [21]	Monoclinic	–	High pressure	–	–
TiO ₂ -OI[22]	Orthorhombic	–	High pressure	–	–
Cubic[23]	Cubic	–	P>40 GPa, T>1600 °C	–	–
TiO ₂ –OII (PbCl ₂ -like, 9 coordinated Ti) [24]	Orthorhombic	–	P>40 GPa, T>700 °C	–	–

The cotunnite-type phase was claimed by L. Dubrovinsky and co-authors to be the hardest known oxide with the Vickers hardness of 38 GPa and the bulk modulus of 431 GPa (i.e. close to diamond's value of 446 GPa) at atmospheric pressure. However, later studies came to different conclusions with much lower values for both the hardness (7–20 GPa, which makes it softer than common oxides like corundum Al₂O₃ and rutile TiO₂) [25] and bulk modulus (~300 GPa). [26]

The oxides are commercially important ores of titanium. The metal can also be mined from other minerals such as ilmenite or leucosene ores, or one of the purest forms, rutile beach sand. Star sapphires and rubies get their asterism from rutile impurities present in them [27].

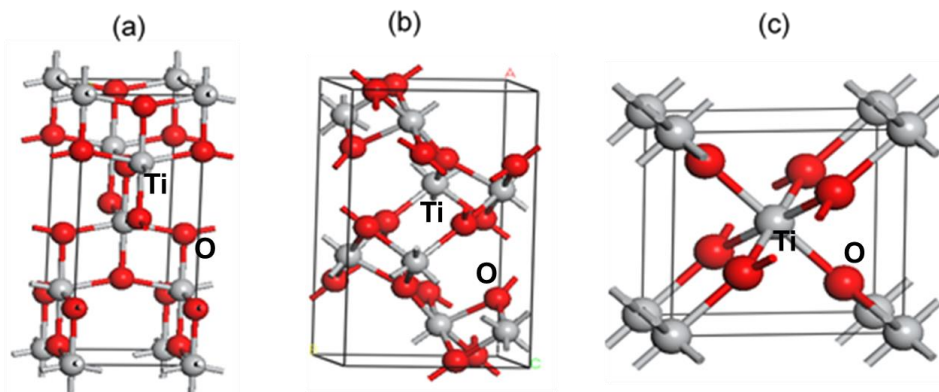


Figure 1: The three polymorphs of TiO_2 (a) Anatase, (b) Brookite and (c) Rutile.

1.1.2 Occurrence

Titanium dioxide occurs in nature as the well-known minerals rutile, anatase and brookite, and additionally as two high pressure forms, a monoclinic baddeleyite-like form and an orthorhombic $\alpha\text{-PbO}_2$ -like form, both found recently at the Ries crater in Bavaria. One of these is known as akaogiite and should be considered as extremely rare mineral [28]. It is mainly sourced from ilmenite ore. This is the most widespread form of titanium dioxide-bearing ore around the world. Rutile is the next most abundant and contains around 98% titanium dioxide in the ore. The metastable anatase and brookite phases convert irreversibly to the equilibrium rutile phase upon heating above temperatures in the range 600-800 °C (1,112-1,472 °F) [29] Titanium dioxide (B) is found as a mineral in magmatic rocks and hydrothermal veins, as well as weathering rims on perovskite. TiO_2 also forms lamellae in other minerals [30].

1.2 Literature Review

1.2.1 Applications

Titanium dioxide have a wide range of applications due to its wide band gap of 3.2 eV (ref) and structural characteristics [1]. Applications such as photo-catalysis[2], photo-splitting of water [3], photochromic devices [4], insulators in metal oxide [5], semiconductors devices [6], dye sensitized solar cells (DSSCs) (energy conversions) [7], rechargeable lithium batteries (electrochemical storage) [8]. Previously the demand of renewable energy has exhibited lithium ion batteries (LIB) to be regarded as energy storage applications in portable devices and electric vehicles [9]. TiO_2 has being recognized as one of the anode active material in LIBs [10] since is one of the most promising anode candidates for LIBs. The anode material plays an important part in LIBs therefore; we have to study the most important factors of TiO_2 for the enhancement of the battery. A good anode material must have cycling stability [11], good rate capability [12], a high specific surface area and more channels to accommodate lithium ions [13]. These points are very much important for large-scale batteries for applications in electric vehicles since they require high safety, environmentally friendly and inexpensive [13] [14]. TiO_2 has limitations such as low capacity and poor rate capability [9]. Applications of TiO_2 depends on the size, shape and polymorphs of TiO_2 [3] [4] [7].

1.2.2 TiO_2 Nanostructures

Nanostructures of TiO_2 have created a lot of interest in various application due to their different forms and surface energy. Applications such as bio-safety and health [15], LIB and supercapacitor [16] [17]. Recently nanostructures of TiO_2 such as nanosphere [18], nanorods [19], nanowires [20], nanowhiskers [21], nanoporous [22],

nanosheet [23] and nanosizing [24] have been studied for different applications with different methods.

Nanoparticles TiO_2 is more effective as a photocatalyst compared to the bulk parent material [4]. In particular, when the diameter of the crystallites of a semiconductor particle falls below a critical radius of about 10 nm, each charge carrier behaves quantum mechanically [5]. Lithium insertion into nanoparticles of other TiO_2 common polymorphs, such as rutile and brookite, was not well known until very recently, when a high Li electroactivity was reported in nanometer sized rutile and brookite TiO_2 at room temperature [25][26]. It was noticed that crystalline size of brookite TiO_2 has effect on lithium intercalation [27].

Bulk rutile TiO_2 and its (110) surface have been investigated with a computationally efficient semi empirical tight binding method [28]. However, the study have not reported on interatomic parameters for this system or its bulk. The anatase phase of bulk structure of TiO_2 has been preferred for lithium intercalation than the brookite [26]. More structural features must be studies so that we can have a clear understanding of which polymorphs can accommodate more lithium atoms.

Various authors for different applications have studied Nanoporous [29] [30]. It has reported that nanoporous has a good electrochemical performance due to its large surface area [22]. Nanoporous has been studied with an ordered structure and it shows enhanced photocatalytic activity [31]. Large-scale preparation of nanoporous have shown the anatase TiO_2 porous morphology with the diameter of 20nm.

Nanosheets in an anatase phase has an improved photoelectric conversion efficiency [9]. They also reported the nanosheets with facet and its applications for solar cells [31]. The energy storage, conversion and catalytic activities of TiO_2 nanosheets are a

more recent area of study compared to nanoparticulate and nanoporous TiO₂ because the exposure of highly reactive surfaces renders the nanosheets unstable during crystal growth [32]. Nanosheets of TiO₂ comprising mixed polymorphic phases (brookite with anatase and rutile) are easier to synthesise than pure brookite and were found to be photoactive, particularly for photo-oxidation reactions in solid-liquid and gas-solid systems [32].

TiO₂ nanoparticles have been studied for high-pressure crystallisation where they generated full atomistic model of a TiO₂ nanocrystal [33]. Their simulation technique has been used to study various nanostructures of TiO₂ [77]. We will lithiate those nanostructures with different lithium concentrations and study their structural features, at varied temperature.

1.3 Motivation

The literature review in section 1.2 has clearly indicated the significance of energy storage for different applications, particularly its demand for vehicle traction recently. TiO₂ with high Li concentrations are being considered as one of the most attractive anode materials of LIBs owing to distinct characteristics, which have been outlined, as compared to some of the existing commercial anode materials such as graphite. The advantages of the various TiO₂ nano-architectures have been clearly elucidated, and in order to maximise their usage in enhancing the rate capability and energy density their further fundamental understanding is necessary.

Future chemical energy storage applications, ranging from portable consumer products to hybrid and plug-in electric vehicles to electrical distribution load levelling, require vivid outcome of deep discharge with subsequent recharging (charge-discharge cycles). Battery design developments for a low-cost, high volume synthesis

and fabrication techniques for nano composites, need to be improved to elevate the safety characteristics for their use in Li-ion battery.

The level of usage must occur with minimal loss of performance so that the same capacity is available on every discharge, in particular with minimal capacity fade. The requirements of ensuring stable cycle-life response have been limited by the utilisation of the electrodes and the amount of energy that could be available from the batteries during charge/discharge reaction. Nano-architected materials have been attracting an increasing amount of attention in the science community due to their unique physical and chemical properties [63]. These nanomaterials have large surface-to-volume ratios and interfaces (between the electrode and electrolyte).

Nano-architected materials also offer the ability to advance the properties of materials or improve new properties by simply adjusting their size. Lithiated TiO_2 is of considerable technological and scientific interest because of its ability to be controlled at a nano scale and its size add a functional variable in composition and structure. The low temperatures that were applied in previous studies have enabled batteries not to last longer through decreased ion mobility, hence it is necessary to investigate the effect of ambient and high temperatures on a recrystallised and cooled structures of LiTiO_2 . The diffusion coefficient, radial distribution functions and energy profiles were calculated to understand the mobility of ions, melting points and the effect of lithium concentration in the recrystallised structures of LiTiO_2 nanostructures.

In the proposed study, simulated amorphisation recrystallisation method will be employed to generate nano-architectures of TiO_2 , i.e. nanosphere, nanoporous, nanosheet and bulk structures which have been widely studied experimentally. Such structures will be lithiated and characterized to understand the fundamentals of

atomistic structural and microstructural details that are crucial for enhancement of energy density. The impact of high temperature on structural aspects, XRDs and microstructures will be explored, as well as lithium transport which are all related to energy density, power, charge discharge time and number of charge/discharge cycles of high power rechargeable batteries.

1.4 Objectives

Molecular dynamics simulations technique will be used to explore Li transport in amorphous and recrystallised TiO₂ nanosphere, nanosheet, nanoporous and bulk structures with an aim of obtaining atomic insights into the structural response at increase temperatures and different Li ion concentrations. By

- i. evaluating the effect of lithiation on crystallisation of TiO₂ nano-architected structures at different Li ion concentrations through amorphisation and recrystallization process,
- ii. monitoring the behaviour of the recrystallized lithiated TiO₂ nano-architected structures after being cooled from 1500 to 0 K,
- iii. Investigating structural changes of Li_xTiO₂ nano-architected after being heated to high (500 K) temperatures from low (0 K) temperature conditions,
- iv. Determining the reliability and performance of Li_xTiO₂ by viewing microstructures and calculating its X-ray diffraction patterns and diffusion coefficient for battery anode electrode at different temperatures.

Chapter 2

2 Theoretical Background

In this chapter, we present the method that was used throughout the study. We describe the simulation code that was employed, potential models used and the simulated amorphisation and recrystallisation technique that was used to allow the spontaneous growth of titanium dioxide nanostructures. We will present the discussion of the potential models for atomic simulation technique since it was the only technique that was employed throughout this work. Some potential models were not used like shell model, since it is a sub-potentials of Buckingham potential. Shell model is computationally very expensive preventing simulation of large systems, such as a mesoporous TiO₂ host. Moreover, the potentials become unstable at high temperatures leading to potential catastrophic failure.

2.1 Atomistic Simulation

Computer simulation of matter with atomistic detail has become a very prominent tool in chemistry, physics, life sciences and material sciences. In this field, simulation results yield the insights needed to interpret experimental measurements that can be used to predict material properties or to design new compounds.

2.1.1 DL_Poly Code

Molecular dynamics simulations were all performed using the computer code DL_POLY [64]. DL_POLY is a general-purpose molecular dynamics simulation package continually developed at Daresbury Laboratory by W. Smith and I. T. Todorov under the auspices of EPSRC and NERC in the support of CCP5. It simulates a wide variety of molecular systems of ionic liquids and solids, simple liquids, small polar and non-polar molecular systems, bio- and synthetic polymers, ionic polymers and glasses

solutions, simple metals and alloys. In this work, we used this code to simulate the nanostructures of titanium dioxide. The input files for DL_POLY are CONTROL, FIELD and CONFIG, which helps us to carry our calculations together with the run script. These mandatory files must be present in the directory when DL_POLY is to run. CONTROL - this file specifies the control conditions for a run of the program. In this file, we specify time step, temperature, pressure, ensemble, Ewald precision etc. FIELD– defines the force field for the simulation and details of the molecular structures. CONFIG – defines the positions of all the atoms in the system (in Angstroms) and specifies the simulation cell. It also specifies the atomic velocities and forces.

2.2 Potential Models

Calculations are based on the Born model [65] of ionic solids, where ions interact via long-range Coulomb and short range interactions. Rigid ion potentials with partial charges were used and Matsui developed these for isostructural rutile TiO₂. In this section, we are going to describe the potential models.

2.2.1 Short Range Two Body Potential Functions

The short-range two body potentials are an interaction between two charge clouds. That is the short-range attractive and repulsive interactions of the ions. Attractive interaction contains van der Waals. The short-range interaction energies are described well by simple parameterised analytical functions. Below we give descriptions of short-range interactions potentials.

2.2.1.1 Buckingham Potentials

Buckingham potential is a formula that describes the van der Waals energy Φ_{ijl} for the interaction of two atoms that are indirectly bonded as a function of the interatomic distance l . It is used to model two body non-bonded interactions in ionic solids. The

general form of Buckingham potential is given by

$$\Phi_{ij}(r) = A_{ij} \exp \frac{-r_{ij}}{\rho_{ij}} - \frac{C_{ij}}{r_{ij}^6} \quad 2.1$$

Where A_{ij} is the size of the ions, ρ_{ij} is the hardness and C_{ij} is the dispersion parameter. The repulsive interaction between the ions is represented by the first term while the second term is the van der Waals attractive interaction of the ions.

2.2.2 Long Range Interaction

The long-range interaction energy is the sum of interaction energies between the charges of a central unit cell and all the charges of the lattice. The long range interaction energy of two ions (ion i and ion j) with charges q_i and q_j is given by

$$\Psi(r_{ij}) = \sum \frac{q_i q_j}{4\pi\epsilon_0 (r_{ij} + l)} \quad 2.2$$

Where r_{ij} is the displacement separating the two ions, ϵ_0 is the permittivity of free cell and l is the set of lattice vectors representing the periodicity of the crystal lattice. In particular, long-range interactions describe the Coulombic summation.

2.3 Molecular Dynamics

Molecular dynamics simulation is a computational technique used to study the motions of atoms in a given system (e.g. a solid material or a solid solution could equally be liquids and gases) in order to understand and predict the structural , dynamic, kinetic, and /or equilibrium properties at a chosen conditions (e.g. compositions, temperatures and pressures) [66]. Molecular dynamics (MD) is a powerful method for exploring the structure of solids, liquids and gases. It is a modern method, which requires electronic computers and recently supercomputers. Molecular dynamics simulations are in many respects very similar to real experiments. When we perform a real experiment, we proceed as follows. We prepare a sample of the material that we wish to study. We connect this sample to a measuring instrument (e.g. a thermometer, manometer, or

viscometer), and we measure the property of interest during a certain time interval. If our measurements are subject to statistical noise (as most measurements are), then the longer we average, the more accurate our measurement becomes. In molecular dynamics simulation, we follow exactly the same approach. First, we prepare a sample: we select a model system consisting of N particles and we solve Newton's equations of motion for this system until the properties of the system no longer change with time (we equilibrate the system).

After equilibration, we perform the actual measurement. In fact, some of the most common mistakes that can be made when performing a computer experiment are very similar to the mistakes that can be made in real experiments (e.g., the sample is not prepared correctly, the measurement is too short, the system undergoes an irreversible change during the experiment, or we do not measure what we think) [67]. We call molecular dynamics (MD) a computer simulation technique where the time evolution of a set of interacting atoms is followed by integrating their equations of motion. The molecular dynamics can be used to investigate the detailed atomistic mechanisms. With MD technique, it is possible to simulate the dynamic, thermal behavior of atoms in solids. By performing simulations at different temperatures and studying the displacements of the ions as a function of time we can predict diffusion coefficients. The molecular dynamics technique involves solving Newton's laws of motion over a finite period for all the particles of a system. The main difference with the energy minimization method discussed in the previous section, is that, molecular dynamics simulation gives the effect of temperature by assigning kinetic energy to the atoms in the simulation cell and thus allows us to follow the trajectory of the atoms and molecules with time. Hence, unlike in energy minimization calculations, atoms and molecules can potentially jump over energy barriers to reach a global minimum;

however, due to the very short ‘real time’ accessible to molecular dynamics simulations, this only applies to small energy barriers, i.e., of the order of few $k_B T$. All molecular dynamics simulations in this work was performed using the computer code DL_POLY developed by W. Smith and T.R. Forester in Daresbury, UK [68]. In molecular dynamics simulation, the particles are initially assigned random velocities, such that the system starts with the required temperature and that the simulation cell has no translational momentum, i.e,

$$\sum_{i=1}^N m_i \cdot v_i^2 = 3Nk_B T \quad (2.3)$$

and

$$\sum_{i=1}^N m_i \cdot v_i = 0 \quad (2.4)$$

where N is the number of particles, k_B is the Boltzmann constant, T is the temperature, m_i is the mass of ion i , and v_i its velocity.

The second step of a molecular dynamics simulation is to calculate the force acting on each particle. Once the forces, F_i are obtained the accelerations, a_i can be calculated and the velocities, v_i and positions F_i , are updated, for an infinitely small time step, according to

$$a_i(t) = \frac{F_i(t)}{m_i} \quad (2.5)$$

$$v_i(t + \delta t) = v_i(t) + a_i(t) \cdot \delta t \quad (2.6)$$

$$r_i(t + \delta t) = r_i(t) + v_i(t) \cdot \delta t \quad (2.7)$$

These are the Newton's equations of motion and can only be applied strictly for an infinitesimal time step. In practice, computer codes use integration algorithms such as the Verlet algorithm [69] to solve Newton's laws of motion, as explained in the next section. The choice of the time step δt , in these equations is very important. Indeed, if δt is too large, the molecular vibrations will occur within the time step, giving rise to large errors. However, if δt is too small, the particles will take too long to move a significant distance. In addition, another factor needs to be considered to choose the time factor. After each step, run time properties such as the potential energy, the temperature, or the pressure of the system are calculated. Then the process is repeated several thousand or million times to reach the required simulation time. In the first few tens of thousands steps, the particles' velocities are scaled to meet the desired temperature. This period is the equilibrium period and it allows the system to come to equilibrium at a given temperature and pressure before data are collected. Then, the simulation runs as long as possible, without scaling the particles' velocities, to obtain converged averages of the properties of interest and reduce statistical noise.

In molecular dynamics, we follow the laws of classical mechanics, and most notably Newton's law of motion:

$$\vec{F}_i = m_i \vec{a}_i \quad (2.8)$$

for each atom i in a system constituted by N atoms. Here, m_i is the atom mass, $\vec{a}_i = \frac{d^2 \vec{r}_i}{dt^2}$ its acceleration, and \vec{F}_i the force acting upon it, due to the interactions with other atoms.

In the next section we discuss the integration algorithm, the different types of ensembles used in this work and we will discuss the properties that are calculated

from molecular dynamics simulations i.e. Radial distribution functions, diffusion coefficients and mean squared displacement.

2.3.1 Integration Algorithms

An integration algorithm is used to perform the systematic solution of the equations of motion using a finite difference algorithm. The algorithm used in this work is the Verlet algorithm. The positions, velocities as well as accelerations are obtained by a Taylor expansion of the positions about time t :

$$\begin{aligned}
 r(t + \delta t) &= r(t) + v(t)\delta t + \frac{1}{2}a(t)\delta t^2 + \frac{1}{6}b(t)\delta t^3 + \dots \\
 v(t + \delta t) &= v(t) + a(t)\delta t + \frac{1}{2}b(t)\delta t^2 + \dots \\
 a(t + \delta t) &= a(t) + b(t)\delta t + \dots \\
 b(t + \delta t) &= b(t) + \dots
 \end{aligned} \tag{2.9}$$

where r is the particle's position, v is the velocity, a is the acceleration and b is the third time derivative of r . From equation, $r_{n+1} = r_n - g_n \cdot H_n$ (i) we can calculate the position of a particle about a position $r(t)$ before and after a time step δt

$$r(t + \delta t) = r(t) + v(t)\delta t + \frac{1}{2}a(t)\delta t^2 + \frac{1}{6}b(t)\delta t^3 + \mathcal{O}(\delta t^4) \tag{2.10}$$

$$r(t - \delta t) = r(t) - v(t)\delta t + \frac{1}{2}a(t)\delta t^2 - \frac{1}{6}b(t)\delta t^3 + \mathcal{O}(\delta t^4) \tag{2.11}$$

where $\mathcal{O}(\delta t^4)$ is the order of accuracy. Now adding

$$H_{n+1} \approx H_n + \frac{\delta r \times \delta r^T}{\delta r^T \cdot \delta g} - \frac{(H_n \cdot \delta g) \times (H_n \cdot \delta g^T)}{\delta g^T \cdot H_n \cdot \delta g} \tag{ii}$$

and

$$H_{n+1} \approx H_n + \frac{\delta r \times \delta r}{\delta r \cdot \delta g} - \frac{(H_n \cdot \delta g) \times (H_n \cdot \delta g)}{\delta g \cdot H_n \cdot \delta g} + (\delta g \cdot H_n \cdot \delta g) u \times u \quad (\text{iii})$$

gives

$$r(t + \delta t) + r(t - \delta t) = 2r(t) + a(t)\delta t^2 + \mathcal{O}(\delta t^4) \quad (2.12)$$

We notice that Verlet algorithm is time-reversible (i.e. $r(t + \delta t)$ and $r(t - \delta t)$ are interchangeable). Also, the absence of velocities, since they are not required but are necessary for the calculation of the kinetic energy. They can be calculated by subtracting Equation (ii) from (iii) and obtain:

$$v(t) = \frac{r(t + \delta t) - r(t - \delta t)}{2\delta t} + \mathcal{O}(\delta t^2) \quad (2.13)$$

Equation (2.12) is accurate to δt^4 while Equation (2.13) is accurate to order δt^2 .

2.3.2 Ensembles

Integrating Newton's equations of motion allows you to explore the constant energy surface of a system. However, most natural phenomena occur under conditions where the system is exposed to external pressure and/or exchanges heat with the environment. Under these conditions, the total energy of the system is no longer conserved and extended forms of MD are required. Several methods are available for controlling temperature. Depending on which state variables the energy, E, enthalpy, H (i.e., E + PV), number of particles, N, pressure, P, stress, S, temperature, T, and volume, V – are kept fixed, different statistical ensembles can be generated. A variety of structural, energetic, and dynamic properties can then be calculated from the averages or the fluctuations of these quantities over the ensemble generated. There are three most common ensembles that are often used in MD simulations NVT, NVE

and NPT ensembles. NVT ensemble is also known as canonical ensemble where temperature and volume are kept constant. NVT ensemble in statistical mechanics is a statistical ensemble representing a probability distribution of microscopic states of the system. For a system taking only discrete values of energy, the probability distribution is characterized by the probability of finding the system in a particular microscopic state with energy level, conditioned on the prior knowledge that the total energy of the system and reservoir combined remains constant. NVE ensemble is also known as micro canonical ensemble where energy and volume are kept constant. NVE ensemble is obtained by solving the standard Newton equation without any temperature and pressure control. Energy is conserved when this (adiabatic) ensemble is generated. However, because of rounding and truncation errors during the integration process, there is always a slight fluctuation, or drift, in energy. NPT ensemble is also known as isothermal-isobaric ensemble. This ensemble plays an important role in chemistry as chemical reactions are usually carried out under constant pressure condition. In NPT ensemble, pressure and temperature are kept constant. The NPT ensemble is used for comparison of MD simulations with experiments. Temperature in NPT ensemble is controlled using Langevin method. The partition function can be written as the weighted sum of the partition function of canonical ensemble, $Z(N, V, T)$.

$$\rho(N, P, T) = \int Z(N, V, T) e^{(-\beta PV)CdV} \quad 2.14$$

Where $\beta = \frac{1}{k_B T}$ 2.15

k_B is the Boltzmann constant and V is the volume of the system.

2.3.3 Energy

The internal energy is easily obtained from a simulation as the ensemble average of the energies of the states that are examined during the course of the simulation:

$$U = \langle E \rangle = \frac{1}{M} \sum_{i=1}^M E_i \quad 2.16$$

The average potential energy V is obtained by averaging its instantaneous value, which is obtained at the same time as the force computation is made. Thus, the potential energy is given by:

$$V(t) = \sum_i \sum_{j>1} \phi (|r_i(t) - r_j(t)|) \quad 2.17$$

The kinetic energy is given by:

$$K(t) = \frac{1}{2} \sum_i m_i [\bar{v}_i(t)]^2 \quad 2.18$$

Where m_i is the mass of atom i and \bar{v}_i is the velocity of atom i . The total energy of the system can be represented as the sum of the kinetic energy and the potential energy and the total energy of the system with a given set of positions and velocities is represented by:

$$T_{tot} = K(t) + V(t) \quad 2.19$$

2.3.4 Temperature

Temperature depends on a certain kind of ensemble for a particular simulation. In a canonical ensemble, the total temperature is constant whereas in the micro canonical ensemble the temperature is fluctuating. The temperature is directly related to the kinetic energy of the system as follows:

$$K = \sum_{i=1}^N \frac{|\dot{p}_i|^2}{2m_i} = \frac{k_B T}{2} (3N - N_c) \quad 2.20$$

Where p_i is the total momentum of particle i , m_i is its mass and N_c is the number of constraints on the system. Each degree of freedom contributes $k_B T/2$ this is according to the equipartition of energy. If there are N particles, each with three degrees of freedom, then the kinetic energy should be equal to $3Nk_B T/2$. Total linear momentum of the system is often constrained to a value of zero in a molecular dynamics simulation, which has the effect of removing three degrees of freedom from the system and N_c

would be equal to 3.

2.3.4.1 Melting Temperature

Melting temperature is defined as the temperature at which, under a specific pressure, the liquid and solid phases of a substance coexist in equilibrium. At melting the systems appear disordered, molecular diffusion can occur, and it is a high-pressure case. At low temperatures, systems are ordered with little molecular motion and that occurs at low pressures. The melting temperature of most substances is the same as their freezing temperature because the substance melts at a similar temperature as that at which it freezes. The example is that of the most interesting liquid, water, which melts very close to 0 °C (273.15 K). Coexistence is easily achievable in larger systems in two dimensions. Unlike the boiling point, the melting temperature is relatively insensitive to pressure. Melting points are often used to characterise organic compounds and ascertain the purity. The melting point of a pure substance is always higher and has a smaller range than the melting point of an impure substance.

The more impurity is present, the lower the melting point and the broader the range. The chemical element with the highest melting point is tungsten which melts at 3695 K (3422 °C) making it excellent for use in light bulbs. Platinum, with the melting point of 1772 °C (2045.15 K), has the highest melting point amongst the precious metals while metallic gold melts at 1064 °C (1337 K). Computationally we are able to keep the pressure and temperature constant while allowing the energy to fluctuate until a stable value is reached. Not only is heat required to raise the temperature of the solid to the melting point, but also the melting itself requires heat called the heat of fusion. From thermodynamics, at the melting point the change in Gibbs free energy (ΔG) of the material is zero, because the enthalpy (H) and the entropy (S) of the material are increasing ($\Delta H, \Delta S > 0$). Melting phenomena happens when the Gibbs free energy of

the liquid becomes lower than the solid for that material. Carnelley's rule established in 1882 by Thomas Carnelley states that high molecular symmetry is associated with high melting point. A good example is that of three structural isomers with molecular formula C_5H_{12} where the melting point increases in the series: isopentane 113 K, n-pentane 143 K and neopentane 255 K. Pyridine has a lower symmetry than benzene hence its lower melting point. A high melting point results from a high heat of fusion or low entropy of fusion or a combination. In highly symmetrical molecules, the crystal phase is densely packed with many efficient intermolecular interactions resulting in a higher enthalpy change on melting.

2.3.4.2 Annealing process

Annealing is a heat treatment in which a material is exposed to an elevated temperature for an extended time and then slowly cooled down. It is regarded as the toughening process and prevents the creation of defects in the atomic scale as defects like vacancies; misplacement, etc. can really hurt the strength of material. In the glass factory, it is extremely important to anneal, the glass before it is ready or else it will be very fragile and even removing it from its mould will be impossible. Glasses, which are not properly annealed will contain stress, which may result in breakage before or at any time subsequent to their removal from the kiln. Annealing is critical to the longevity of glass.

Annealing is also used as an optimisation tool in finding the global minima. Another important application is to relieve internal stress, refine the structure and improve cold working properties. There are three stages in the annealing process, with the first being the recovery phase, which results in softening of the metal through removal of crystal defects and the internal stresses that they cause. The second phase is recrystallization, where new grains nucleate and grow to replace those deformed by

internal stresses. If annealing is allowed to continue once recrystallization has been completed, grain growth will occur, in which the microstructure starts to coarsen and may cause the metal to have less than satisfactory mechanical properties. The high temperature of annealing may result in oxidation of the surface of the metal, resulting in scale. If scale is to be avoided, annealing is carried out in an oxygen, carbon, and nitrogen free atmosphere. In thermodynamics, annealing occurs by diffusion of atoms within a solid material, so that the material progresses towards its equilibrium state.

2.3.5 Pressure

Calculation of pressure is usually in a computer simulation via the virial theorem of Clausius. The virial is defined as the expectation value of the sum of the products of the coordinates of the particles and the forces acting on them. Usually this is written as

$$W = \sum x_i \dot{p}_{x_i} \quad 2.21$$

Where x_i is a coordinate (e.g. the x or y coordinate of an atom) and \dot{p}_{x_i} is the first derivative of the momentum along that coordinate (\dot{p}_i is the force, by Newton's second law). The virial theorem states that the virial is equal to $-3Nk_B T$. In an ideal gas, the only forces are those due to interactions between the gas and the container and it can be shown that the virial in this case equal to $-3PV$. This result can be obtained directly from

$$PV = Nk_B T \quad 2.22$$

Forces between the particles in a real gas or liquid affect the virial, and thence the pressure. The total virial for a real system equals the sum of an ideal gas part ($-3PV$) and a contribution due to interactions between the particles. The result obtained is:

$$W = -3PV + \sum_{i=1}^N \sum_{j=i+1}^N r_{ij} \frac{dv(r_{ij})}{dr_{ij}} = -3Nk_B T \quad 2.23$$

If $d \frac{dv(r_{ij})}{dr_{ij}}$ is written as f_{ij} the force acting between i and j then pressure can be written as follows:

$$P = \frac{1}{V} \left[Nk_B T - \frac{1}{3k_B T} \sum_{i=1}^N \sum_{j=i+1}^N \mathbf{r}_{ij} \mathbf{f}_{ij} \right] \quad 2.24$$

The forces are calculated as part of a molecular dynamics simulation, and so little additional effort is required to calculate the virial and thus the pressure. In the NPT ensemble, the total pressure of the system is constant while in NVT ensemble the pressure is fluctuating throughout the simulation.

2.3.6 Periodic Boundary Conditions

Periodic boundary conditions (PBC) are a set of boundary conditions that are often used to simulate a large system by modelling a small part that is far from its edge. A periodic boundary is an important technique in a molecular dynamics simulation. It is a clever trick to make a simulation that consists of only a few hundred atoms behave as if it was infinite in size. The main reason this is required is to remove the effects of the surface, which any finite sample of matter must have, and which ensure that the internal structure of the sample is dominated by surface rather than bulk forces (like surface tension – recall how a small drop of water tries to assume a spherical shape, in such cases the surface forces overwhelm the structure of the bulk liquid). Figure 2 illustrates the concept of periodic boundary conditions in two dimensions.

The shaded box represents the system we are simulating, while the surrounding boxes are exact copies in every detail – every particle in the simulation box has an exact duplicate in each of the surrounding cells. Even the velocities (indicated by the arrows) are the same. This arrangement is imagined to fill the whole of space. A result of this is that whenever an atom leaves the simulation cell, it is replaced by another with exactly the same velocity, entering from the opposite cell face. So the number of atoms in the cell is conserved. Furthermore, no atom feels any surface forces, as these are now completely removed. In the figure r_{cut} is the cut-off radius that is normally applied when calculating the force between two atoms.

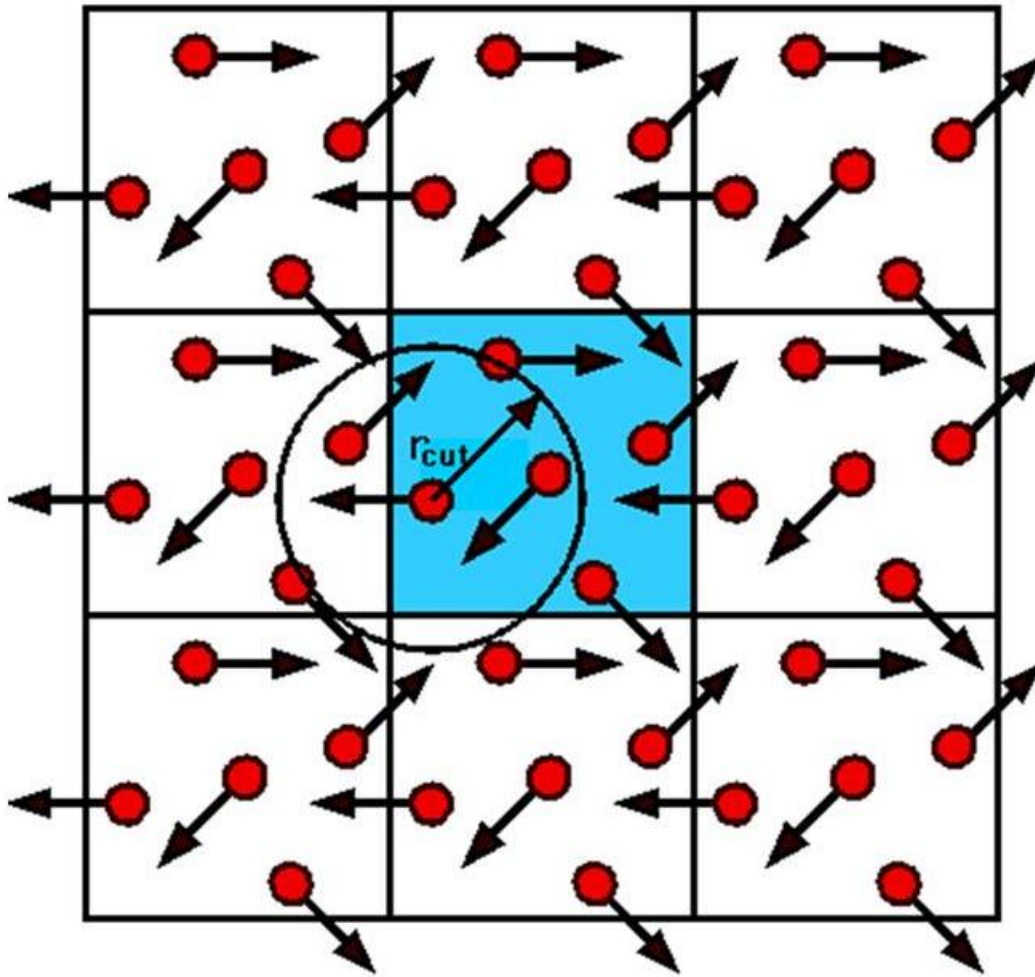


Figure 2: Illustration of the concept of periodic boundary conditions.

2.4 Simulation Properties

The molecular dynamics studies result in various quantities describing the temperature-dependent behaviour of the analysed systems. In our case, we looked at the radial distribution functions (RDFs) and diffusion coefficient. These quantities provide the structural information about the solid and liquid phases and about the melting phenomenon, meaning the temperatures of the solid-liquid transition can be estimated. However as stated by [70] the interpreted temperatures are not the real melting temperatures of the systems, but rather the temperatures of the mechanical instability of the infinite single crystal.

2.4.1 Radial Distribution Functions (RDFs)

The RDF is defined as the probability of finding an atom at a distance r from another atom compared to a homogeneous distribution [71] [72] and is given by

$$g(r) = \frac{V}{N_1 N_2} \frac{1}{4\pi r^2 \delta r} \left\langle \sum_i \sum_{j>i} \delta(r - r_{ij}) \right\rangle \quad 2.25$$

where V is the volume, N_1 and N_2 are the atom types of the RDF. The delta function must give rise to a value of one for a range of $r(\delta r)$. The RDF tends to one at long distances with sharp peaks indicating a regular lattice structure. For amorphous or liquid systems, the RDF shows characteristically a small number of broad peaks at short distance, indicating short-range order, superimposed on an oscillating trace to one, which indicates a loss of long-range order [73]. The structural properties of our system were investigated by analysing the partial radial distribution functions (RDFs), $g_{cos}(r)$, $g_{ss}(r)$. The partial RDFs $g_{\alpha\beta}(r)$ are defined in such a way that, by considering an atom of the species α , the probability of finding an atom of the species β in a spherical shell $(r, r + dr)$ is:

$$\rho_\beta 4\pi r^2 g_{\alpha\beta}(r) dr \quad 2.26$$

where $\rho_\beta = \frac{x_\beta}{V}$, is the number density of the species β with mole fraction x_β , and V is the volume per atom.

RDFs give the probability of finding the centre of a particle or atom at a given distance from the centre of another particle. We calculated the partial distribution functions obtaining the nearest neighbour interatomic distances of Ti -O.

The light atom at the center is the reference atom in figure 3, and the circles around it represent the other atoms. A ring centered on the reference is drawn with radius r and thickness dr . The radial distribution function can be an effective way of describing the structure of a system at different temperatures.

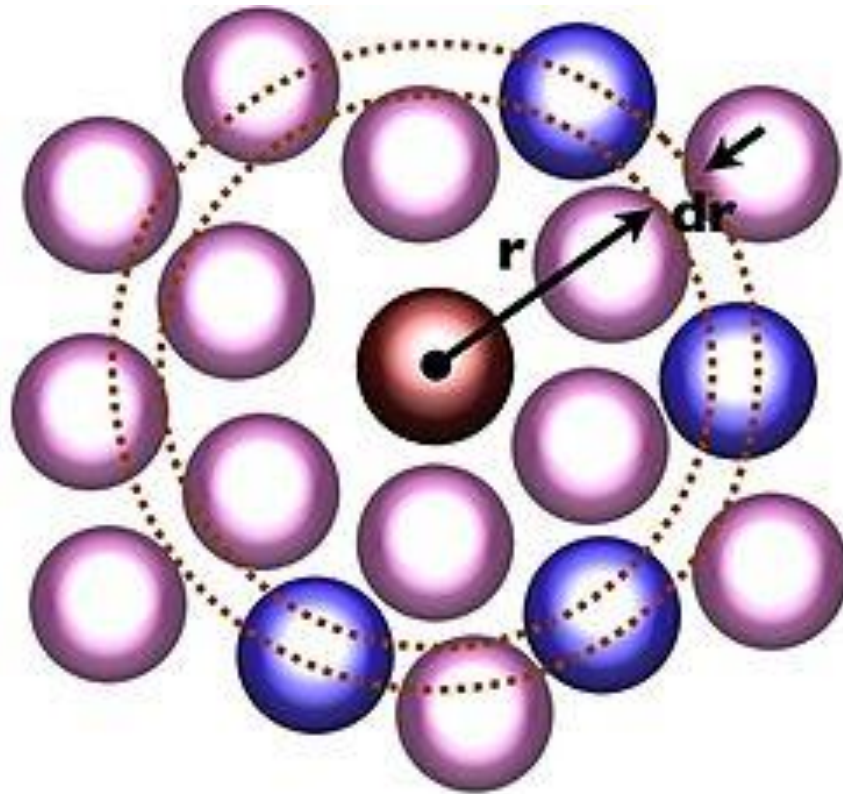


Figure 3: Schematic representation of the radial distribution function.

The light atom at the centre is the reference atom, and the circles around it represent the other atoms. A ring centred on the reference is drawn with radius r and thickness dr . The radial distribution function can be an effective way of describing the structure of a system at different temperatures.

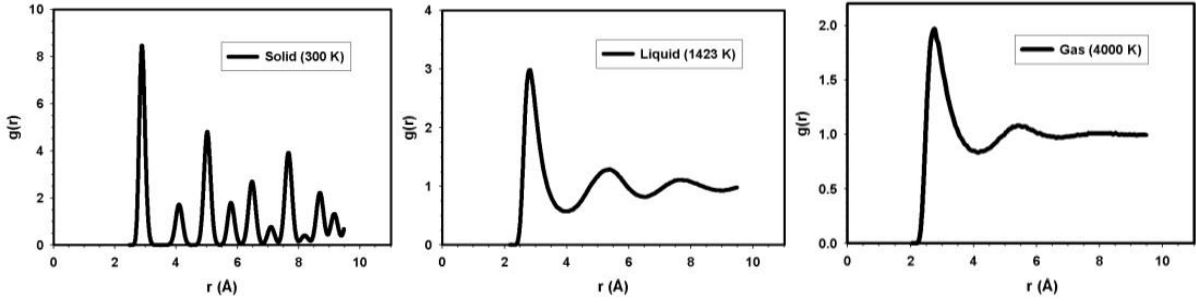


Figure 4: Represents RDFs for TiO₂ bulk from solid, liquid and Gas phases.

The RDFs for TiO₂ bulk, starting from a solid crystal on the left, the system reaches melting in the central figure and on the right, the gaseous system are shown in figure 4. The number of peaks decreases and the broadening of the peaks is quite noticeable. Differentiation between a solid and a liquid are detected using the RDFs by the number of peaks appearing in a particular RDF plot. In a crystal or solid, the radial distribution functions have a multiple number of sharp peaks and heights are characteristic of the lattice structure. The radial distribution function of a liquid has a small number of peaks at short distances and the height of the peaks decreases. For the crystalline solid, the peaks are sharp and thin and show long-range order. In case of a liquid phase, the peaks are broad and the radial distribution function rapidly converges to one as observed in the gaseous phase.

2.4.2 Diffusion Coefficient

The diffusion is another measure to estimate relative mobilities of individual LiTiO₂ atoms. It is known that diffusion coefficient can be estimated from the slope of MSD plots using the Einstein relation as follows:

$$D = \frac{1}{6} \frac{d}{dt} \langle |r_i(t) - r_i(0)|^2 \rangle \quad 2.28$$

The integral Equation 2.28 is the velocity autocorrelation function (VAF), which is related to the diffusion coefficient. The VAF decays to zero at long time; the function is integrated mathematically to calculate the diffusion coefficient as in Equation 2.29.

$$D = \frac{1}{3} \int_0^{\infty} \langle v_i(t) \cdot v_i(0) \rangle dt \quad 2.29$$

The melting point of the simulated system can be located by increasing the temperature of a crystalline system until diffusion appears. Diffusion is also the phenomena of random motion causing a system to decay towards uniform conditions. For example, diffusion of particles causes a net movement of particles from areas of high concentration to areas of lower concentration until equilibrium is reached. Diffusion is a spontaneous process more familiarly known as a passive form of transport, rather than active and affects a variety of different quantities. Spontaneous processes are not reversible.

Examples of diffusion include diffusion of concentration, heat, or momentum. Diffusion increases entropy, decreasing Gibbs free energy, and therefore is thermodynamically favourable. In all cases of diffusion, the flux of the transported quantity (atoms, energy, or electrons) is equal to a physical property (diffusivity, thermal conductivity, electrical conductivity) multiplied by a gradient (a concentration, thermal, electrical field gradient). Diffusion in this type of molecular dynamics simulations is calculated as the slope of the graph of mean square displacement as a function of time.

2.5 X- Ray Diffractions

X-ray diffraction is a powerful tool for materials characterization as well as for detailed structural elucidation. As the physical properties of solid (e.g., electrical, optical,

magnetic etc.) depend on atomic arrangements of materials, determination of the crystal structure is an indispensable part of the structural and chemical characterization of materials. X-ray patterns are used to establish the atomic arrangements of the materials because of the fact that the lattice parameter, d (spacing between different planes) is of the order of x-ray wavelength. Further, X-ray diffraction method can be used to distinguish crystalline materials from nano-crystalline (amorphous) materials. From X-ray diffraction pattern, we can obtain the following information:

- (i) to judge formation of a particular material system.
- (ii) Unit cell structure, lattice parameters, miller indices.
- (iii) Types of phases present in the material
- (iv) Estimation of crystalline/amorphous content in the sample.
- (v) Evaluation of the average crystalline size from the width of the peak in a particular phase pattern. Large crystal size gives rise to sharp peaks, while the peak width increases with decreasing crystal size.
- (vi) An analysis of structural distortion arising because of variation in d spacing caused by the strain, thermal distortion.

2.5.1 Determination of Crystal Size:

The X-ray diffraction analysis has been the most popular method for the estimation of crystallite size in nanomaterials and therefore, has been extensively used in the present work. The evaluation of crystallite sizes in the nanometer range warrants careful analytical skills. The broadening of the Bragg peaks is ascribed to the development of the crystallite refinement and internal strain. To size broadening and strain broadening, the full width at half maximum (FWHM) of the Bragg peaks as a function of the diffraction angle is analysed. The X-ray diffraction (XRD) peak

broadening calculates crystallite size of the deposits. The diffraction patterns are obtained using Cu K α radiation at a scan rate of 10/min. The full width half maxima (FWHM) of the diffraction peaks were estimated by pseudo-Voigt curve fitting. After subtracting the instrumental line broadening, which was estimated using quartz and silicon standards, the grain size can be estimated the Scherer equation

$$\frac{0.9\lambda}{\beta\cos\theta} = D$$

Where λ is wavelength of X-ray, β is FWHM in radian, θ is peak angle.

As for single crystal diffraction, an essential ingredient for the simulation of a powder diffraction experiment is the calculation of the structure factors F_{hkl} , which are related to the atomic positions and atomic scattering factors via equation below

$$F_{hkl} = \sum_1^N f_n e^{2\pi i(hu_n + kv_n + lw_n)} \quad 2.31$$

The powder diffraction intensity observed at diffraction angle 2θ is then given as:

$$I(\theta) = \sum_{hkl} P_{hkl}(2\theta - 2\theta_{hkl}) I_{hkl} \quad 2.32$$

Where the Integrated Bragg Intensity I_{hkl} is related to the structure factors F_{hkl} via:

$$I_{hkl} = M_{hkl} P_{hkl} L_{hkl} |F_{hkl}|^2 \quad 2.33$$

Here

M_{hkl} is the multiplicity of reflection hkl

P_{hkl} is the preferred orientation correction for reflection hkl

L_{hkl} is the Lorentz and polarization correction for reflection hkl .

$P_{hkl}(2\theta - 2\theta_{hkl})$ is an appropriate profile function.

The profile function may include an asymmetry correction, and its width depends on instrument resolution and sample broadening effects.

2.5.2 Multiplicity and Systematic Absences

2.5.2.1 Multiplicity

In the single crystal rotation geometry, two distinct reflections, hkl and $-h-k-l$ are each recorded twice in the rotation exposure. Were the crystal, say, to be cubic, with rotation about $[001]$, the planes 100 , -100 , 010 , and $0-10$ would all pass through the diffraction condition and be recorded at the same Bragg angle, 2θ . The random collection of orientations in powders implies that all the equivalent reflections contribute to a given diffraction cone, so that the intensity recorded at the appropriate Bragg angle simultaneously contains contributions from the 100 , -100 , 010 , $0-10$, 001 , and $00-1$ planes. The system symmetry in this case dictates that the intensity contributed by each of these planes is equal, but since there are six of them, the measured intensity must be divided by a multiplicity factor of six in order to obtain a relative measure of the 100 intensity. This multiplicity factor depends on the symmetry of the structure and on the nature of the indices, h , k , and l . For a general index plane, hkl , the multiplicity varies from 2 in the lowest triclinic symmetry to 48 in the highest symmetry cubic case. Friedel's law states that the intensity of radiation scattered from a given plane hkl is equal to that from its inverse, $-h-k-l$. Although this law breaks down when anomalous scattering effects are significant, it is assumed to apply uniformly here.

2.5.2.2 Systematic absences

Bragg reflections occur when the radiation scattered by each of the atoms, in the unit cell, do so in phase, i.e., constructive interference. For a primitive cell, the intensities of the reflections are easily predicted. In the case, however, of non-primitive cells there

are special conditions, which result in reflections of zero intensity. These are called systematic or space group absences. In the case of an I-lattice with lattice points at (0, 0, 0) and (1/2, 1/2, 1/2), it is observed that for reflections where the sum of the indices (h + k + l) is odd, no reflection is detected. This can be explained by the diffraction process from the (100) plane, where the combined scattering from the (0, 0, 0) lattice points do so completely in phase at the specific Bragg angle, but those at the (1/2, 1/2, 1/2) actually interfere. As there are equal occurrences of the two lattice points, they will cancel out. For centred systems the following equation can be used to predict the presence/absence of Bragg peaks; reflections will only be observed when n is an integer.

$$hx_n + ky_n + lz_n = n \quad 2.35$$

Where: h , k and l refer to reflection (hkl)

X_n , Y_n and Z_n refer to the n th lattice point's location in the lattice.

In addition to centred cells, systematic absences will occur in non-primitive systems when glide planes and/or screw axes are present. The method employed to determine whether a reflection is absent in these circumstances requires knowledge of the rotational and translational operators which define the crystal symmetry. If a reflection, $H = (hkl)$, is unchanged by applying a rotation operator, R , and if the scalar product with the corresponding translation operator, T , is not an integer, then the reflection is absent.

$$H.T = ht_x + kr_y + lt_z = H \quad 2.36$$

$$H.T = ht_x + kt_y + lt_y \neq n \quad 2.37$$

If both of these conditions are satisfied, then the reflection is computed to have zero intensity.

2.5.3 Correction Factors in Powder Diffraction

The powder diffraction trace represents a 1D projection of the 3D scattering intensities of each of the atoms in the unit cell. Translating the calculated reflection intensities into a continuous spectrum that accurately predicts the experimental trace requires knowledge of the conditions that existed during data collection. Using this knowledge, a number of corrections are applied to the intensity list to produce a realistic trace. These corrections are as follows: Lorentz and polarization correction, instrumental broadening, sample broadening, asymmetry corrections, preferred orientation and line shift correction.

2.6 Amorphisation and Recrystallisation Technique

Amorphisation and recrystallisation technique [75] is the strategy that has been used in atomistic simulation complex structures evolve during a pseudo-recrystallisation from an amorphous starting point. Amorphisation and recrystallisation is an evolutionary simulation technique where compression or tension is applied to the system to displace atoms from equilibrium positions. When pressure is released, atoms are accelerated to equilibrium positions having high ionic mobility as molten systems. To generate realistic models of supported oxide thin films one must consider various factors including the epitaxial relationships, defects and reduced interfacial ion densities. The defects, which evolve in response to misfit accommodation, may include dislocations arrays, vacancies, substitutions and interstitials including clustering of such defects. These structural features must be achieved in order to generate a realistic model even though some are challenging. To overcome the problems

associated with the starting structure, the supported thin film is forced to undergo an amorphous transition before recrystallising into a final structure. Such a procedure eliminates any possibility of the final structure reflecting artificially the starting structure. Essentially the system loses all memory of the preparatory configuration and dynamical simulation, as applied to an amorphous structure, allows a more comprehensive exploration of the configurationally space, which is likely to results in an energetically more favourable, and hence more realistic, final interface structure. This method allows interfacial structures to evolve during the course of the simulation influenced solely by substrate material and associated lattice misfit.

Various mechanisms for inducing amorphisation have been explored for supported metal-oxide thin films associated with both positive and negative lattice misfits. These include performing dynamical simulation at very high temperatures to melt the thin film and constraining the thin film under conditions of compression or tension: under dynamical simulation, the considerable strain within the thin film results in an amorphous structure. The latter can be achieved either by modifying artificially the potential parameters during the amorphisation step or by constructing an interface system with a particular associated lattice misfit (positive or negative) based upon, for example, some particular near coincidence site lattice[76][77].

The amorphisation is induced by straining the support thin film under high compression. The application of high-temperature dynamical simulation to this strained system results in the amorphisation of the thin film over layer. Prolonged dynamical simulation is required to allow the system to recrystallises under the influence of the support. This methodology is purely a simulation technique to derive low energy structures and the structural evolution of the system bears no physical significance. The main driving force to the amorphisation is the strain under which the

thin film is constrained, while the temperature at which the dynamical simulation is run is secondary to inducing amorphisation. For example, the procedure can be performed equally as well at 20 K as at 200 K. However, the recrystallisation process at 20 K is much slower. In essence, the optimum temperature is one that allows the structure to evolve but that falls of melting the thin film. This would be detrimental as it would prevent recrystallisation and require an additional quenching step [78] .

An important feature of the methodology is that the amorphous transition enables all memory of the preparatory configuration to be lost (radial distribution functions for the amorphous thin film are broad indicating no long range ordering) and therefore the final structures cannot reflect artificially the starting structure [78]. The recrystallisation is deemed complete when the system is no longer evolving structurally or energetically, the duration of which is system dependent. In addition, dynamical simulation, as applied to an amorphous structure, allows a more comprehensive exploration of the configurational space, which is likely to result in an energetically more favourable, and hence more realistic, final interface structure [79].

This technique has been implemented on various materials such as thin films and nanoparticles [80], generate models for CeO₂ nanocrystallites [81], microstructure in MnO₂ [82], shape of CeO₂ nanoparticles [83], MgO cluster supported on BaO (100) [75] and lithium insertion into [84]. In this work, we will employ this technique on the nanostructures and lithiated nanostructures of TiO₂. In order to lithiate the various nano-architectures, lithium ions will be inserted at random positions in the amorphous TiO₂; and coordinates will be chosen to ensure that Li ions are not positioned on top of other atoms in the simulation cell. To facilitate charge neutrality, an equivalent number of Ti⁴⁺ species were reduced to Ti³⁺. The method was previously used

successfully in the bulk MnO_2 [84]. We will also present the radial distribution functions of the systems to verify the process of amorphisation and recrystallisation.

2.7 Lithiation of Nanostructures

This section discuss on how the Li ions were introduced into the TiO_2 nanostructures. Dr M.G. Matshaba [85] also applied the lithiation program used in this study. The lithium ions were randomly inserted into the nanoporous TiO_2 using the following procedure: Firstly, a random coordinate was generated, by taking the minimum and maximum values of the cell dimension of the nanostructure, and then a value between the minimum and maximum was randomly generated. This was done for all cell dimensions x, y and z. Thereafter the program constructed a cube of about 2.5 Å around the newly generated coordinate and checked to see if there was another atom closer to it than 1.6 Å. If there was then the coordinate was rejected, otherwise it was accepted and that is where the lithium ion was inserted. The Ti^{4+} closest to the inserted lithium was then reduced to the Ti^{3+} for charge compensation.

2.7.1 Lithiation at Octahedral Sites

The pristine TiO_2 nanostructures are large and comprise 15972 atoms, 5324 titanium atoms and 10648 oxygen atoms. Additionally, they are heavily twinned and non-crystalline making it difficult to easily compute the coordinates of the 1x1 tunnel sites by using the knowledge of symmetry and lattice constants. However, each tunnel is enclosed by four walls of linked edge-sharing TiO_6 octahedral chains with slightly varying distance between the chains. The program uses these twinning octahedral chains to estimate the tunnel sites where lithium ions will be intercalated.

Slicing the TiO_6 octahedral chain planes and rendering min polyhedral view reveals different the 1x1 tunnel configurations (figure 6). During intercalation, lithium ions are

placed at specific locations in the tunnels which we denote lithium insertion sites. The estimation of the coordinates of these lithium insertion sites is calculated with the midpoint formula for different tunnel configurations shown in a figure below.

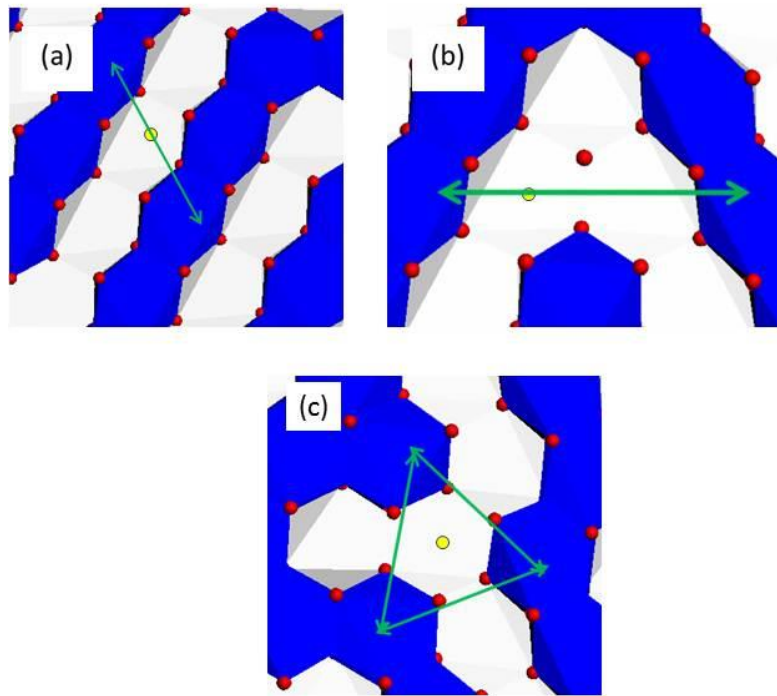


Figure 5: slices through the nanostructure showing different tunnel configurations. The yellow circle indicates lithium insertion site.

The coordinates of the lithium insertion site (x, y, z) for a tunnel structure in figure 5 (a) is estimated by using the two or three titanium atoms on the same TiO_6 octahedral planes, depicted by the ends of the arrow in the midpoint formula:

$$(x, y, z) = \left(\frac{x_1+x_2}{2}, \frac{y_1+y_2}{2}, \frac{z_1+z_2}{2} \right) \quad 2.34$$

In figure 5 (b) the estimation of the insertion sites is achieved by applying the midpoint formula twice. Applying the midpoint formula once result in a coordinate in the middle of the two tunnel sites. Using the newly computed coordinate with the coordinate of

one of the manganese atoms at the ends of the arrow in the formula gives the coordinate of the tunnel site (yellow circle):

$$(x, y, z) = \left(\frac{x_1}{2} + \frac{x_1+x_2}{4}, \frac{y_1}{2} + \frac{y_1+y_2}{4}, \frac{z_1}{2} + \frac{z_1+z_2}{4} \right) \quad 2.35$$

In the last case i.e. in figure 6 (c) the computation of the tunnel sites is accomplished by using the coordinates of three manganese atoms in the triangle midpoint formula:

$$(x, y, z) = \left(\frac{x_1+x_2+x_3}{3}, \frac{y_1+y_2+y_3}{3}, \frac{z_1+z_2+z_3}{3} \right) \quad 2.36$$

The decision of whether two manganese atoms can be used to compute an insertion site depends on the separation distance between them. The Ti-Ti radial distribution function of the nanostructure provides us with a good estimate of these separation distances.

The program computes the lithium insertion sites by checking the separation distance between each pair of titanium atoms in the range specified by the third, fifth and ninth peaks in the radial distribution function of a rutile-type structure and using the appropriate form of the midpoint formula. The insertion site is then validated by checking its distance from all atoms within a small cube constructed around the insertion site with dimensions that are slightly larger than the minimum Ti-O (Ti – titanium in rutile-type structure) separation distance. If there is an atom (Ti, O, or Li⁺) which is closer to the insertion site by more than 1.6 Å (for pyrolusite) then the insertion site is not valid and it is discarded. All valid insertion sites are then saved in a file that will be used during lithium insertion into the various nanostructures.

2.7.2 Lithium Insertion

The program uploads the lithium insertion sites from the file produced in the previous step, randomly selects a tunnel site and inserts a lithium ion at its coordinates. Charge

compensation in the structure is achieved by changing the titanium (4^+ -oxidation state) closest to the lithium cation into the Jahn-Teller active titanium (3^+ -oxidation state). This process is repeated for all the lithium ions inserted in the structure. Note that the program randomly selects an insertion site and the corresponding closest trivalent titanium cation and this can result in different lithium-titanium configurations with different energies. The lithiated structure is not of the lowest energy. To obtain the lowest energy structure one could lithiate in a Monte Carlo way and then run molecular dynamics simulations on each configuration that would be very time consuming considering the massive size of the nanostructures.

Chapter 3

3 Results

In this chapter we present results obtained on all four various nano-architectures of TiO_2 namely (a) nanosphere, (b) nanosheet, (c) nanoporous and (d) bulk. Lithiation behaviour of nano-architectures was studied by varying lithium concentration into nano-architectures of Li_xTiO_2 shown in figure 6 with $x= 0.03, 0.04$ and 0.07 .

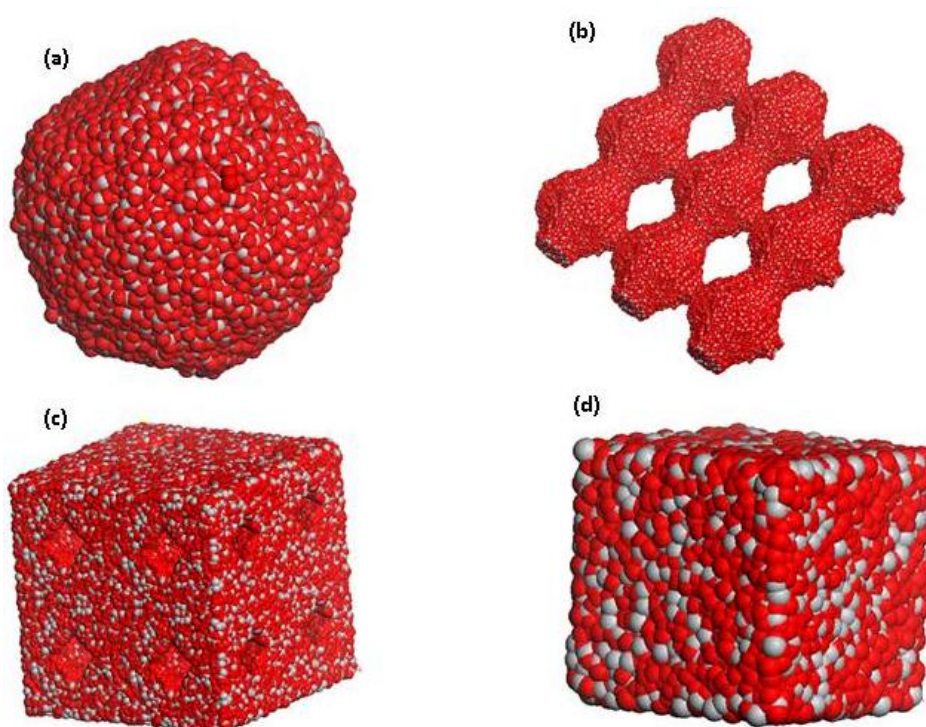


Figure 6: Nanostructures of TiO_2 (a) nanosphere, (b) nanosheet, (c) nanoporous and (d) bulk [77].

Initially, lithium ions were randomly distributed throughout the amorphous structure before the molecular dynamics simulations are performed. Amorphisation and recrystallisation technique was employed to generate crystallised lithiated nanostructures.

Radial distribution functions for Ti^{3+} - O^{2-} and Ti^{4+} - O^{2-} on the same axis and configuration energy vs time graph were plotted to confirm recrystallisation. The recrystallized structure was then cooled by running molecular dynamics (MD) simulation for 500 ps at 1500 K, followed by 250 ps at 1000 K, 250 ps at 500 K, and lastly 500 ps at 0 K, then confirmed by radial distribution functions for Ti^{3+} - O^{2-} and Ti^{4+} - O^{2-} from 1500 to 0 K. Note the Ti^{3+} were not held stationary in our molecular dynamics simulations and are dynamically allowed to evolve.

To evaluate Li transport within the recrystallised and cooled nanostructures, molecular dynamics simulations were then performed at high temperatures ranging between 100 and 500 K with 100 intervals within an NVT ensemble. X-ray diffraction patterns at low and high lithium concentration were calculated. Diffusion coefficient as a function of temperature for Li, Ti^{3+} , Ti^{4+} and O atoms graphs was evaluated to validate transportation of atoms within the nanostructures of all three lithium concentrations.

Comparison of microstructures at 0 and 500 K for all three lithium concentrations are also presented. It is noted that XRDs using Cu source are in good accord with experimental results as compared to those of Fe. Hence, we will calculate XRDs of cooled structures and temperature variance with the copper only source and compare our results with available experimental results.

3.1 Methodology

The potential models employed in this chapter are based on the Born model of ionic solids. However, Ti^{4+} , Ti^{3+} , Li^+ and O^{2-} ions interact via long-range Coulomb and short-range interactions, given in table 2. In this chapter, we present and discuss the lithiated nanostructures of TiO_2 . All produced nanostructures were inserted with different number of lithium atoms.

Table 2: Buckingham potentials used for lithiated TiO₂

Ion pair (ij)	A _{ij} (eV)	ρ_{ij} (Å)	C _{ij} (eV.Å ⁶)
Ti ³⁺ -O ²⁻	18645.840	0.1950	22.0000
Li ⁺ -O ²⁻	426.48000	0.3000	0.00000
Ti ³⁺ -Ti ⁴⁺	28707.210	0.1560	16.0000
Ti ³⁺ -Ti ³⁺	33883.920	0.1560	16.0000

3.1.1 Amorphisation and Recrystallisation of Li_xTiO₂ Nanostructures.

This section presents and discusses the various lithiated nanostructures of TiO₂, generated by the amorphisation and recrystallisation strategy. Cooling and variation of temperature process was employed on all lithiated structures to maintain structural stability. Configurational energy as a function of time to confirm the crystal growth of the nanostructures after recrystallisation are shown.

Radial distribution functions (RDFs) of all the cooled structure are shown to present the structure of the nanostructures right exactly from 1500 K up until to 0 K XRDs of the four nano-architectures are calculated, for each nano-architecture observation of this XRDs were made for cooled and high temperature structures with 0.03 and 0.07 lithium concentrations.

Microstructures are also presented in order to compare available defects present at cooled and high temperatures. Diffusion coefficients of atoms as a function of temperature are also presented to show how they vary at different Li concentrations.

3.1.2 Crystal Growth on the Li_xTiO_2 Nanostructures.

The structures of lithiated TiO_2 nanosphere with 0.03, 0.04 and 0.07 lithium ion concentrations before recrystallisation are given in figure 7. The lithium atoms are located right inside and outside the nanosphere systems. Segregations is observed on all concentrations and there more lithium insertion the more formation of segregation.

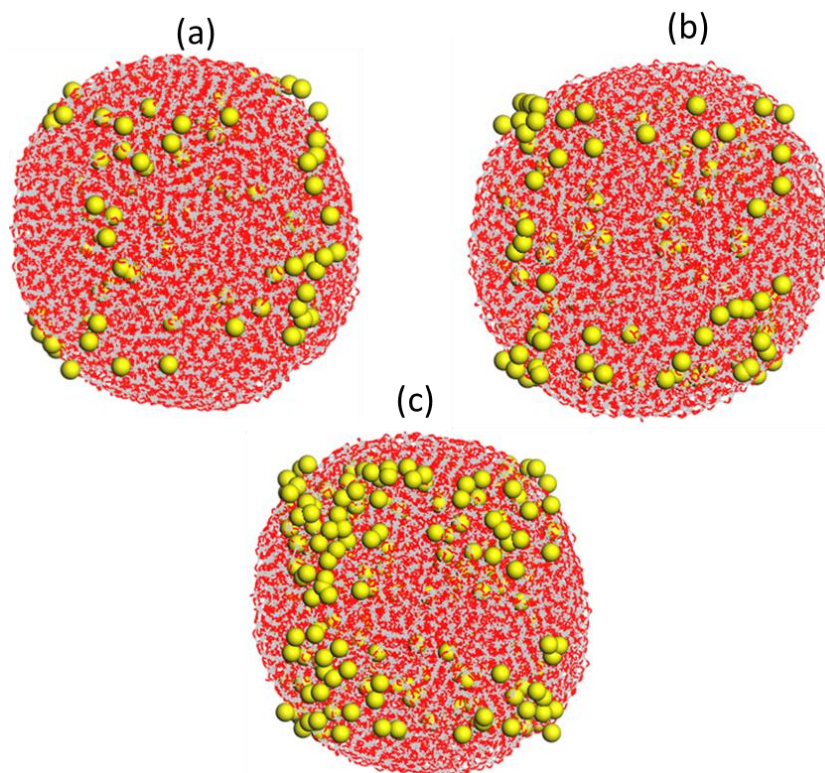


Figure 7: Amorphous nanosphere structures of TiO_2 with (a) 0.03, (b) 0.04 and (c) 0.07 lithium ion concentration at 2000 K.

Recrystallised structures of lithiated nanosphere are given in figure 8. After recrystallisation, some lithium atoms move out of the nanosphere or away, so these structures are recrystallised since some patterns are observed on the structure. As to how many lithium atoms move out of the system and how many remain, depends on the number of lithium atoms that are in the system.

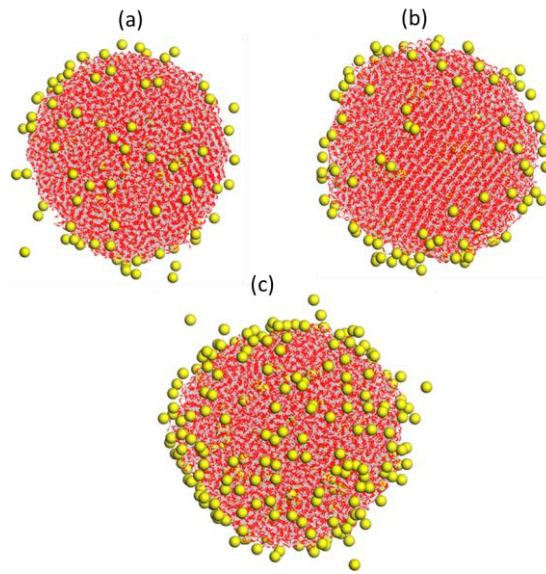


Figure 8: Recrystallised nanosphere structures of TiO_2 with (a) 0.03, (b) 0.04 and (c) 0.07 lithium ion concentration at 2000 K.

The TiO_2 nanosheet was lithiated with three different concentrations of 0.03, 0.04 and 0.07 Li ion concentrations. Figure 9 presents the amorphous lithiated TiO_2 nanosheet. Lithium atoms are clustering right inside the system for all concentrations.

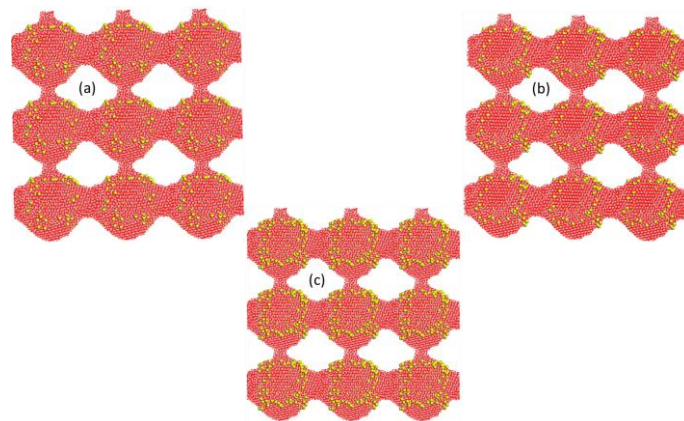


Figure 9: Amorphous nanosheet structures of TiO_2 with (a) 0.03, (b) 0.04 and (c) 0.07 lithium ion concentrations at 2000 K.

Recrystallisation was performed on all lithiated structures presented from figure 10, here we observe dispersing of lithium atoms in such a way that few lithiums are moving out of the systems and most remained in the system.

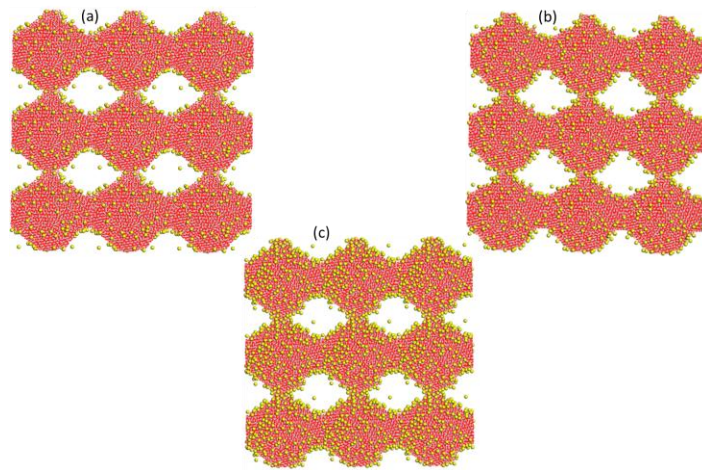


Figure 10: Recrystallised nanosheet structures of TiO_2 with (a) 0.03, (b) 0.04 and (c) 0.07 lithium ion concentrations at 2000 K.

Figure 11 shows an amorphised porous nanostructure with 0.03, 0.04 and 0.07 lithium concentrations respectively. Observing from the structure lower concentration give less clustering of lithium atoms and higher concentrations more clustering of lithium atoms. Lithium distribution tends to move away from the pores then moves right within the structures. The Ti and O atoms are disorderly arranged making the lithium atoms to move freely.

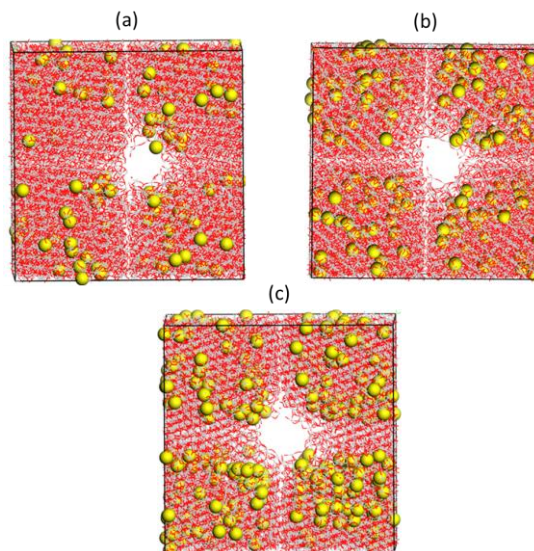


Figure 11: Amorphous nanoporous structures of TiO_2 with (a) 0.03, (b) 0.04 and (c) 0.07 lithium ion concentrations at 2000 K.

The nanoporous structures were crystallised using the NVT ensemble, with different lithium concentrations, and are given in figure 12. This structure of the nanoporous TiO_2 at all lithium concentrations shows clearer patterns, some vacancies and grain boundaries. These clear crystalline patterns confirm recrystallisation and this process push most lithium atoms to locate themselves right on the edges of the pores.

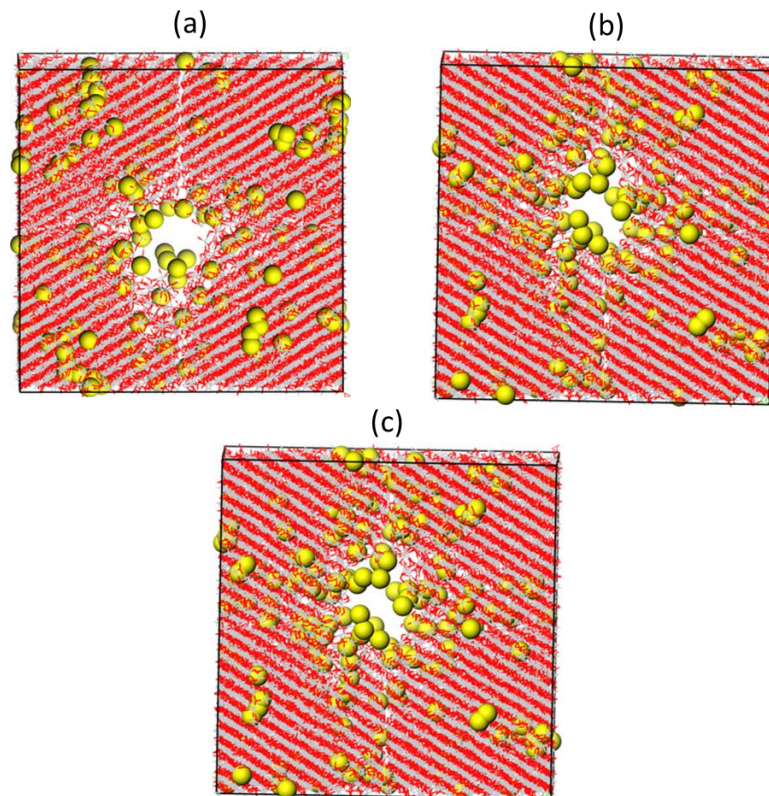


Figure 12: Recrystallised nanoporous structures of TiO_2 with (a) 0.03, (b) 0.04 and (c) 0.07 lithium ion concentrations at 2000 K.

The amorphous bulk structures of TiO_2 were lithiated to 0.03, 0.04 and 0.07 concentrations, and related lithium ions are well distributed as seen in figure 13. No clustering or segregation of these lithium atoms are observed also no patterns on the structure meaning that all systems are amorphous. Patterns started showing after recrystallisation as shown in figure 14, however these patterns are not complete on all systems.

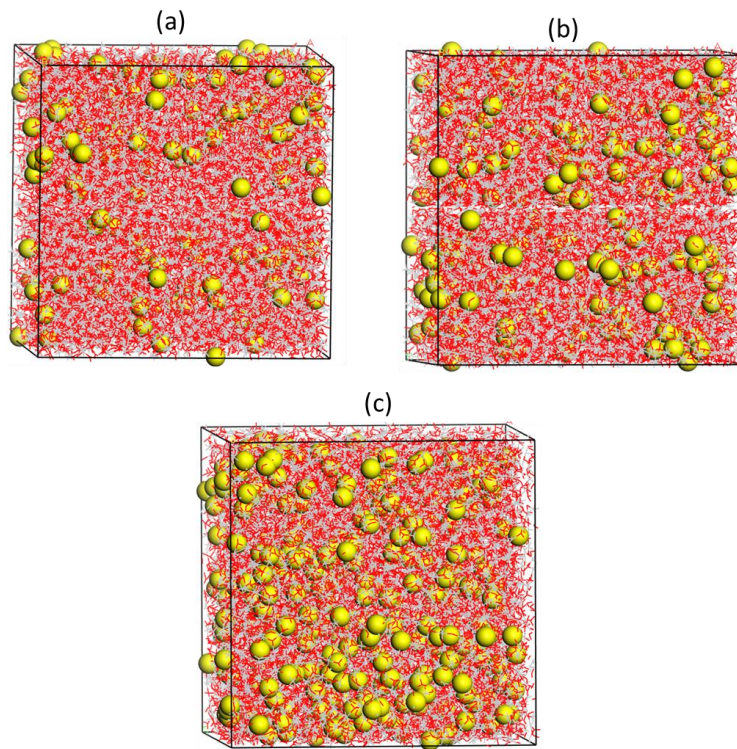


Figure 13: Amorphous bulk structures of TiO_2 with (a) 0.03, (b) 0.04 and (c) 0.07 lithium ion concentrations at 2000 K.

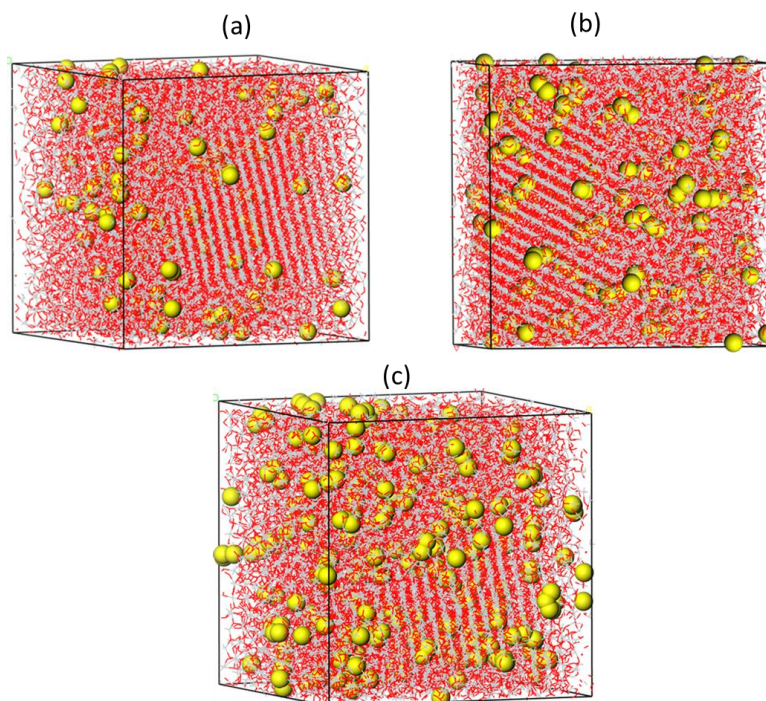


Figure 14: Recrystallised bulk structures of TiO_2 with (a) 0.03, (b) 0.04 and (c) 0.07 lithium ion concentration at 2000 K.

3.1.2.1 Configurational Energy Plots

A plot of the configuration energy as a function of time for all lithiated nanospheres during recrystallisation is given in figure 15. The energy plot of the nanosphere with 0.03 lithium ion concentration shows recrystallisation from 0 to 0.25 ns with configuration energy changing from -2.0128×10^5 to -2.0266×10^5 eV. In the period 0.25 to 0.7 ns, there is a small change of energy, which indicates that the growing of crystals is nearing an end. In the range 0.7 to 2.1 ns, the energy remains constant, which suggests that the lithiated nanosphere has reached full recrystallisation form.

The configuration energy plot of the nanosphere with 0.04 lithium ion concentration exhibits an end of reduction from 0 to 0.4 ns, which could be associated with a crystallisation phase. An energy reduction, but more abrupt than that of the 0.03 Li ion concentration system, is noted from 0.4 to 0.5 ns with configuration energy varying from -2.02×10^5 to -2.03×10^5 eV. From 0.5 to 0.6 ns the energy is near constant, which signals ends of crystallisation. From 0.6 to 2.1 ns the energy was constant throughout confirming a complete crystallisation.

The slope of the configuration energy plot, for the 0.07 Li ions nanosphere, shows smooth curve right from 0 to 0.5ns which seems to be where crystallisation occurred then followed by the growing of crystals right from 0.5 up to 0.8 ns with energies ranging from -2.00×10^5 to -2.01×10^5 eV. However, from 0.8 to 1.0 ns the energy tends to level off which reveal that the structure ceases to recrystallise.

From 1.0 ns onwards, the energy is almost invariable proving that the structure has reached its crystallinity. Hence, from all three plots we observe that there is an amorphous (A) to crystalline (C) transition caused by the notable drop of energy. However, as more lithium atoms are introduced in the nanosphere it takes much longer

time to fully recrystallise.

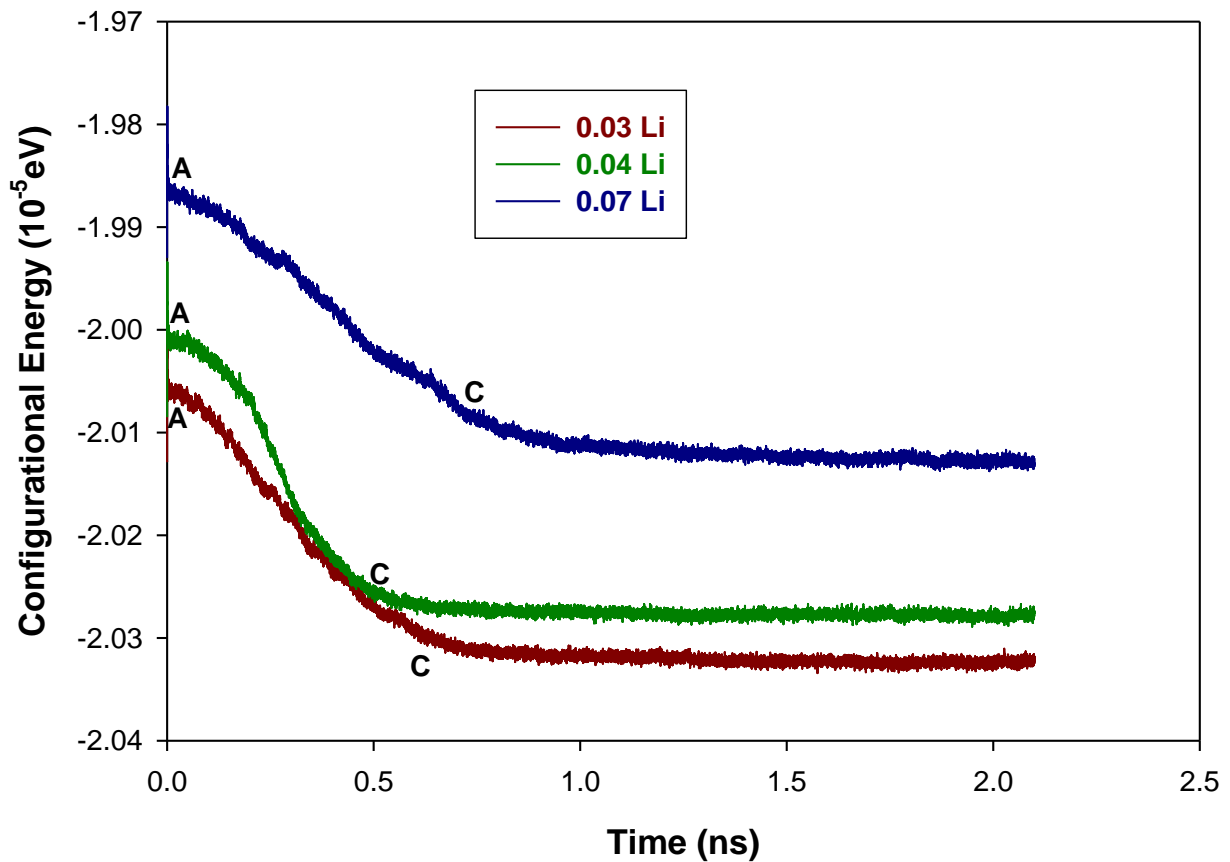


Figure 15: Calculated configuration energy as a function of time after recrystallisation for TiO₂ nanosphere structure with 0.03, 0.04 and 0.07 Li ion concentrations.

Figure 16 represents a graph of configuration energy as a function of time graph for all lithiated nanosheet structures. As observed from the amorphous lithiated structures that some patterns were already showing, a very small change in energy is expected. Graph of nanosheet with 0.07 lithium concentration has more change in energy followed by 0.04 lithium concentration which is very small, which implies that the systems was merely amorphous before recrystallisation due to higher concentrations of lithium atoms. Constant energy is observed at 0.03 lithium concentration from the

initial to the final time, which implies that this system is fully recrystallised and thus systems with 0.04 and 0.0 Li concentrations are also fully recrystallised.

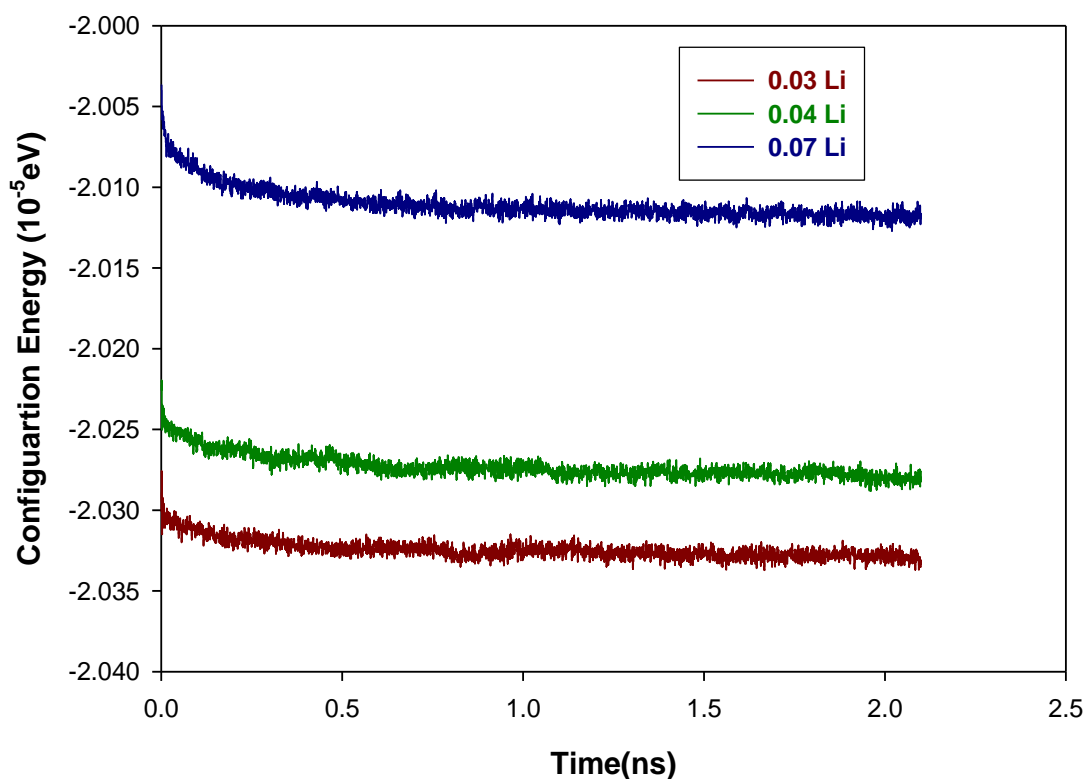


Figure 16: Calculated configuration energy as a function of time after recrystallisation for TiO₂ nanosheet structure with 0.03, 0.04 and 0.07 Li ion concentrations.

Configuration energy as a function of time graph for all lithiated nanoporous TiO₂ at all concentrations are presented in figure 17; a more negative energy corresponds to a more stable structure. They all show constant energy throughout the plot, but the graph of porous with 0.07 lithium ion concentration shows a higher energy than that of the 0.04 lithium ion and the 0.03 lithium ion concentration has lowest configuration energy hence most stable. Since all the plots show constant energy after this small amorphous-crystalline transition at all concentrations, it implies that the structures have reached their crystalline state.

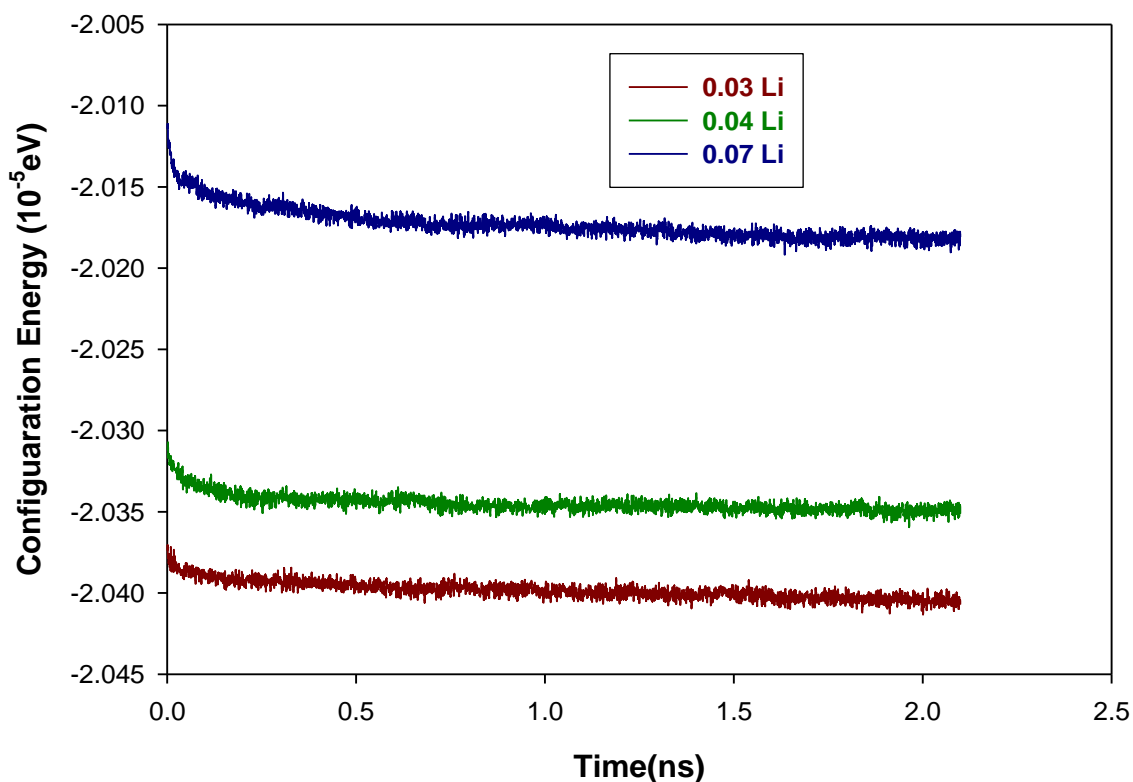


Figure 17: Calculated configuration energy as a function of time during recrystallisation for TiO₂ nanoporous structure with 0.03, 0.04 and 0.07 Li ion concentrations.

The graphs of configuration energy as a function of time for lithiated bulk TiO₂ structures are displayed in figure 18. The energy plot of the bulk with 0.03 lithium ion concentration shows a sudden decrease in energy from point A to B at time 0 and 0.5 ns. A continuous decrease in energy is observed above 0.5 ns, which further goes to 0.9 ns in the region (B-C). Above 0.9 ns a constant energy is detected which indicates a complete recrystallisation. The configuration energy vs time plot of the bulk with 0.04 lithium ion concentration indicates that the amorphous region (A-B) is near constant and related to nucleation. It subsequently exhibits an abrupt reduction from 0.3 to 0.6 ns, which is linked to the transition from an amorphous to crystalline phase. After 0.6 ns, the energy is invariable which shows that the system is recrystallised. The plot of the bulk with 0.07 lithium ion concentration depicts almost no change in energy from

0 to 0.3 ns and the region of (A-B) is more extended compared to that of 0.03 and 0.04 lithium concentrations. From 0.3 ns, we observe a sharp decrease of energy until 0.9 ns, which corresponds to an amorphous to crystalline transition. From 1.0 ns, the energy is constant until 2.1 ns, which suggests that the system is completely recrystallised.

The magnitude of the energy reduction for all three systems is equivalent to the latent heat of crystallisation. On comparison, the configuration energy shows that bulk structure with 0.03, 0.04 and 0.07 lithium ion concentrations require 0.4, 0.3, 0.5 ns respectively to undergo an amorphous to crystalline transition. The extended amorphous regions in figure 18, i.e. A to B and C to D, depicts the long time it takes for the structure to crystallise.

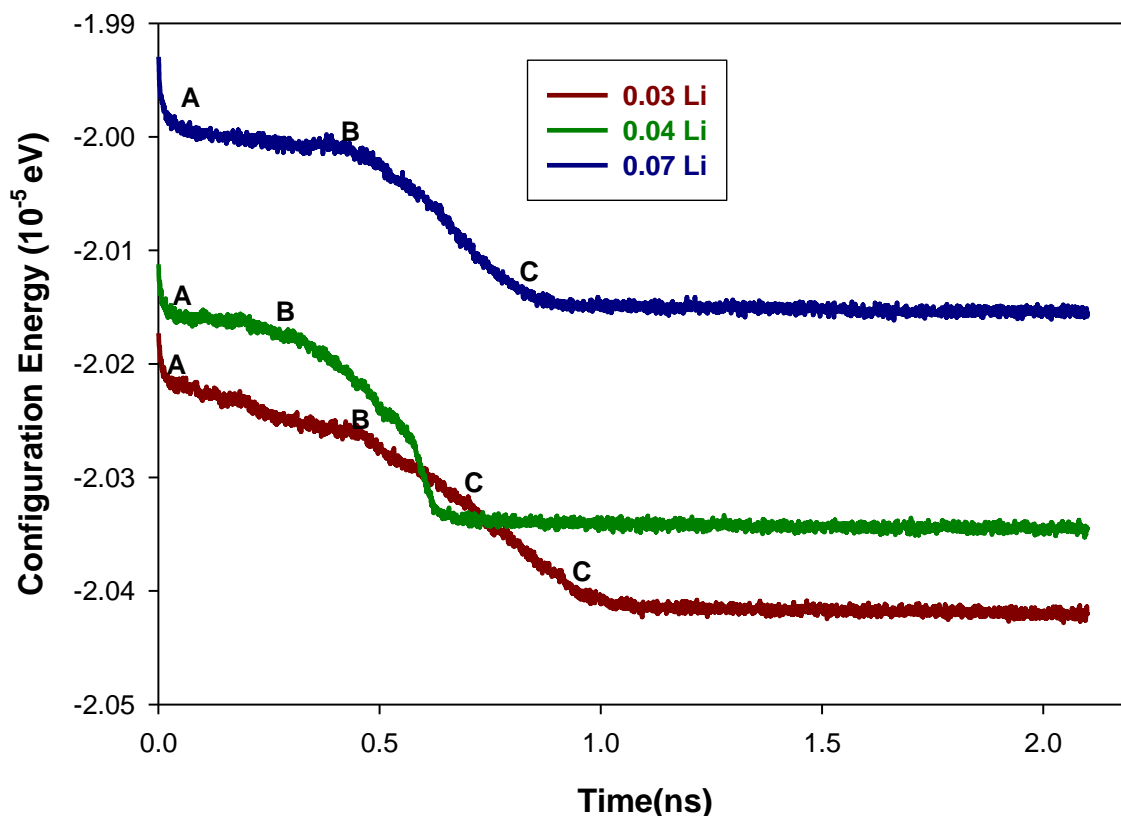


Figure 18: Calculated configuration energy as a function of time after recrystallisation for TiO₂ bulk structure with 0.03, 0.04 and 0.07 Li ion concentrations.

3.1.3 Cooled Nano-Architecture Structures of Li_xTiO₂

All four recrystallized nanostructures were cooled by running molecular dynamics (MD) simulations for 500 ps at 1500 K, followed by 250 ps at 1000 K, 250 ps at 500 K, and lastly 500 ps at 0 K. Cooled structures of nanosphere at 0 K with (a) 0.03, (b) 0.04 and (c) 0.07 lithium ion concentrations are shown in Figure 19. Very clear patterns on (a) and (b) are observed than on (c).

More lithium atoms are noted around the edges of the cooled nanosphere unlike what is observed on the high temperature recrystallised structure where lithium atoms moved away from the structure. Thus, the nanosphere did not undergo any significant structural changes on (a) and (b) whereas (c) has a complex arrangement of atoms

upon cooling but they all kept the atoms together and prevented them from moving away.

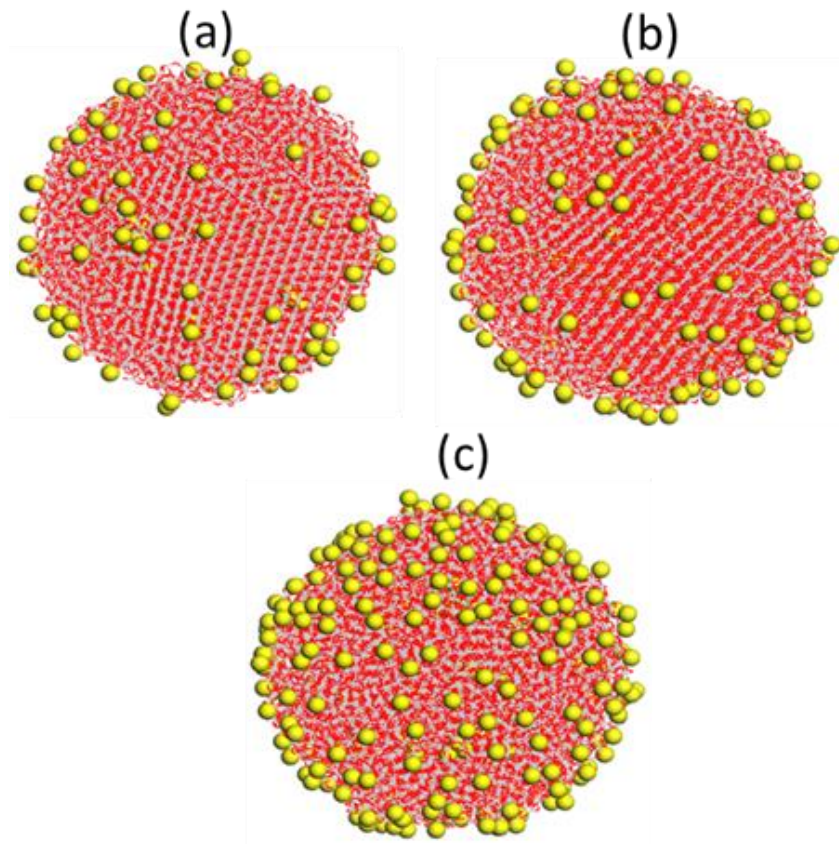


Figure 19: 0K cooled nanosphere structures of TiO_2 with (a) 0.03, (b) 0.04 and (c) 0.07 lithium ion concentrations.

The recrystallised nanosheets with (a) 0.03, (b) 0.04 and (c) 0.07 lithium ion concentrations were cooled and are shown in figure 20. More clear patterns are observed on the system and most lithium atoms are within the nanosheet as compared to recrystallised nanosheet at 2000 K in figure 10.

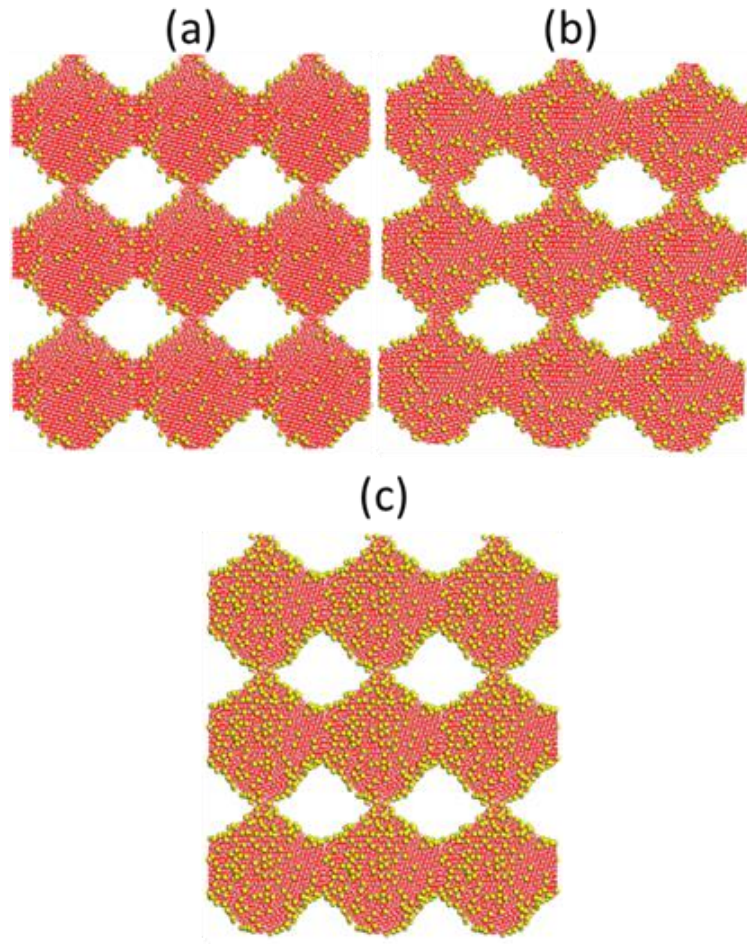


Figure 20: 0K cooled nanosheet structures of TiO₂ with (a) 0.03, (b) 0.04 and (c) 0.07 lithium ion concentrations.

We have cooled the recrystallised nanoporous structures with (a) 0.03, (b) 0.04 and (c) 0.07 lithium ion concentrations and they are shown in figure 21. The channels are open with lithium ions leaving the edges of channels as observed in all concentrations. Crystalline patterns are clearly more visible as compared to those of the recrystallised structures at 2000 K. As the number of lithium atoms is increased, we observe more atoms on the channels and within the system.

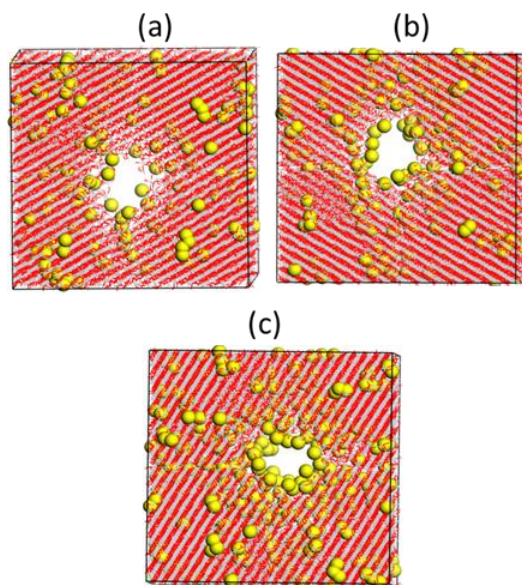


Figure 21: 0K cooled nanoporous structures of TiO_2 with (a) 0.03, (b) 0.04 and (c) 0.07 lithium ion concentrations.

The cooling procedure was also applied on recrystallised bulk TiO_2 with (a) 0.03, (b) 0.04 and (c) 0.07 Li ion concentrations and their corresponding structures are shown in figure 22. Fewer tunnels are observed on (a) and (b) but (c) show no crystalline patterns.

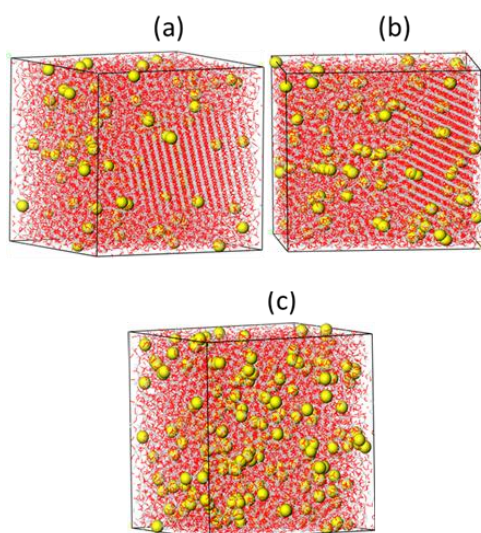


Figure 22: 0K cooled bulk structures of TiO_2 with (a) 0.03, (b) 0.04 and (c) 0.07 lithium ions.

3.1.3.1 Radial Distribution Functions of Li_xTiO_2 at cooled temperatures.

Total radial distribution functions (RDF) of a nanosphere for 0.03 Li ion concentration are presented in figure 23 with different maximum $g(r)$ values of 70 and 80 for (a) $\text{Ti}^{3+}-\text{O}^{2-}$ and (b) $\text{Ti}^{4+}-\text{O}^{2-}$ interactions respectively. It can be deduced from peaks near 2 Å that there is a higher probability of finding $\text{Ti}^{4+}-\text{O}^{2-}$ ion interactions, at that separation, than the $\text{Ti}^{3+}-\text{O}^{2-}$ ones.

The two interactions have different trends of peaks where (b) shows fairly smooth curves at different temperatures, but (a) has noisy sharp peaks corresponding to 0 K at 2, 3.9, 4.5 and 5.4 Å which tend to be broader from 5.5 Å up to the highest value. On the other hand (b) has sharp peaks at a few separations which then tend to be broad from this point up to 10 (Å). It could then be surmised that (a) suggests a more ordered system and (b) depicts a highly disordered system.

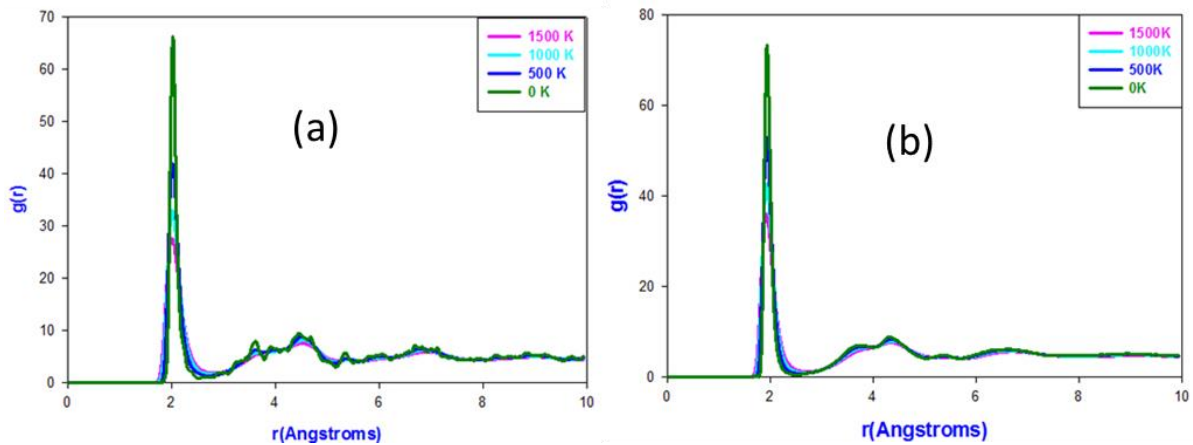


Figure 23: Total RDFs for (a) $\text{Ti}^{3+}-\text{O}^{2-}$ and (b) $\text{Ti}^{4+}-\text{O}^{2-}$ in the TiO_2 nanosphere with 0.03 lithium ion concentration at different temperatures.

Figure 24 shows radial distribution functions of $\text{Ti}^{3+}-\text{O}^{2-}$ and $\text{Ti}^{4+}-\text{O}^{2-}$ TiO_2 nanosphere with 0.04 lithium ion concentration at different temperatures. As in figure 23, a sharp peaks are observed around a radial distance of 2 Å followed by other low intensity

peaks at larger distances, and those corresponding to 0 K are more distinct. However, peaks for the $\text{Ti}^{4+}\text{-O}^{2-}$ are as well defined unlike those of 0.03 lithium ion concentration. All such data depicts slight crystallinity of nanosphere at the 0.04 concentration.

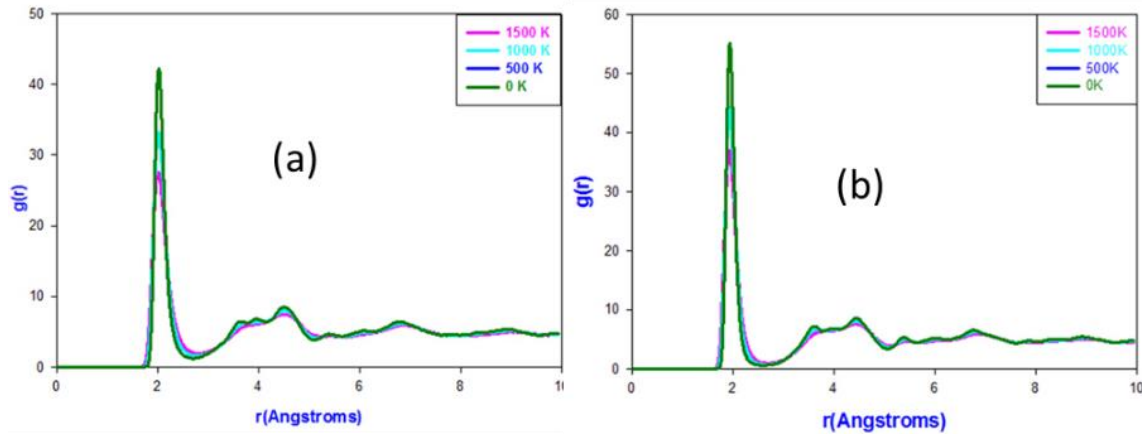


Figure 24: Total RDFs for (a) $\text{Ti}^{3+}\text{-O}^{2-}$ and (b) $\text{Ti}^{4+}\text{-O}^{2-}$ in the TiO_2 nanosphere with 0.04 lithium ion concentrations at different temperatures.

A further exploration on the evolution of atomic structure and temperature in the 0.07 lithium ion concentration nanosphere is depicted by radial distribution functions in figure 25. As in previous concentrations, a sharp large peak is noted around 2 Å and subsequent peaks are lower in magnitude. The peaks corresponding to 0 K for the $\text{Ti}^{3+}\text{-O}^{2-}$ interaction are well defined, although other higher temperature peaks are smoother and not as distinct as those of 0.03 and 0.04 Li concentrations. The $\text{Ti}^{4+}\text{-O}^{2-}$ interaction peaks of the 0.07 lithium ion concentration tend to be generally smooth for all investigated temperatures. These two interactions depict a substantially amorphous (melted) system, except for $\text{Ti}^{3+}\text{-O}^{2-}$ at 0 K.

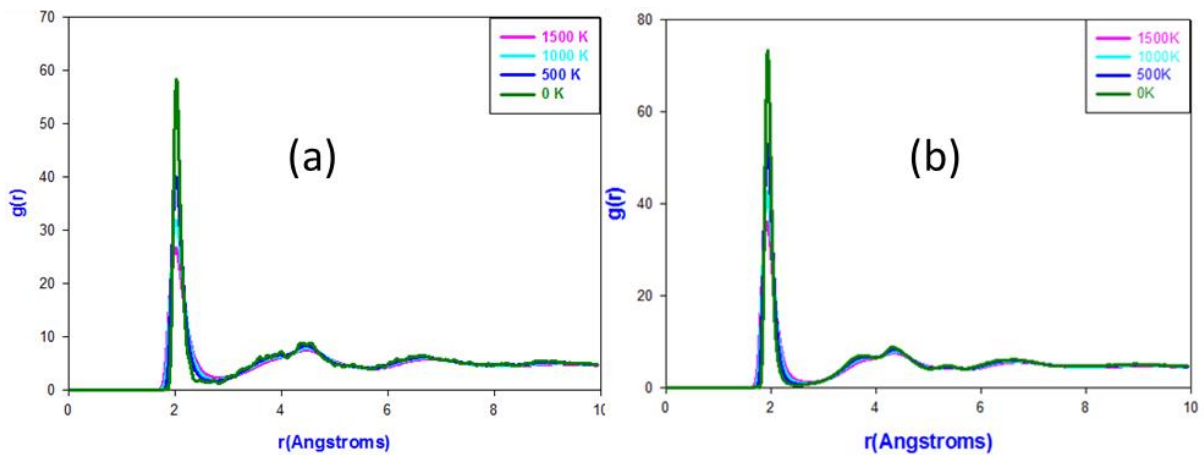


Figure 25: Total RDFs for (a) $\text{Ti}^{3+}\text{-O}^{2-}$ and (b) $\text{Ti}^{4+}\text{-O}^{2-}$ in the TiO_2 nanosphere with 0.07 lithium ion concentrations at different temperatures.

We now consider the radial distribution functions for TiO_2 nanosheets at different Li concentrations. Figure 26 shows RDFs of the $\text{Ti}^{3+}\text{-O}^{2-}$ and $\text{Ti}^{4+}\text{-O}^{2-}$ interactions for 0.03 lithium ion concentration at different temperatures. As always, the first peaks around 2 Å is well defined. All subsequent peaks, at larger radial distances are sharp for both low and high temperatures and this applies for both $\text{Ti}^{3+}\text{-O}^{2-}$ and $\text{Ti}^{4+}\text{-O}^{2-}$ interactions. This reflects high crystallinity of the nanosheets across all temperatures..

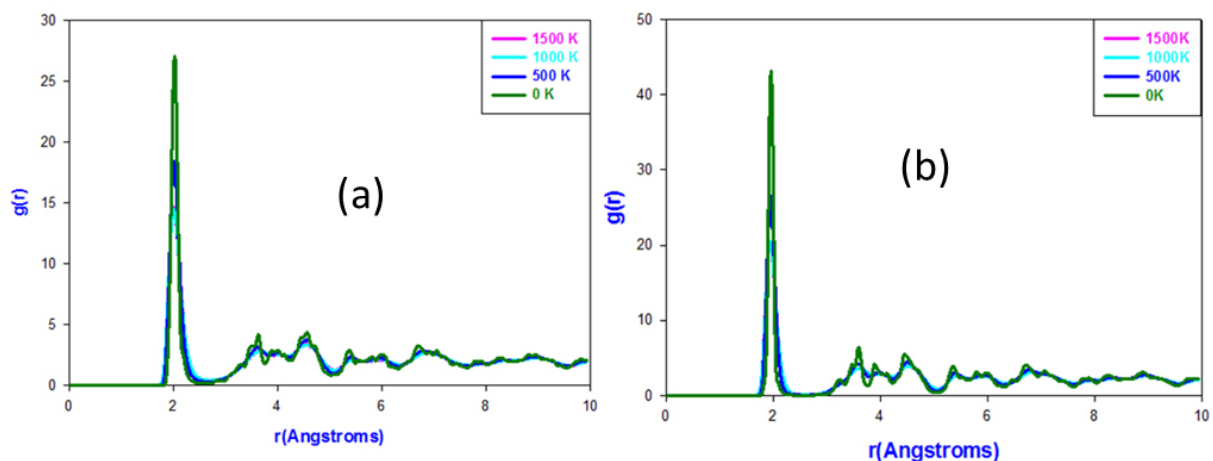


Figure 26: Total RDFs for (a) $\text{Ti}^{3+}\text{-O}^{2-}$ and (b) $\text{Ti}^{4+}\text{-O}^{2-}$ in the TiO_2 nanosheet with 0.03 lithium ion concentration at different temperatures.

Figure 27 shows radial distribution functions for the nanosheet with 0.04 lithium ion concentration. As in the case of figure 26 the peaks corresponding to the $\text{Ti}^{3+}-\text{O}^{2-}$ and $\text{Ti}^{4+}-\text{O}^{2-}$ interactions are well defined with the first peak being the highest. All peaks at larger radial distances corresponding to different temperatures are distinct, attesting to the crystallinity of this Li concentration.

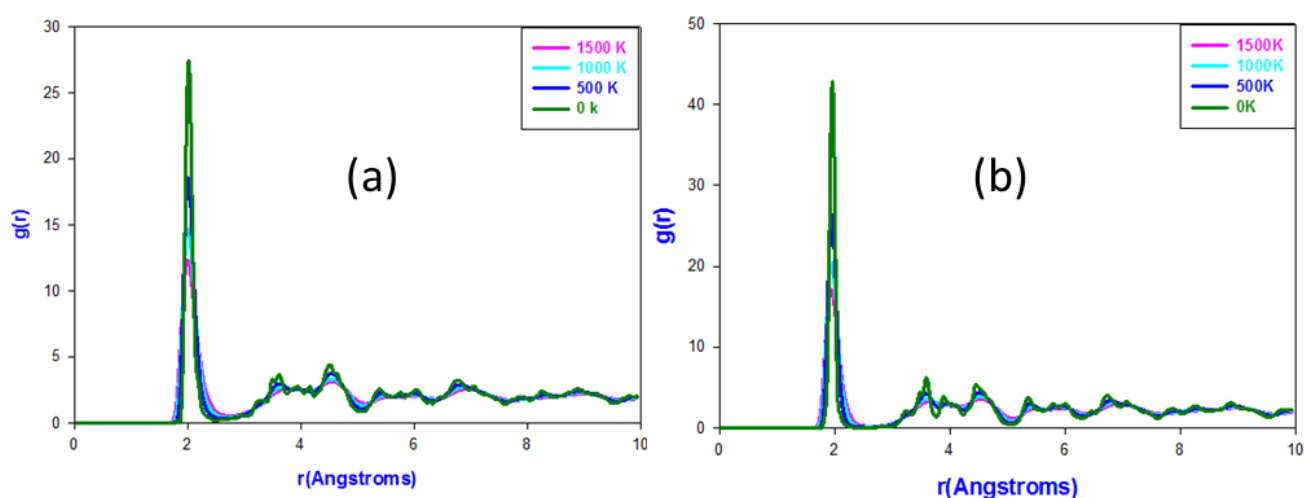


Figure 27: Total RDFs for (a) $\text{Ti}^{3+}-\text{O}^{2-}$ and (b) $\text{Ti}^{4+}-\text{O}^{2-}$ in the TiO_2 nanosheet with 0.04 lithium ion concentration at different temperatures.

Lastly, the radial distribution functions for the nanosheet with 0.07 lithium ion concentration are shown in figure 28. The peaks beyond the first are well defined for all temperatures although they appear to be slightly reduced in intensity compared to those of the 0.03 and 0.04 lithium ion concentrations. This shows that the nanosheets at the highest lithium concentration of 0.07 remain crystalline at all temperatures which is consistent with observed crystal structures.

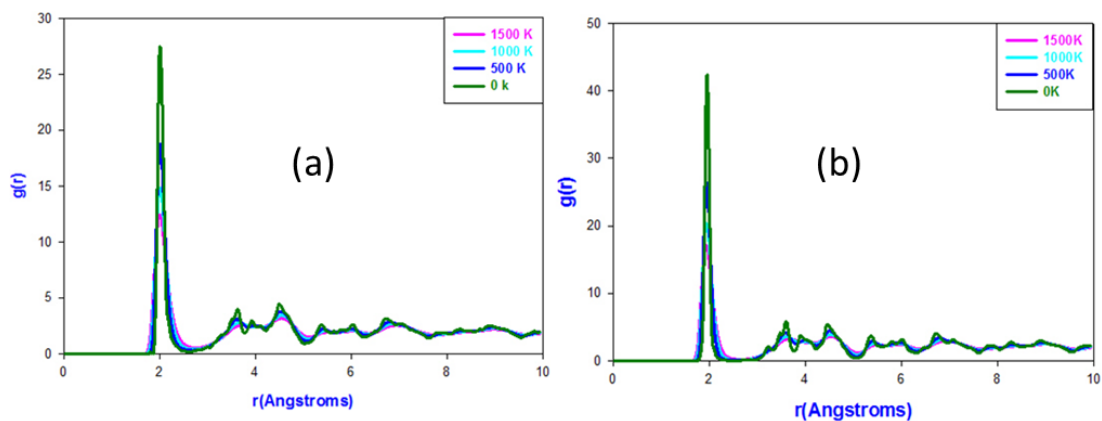


Figure 28: Total RDFs for (a) $\text{Ti}^{3+}\text{-O}^{2-}$ and (b) $\text{Ti}^{4+}\text{-O}^{2-}$ in the TiO_2 nanosheet with 0.07 lithium ion concentration at different temperatures.

Figure 29 features the radial distribution functions (RDF) of the nanoporous structure with 0.03 lithium ion concentration. The plots show that the first $\text{Ti}^{3+}\text{-O}^{2-}$ and $\text{Ti}^{4+}\text{-O}^{2-}$ interaction peaks are well defined and sharp, together with those at higher radial distances from 0 K to the highest temperatures. This attests the crystallinity of the 0.03 concentration nanoporous structure.

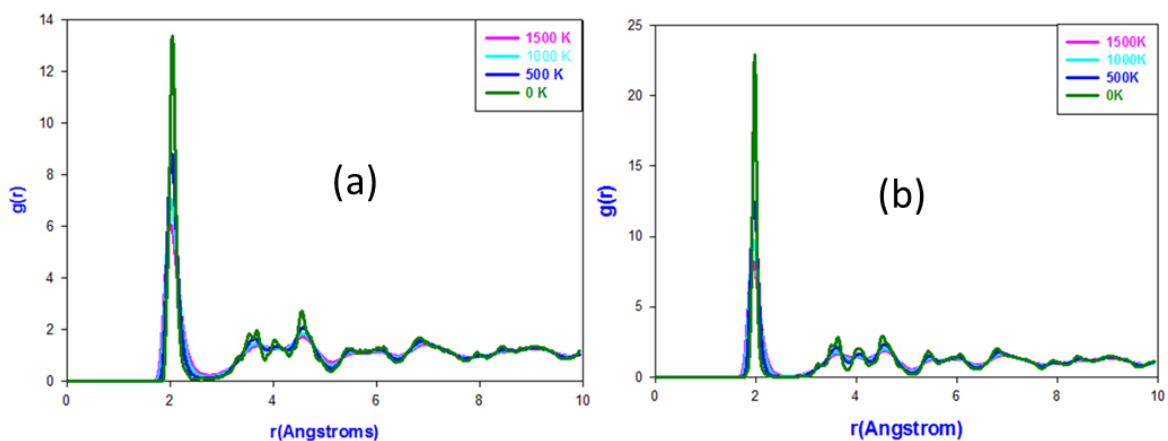


Figure 29: Total RDFs for (a) $\text{Ti}^{3+}\text{-O}^{2-}$ and (b) $\text{Ti}^{4+}\text{-O}^{2-}$ in the TiO_2 nanoporous with 0.03 lithium ion concentration at different temperatures.

Similarly, the radial distribution function (RDF) of porous at different temperature in 0.07 lithium ion concentration are shown in figure 30. The first peaks of the $\text{Ti}^{3+}\text{-O}^{2-}$ and $\text{Ti}^{4+}\text{-O}^{2-}$ interactions have high intensities with the latter enhanced. The peaks at higher radial distances are also sharp and well defined, confirming that the nanoporous structures are crystalline at all temperatures from 0 to 1500K.

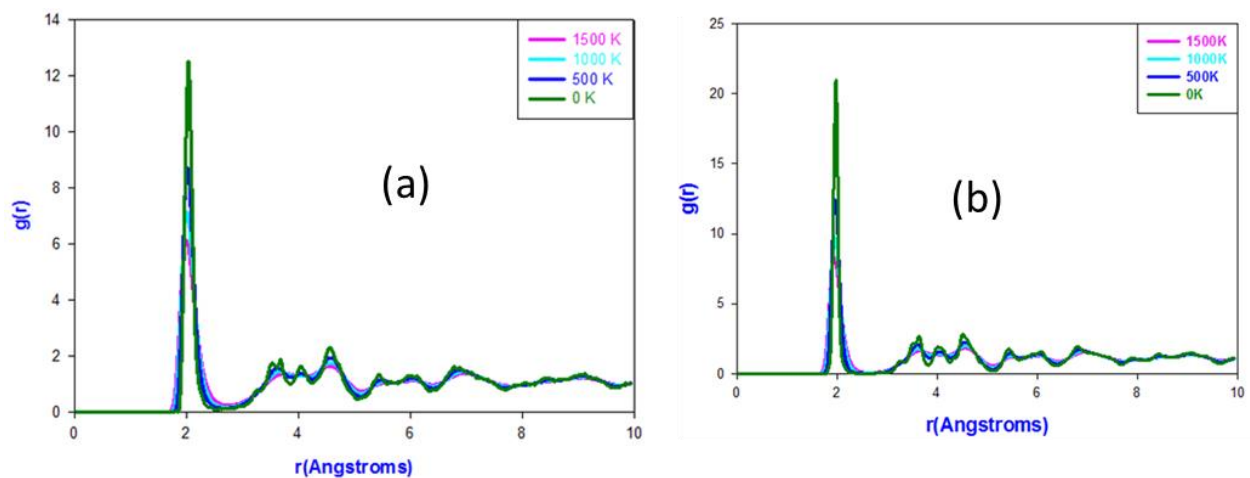


Figure 30: Total RDFs for (a) $\text{Ti}^{3+}\text{-O}^{2-}$ and (b) $\text{Ti}^{4+}\text{-O}^{2-}$ in the TiO_2 nanoporous with 0.07 lithium ion concentration at different temperatures.

The radial distribution functions observed in figure 31 correspond to the bulk TiO_2 with 0.03 lithium ion concentration. The first distinct peaks related to the $\text{Ti}^{3+}\text{-O}^{2-}$ and $\text{Ti}^{4+}\text{-O}^{2-}$ interactions have intensities 10 and 14 respectively. The subsequent peaks at larger radial distances are only sharp at low temperatures for the $\text{Ti}^{3+}\text{-O}^{2-}$ interactions. The peaks tend to be broad for the $\text{Ti}^{4+}\text{-O}^{2-}$ interactions, hence suggesting predominance of an amorphous phase. The radial distribution functions of Figure 31 and those in appendix B14, for 0.04 lithium ion concentration show similar features .

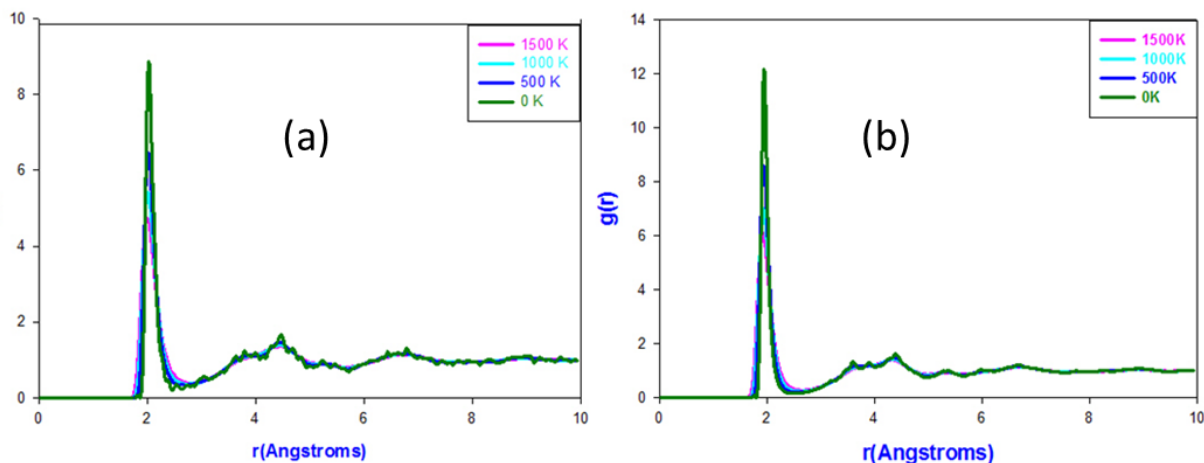


Figure 31: Total RDFs for (a) $\text{Ti}^{3+}\text{-O}^{2-}$ and (b) $\text{Ti}^{4+}\text{-O}^{2-}$ in the TiO_2 bulk with 0.03 lithium ion concentration at different temperatures.

Radial distribution functions (RDF) of the bulk structure with 0.07 lithium ion concentration are presented in figure 32. The first peaks have intensities of 10 and 12 for $\text{Ti}^{3+}\text{-O}^{2-}$ and $\text{Ti}^{4+}\text{-O}^{2-}$ interactions respectively. The lowest temperature structures appear slightly crystalline and those at higher temperatures look amorphous. However, a new structure seems to emerge at the highest temperature of 1500 K. This behaviour of radial distribution functions is different from the ones in figures 31 and appendix B14.

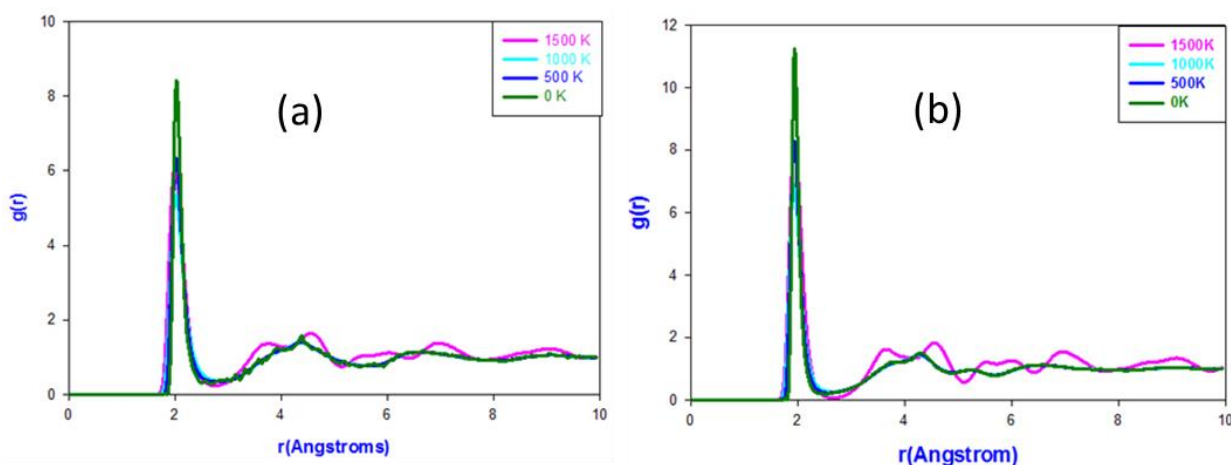


Figure 32: Total RDFs for (a) $\text{Ti}^{3+}\text{-O}^{2-}$ and (b) $\text{Ti}^{4+}\text{-O}^{2-}$ in the TiO_2 bulk with 0.07 lithium ion concentration at different temperatures.

3.1.4 Temperature Variation of Li_xTiO_2 Nano-Architecture Structures

Figure 33 depicts structural changes of TiO_2 nanosphere at increased temperatures with (a) 0.03, (b) 0.04 and (c) 0.07 Li ion concentrations. Structures in (a) and (b) are crystalline, yet structure (c) is not crystalline at all given temperatures. The number of lithium ions at the outer edges increases with an increase in Li-ion concentration which take the trend of (a) < (b) < (c). Structures in (a) and (b) could serve as good anode materials for Li-ion battery compared to the one in (c).

Figure 34 illustrates structural changes of TiO_2 nanosheet at increased temperatures with (a) 0.03, (b) 0.04 and (c) 0.07 lithium ion concentrations. Structures in (a) and (b) do not reflect a high degree of Li aggregation, however (c) has. The structure patterns of the nanosheet TiO_2 seem to be not changing at enhanced temperatures and Li-ion concentrations. Hence figure 34 has a potential of retaining well defined patterns when subjected to high temperatures, thus allowing Li ions to be transported uninterrupted.

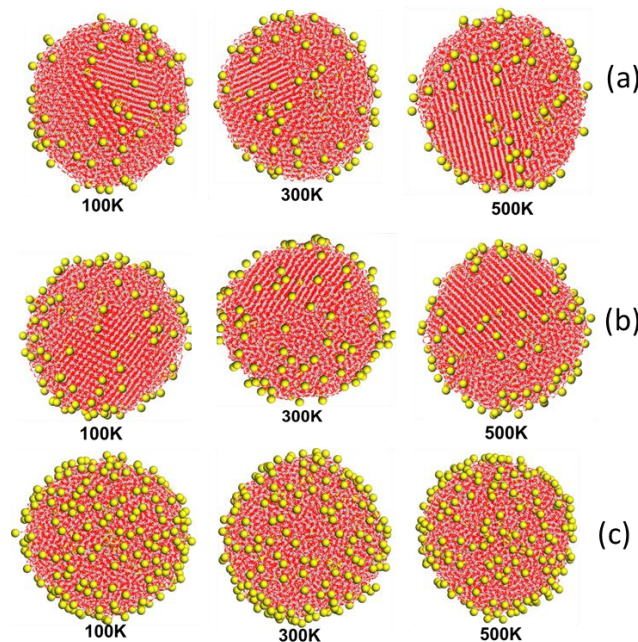


Figure 33: Structural changes of Li_xTiO_2 nanosphere with x of (a) 0.03, (b) 0.04 and (c) 0.07 Li ion concentration with temperatures at 100, 300 and 500 K.

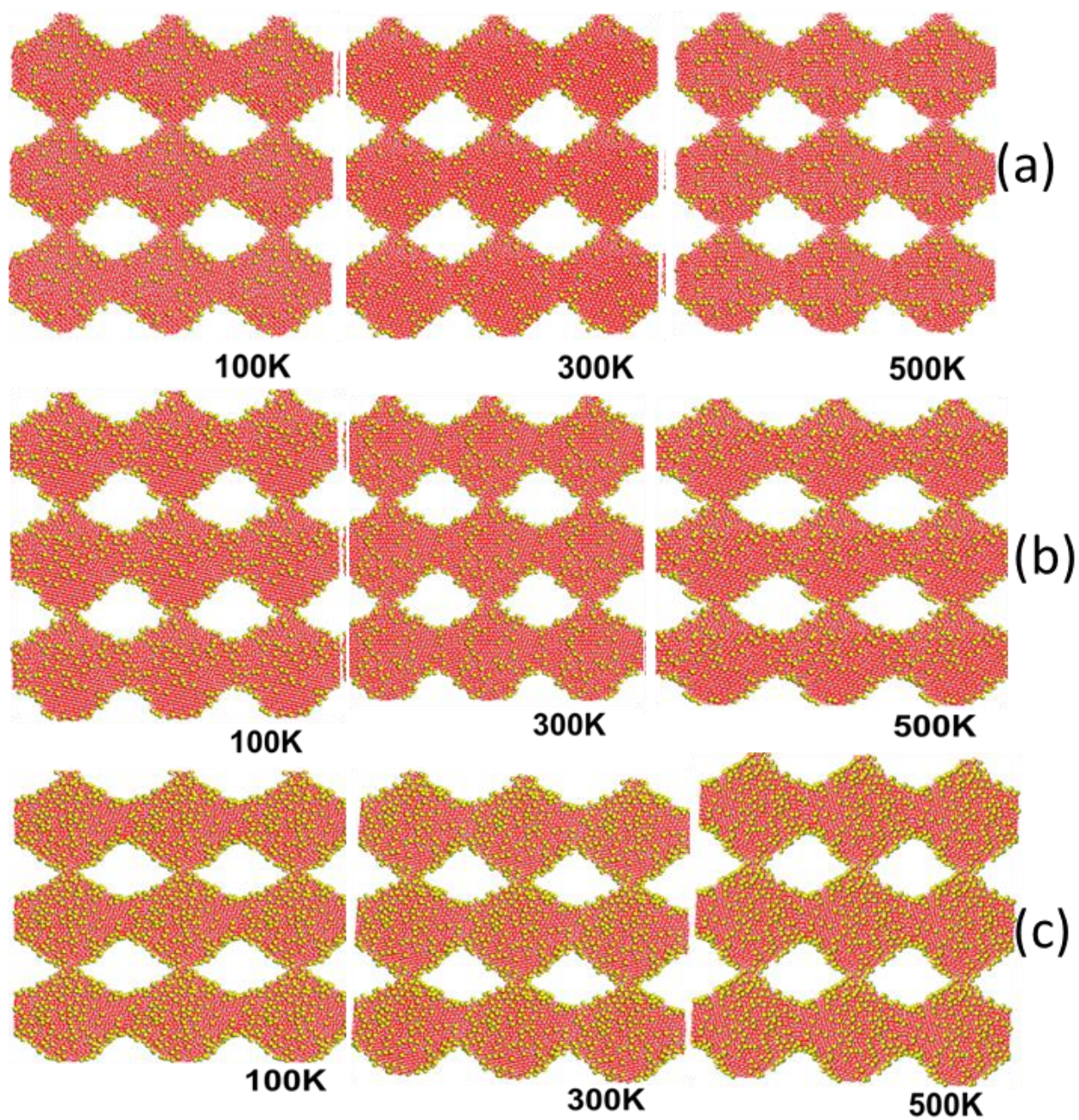


Figure 34: Structural changes of Li_xTiO_2 nanosheet with x of (a) 0.03, (b) 0.04 and (c) 0.07 Li ion concentration with temperatures at 100, 300 and 500 K.

Figure 35 shows structural changes of nanoporous TiO_2 at enhanced temperatures with (a) 0.03, (b) 0.04 and (c) 0.07 lithium ion concentrations. Structures in (a), (b) and (c) are crystalline and accumulation of lithiums is observed on the inside edges of the channels. Structures in (b) and (c) shows a aggregation of Li atoms which appears to increase with Li concentrations. Crystallinity in nanoporous structure shown in (a), (b) and (c) withstands higher temperatures. Its stability proves it can serve as a good anode material for Li-ion batteries.

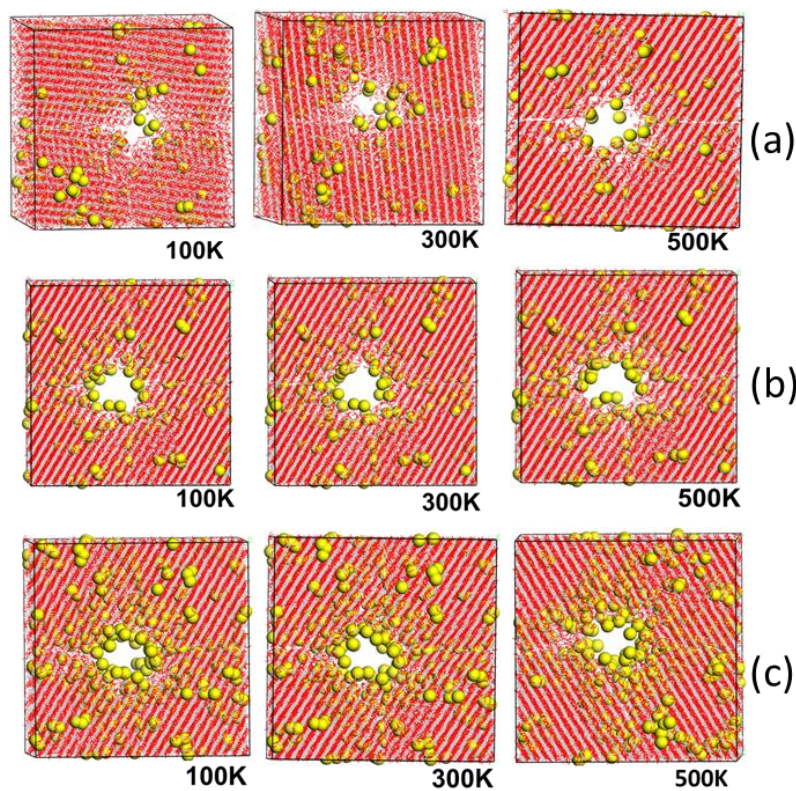


Figure 35: Structural changes of Li_xTiO_2 nanoporous with x of (a) 0.03, (b) 0.04 and (c) 0.07 Li ion concentrations with temperatures at 100, 300 and 500 K.

Figure 36 gives structural changes in the bulk TiO_2 that follows at different temperatures with (a) 0.03, (b) 0.04 and (c) 0.07 lithium ion concentrations. These structures appear to have both crystalline and amorphous forms at all temperatures and concentrations. The influence of temperature appears the same at all Li concentrations. However,

higher Li content seems to enhance the amorphous phase. Such behaviour makes the bulk structure to be unreliable as anode material for Li-ion batteries. For future analysis, an increase in temperature above this range is needed.

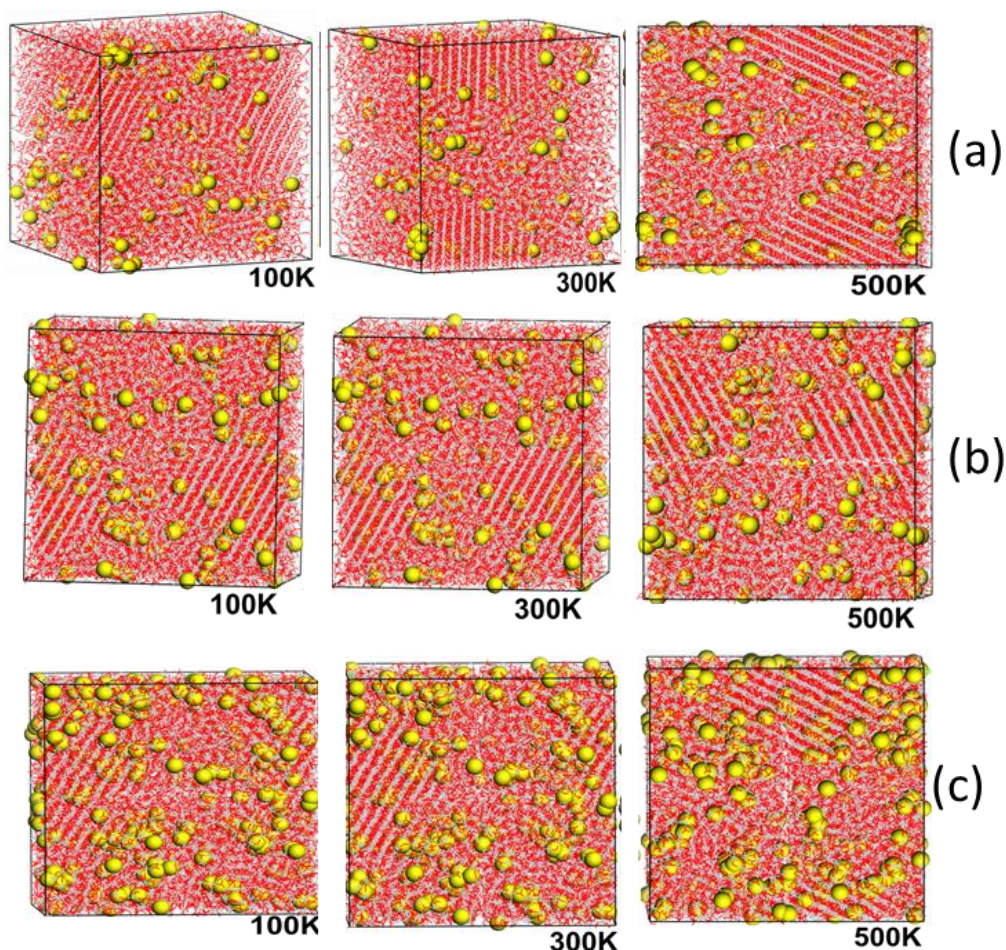


Figure 36: Structural changes of Li_xTiO_2 bulk with x of (a) 0.03, (b) 0.04 and (c) 0.07 Li ion concentrations with temperatures at 100, 300 and 500 K.

3.1.5 X-ray Diffraction Patterns

X-ray diffraction patterns at cooled and higher temperatures on various TiO_2 nano-architectures, with low and high lithium concentrations, were calculated in order to gain further structural understanding. All XRD patterns were determined between 20 and 80 °, where the peak intensities were scaled up for better visualisation. The reference peak positions for TiO_2 and LiTiO_2 with different phases are shown as straight lines in

figure 37. This atomistic simulation procedure allowed us to reveal weak signals from low concentration phases in Li_xTiO_2 . As will be indicated, Figure 39 and 40 show XRDs for nanosheet and nanoporous respectively having dominant and equivalent peaks at 25, 31, 42, 55 and 66 ° while figure 38 and 41 represents XRDs for nanosphere and bulk respectively have equivalent peaks at 30, 42, 55 and 68 °.

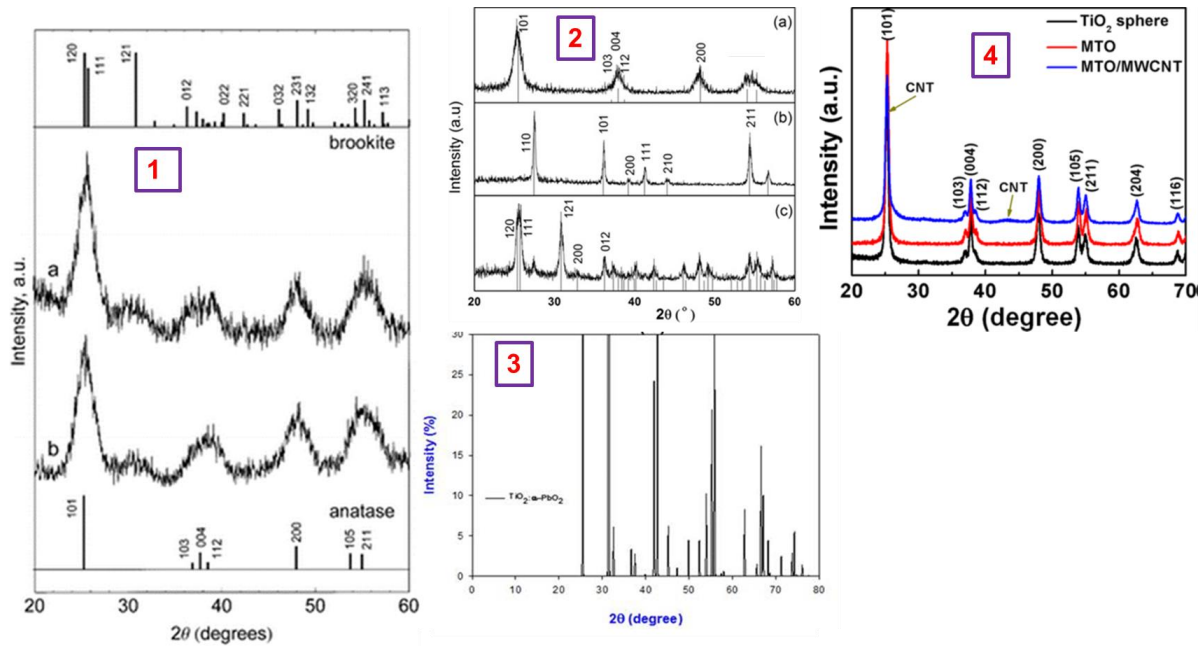


Figure 37: Experimental XRD patterns for 1. TiO₂ (a) Nanorods and (b) Co (II) TiO₂ [47] 2. Pure TiO₂ (a) anatase (b) rutile (c) brookite [22] 3. TiO₂: α -PbO₂. 4. TiO₂ spheres, mesoporous TiO₂ spheres, and MTO/MWCNT composite [33].

Figure 38 shows XRD patterns of the nanosphere cooled to 0 K with 0.03 lithium ion concentration. It has broad peaks full of noise, with peak positions at 2θ between 20 and 40 °, 40 and 45 °, 52 and 58 ° and around 68 ° containing elements of brookite and rutile phases. At 0 K, the 0.07 lithium concentration peak positions at 2θ between 20 and 40 °, 40 and 75 ° are noted with maximum intensity of 8 containing many broad peaks.

Increased temperatures did not affect the XRD patterns of both concentrations since the same peak positions are observed at 0 and 500 K. The set of XRD peaks for the 0.07 Li ion concentration suggests a non-crystalline structure. So the nanosphere system at lower Li ion concentrations can withstand high temperatures, whereas high lithium contents affect the morphology and characteristics of the structure.

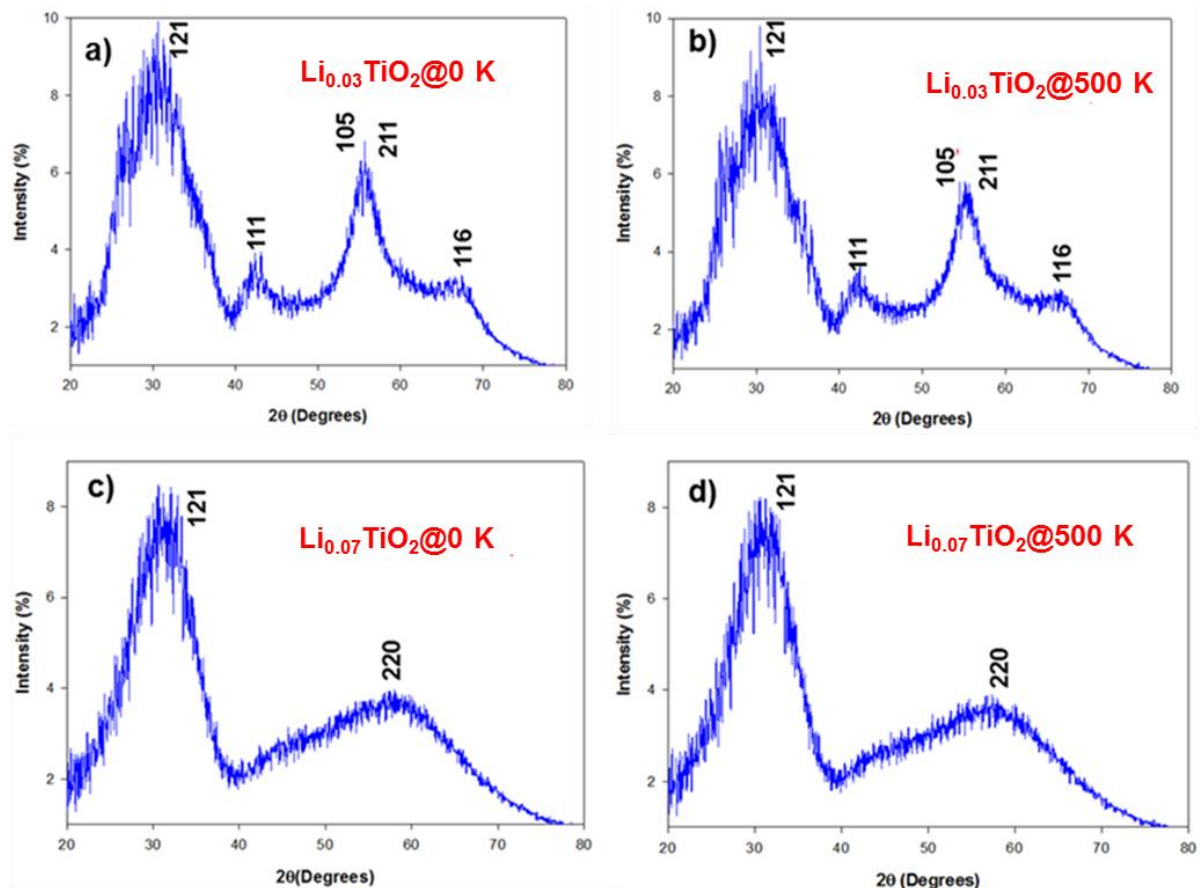


Figure 38: Calculated XRD patterns for nanosphere Li_xTiO_2 (0.03 and 0.07 Li ion concentrations) at 0 and 500 K.

In figure 39, the XRD patterns of the nanosheet at 0 and 500 K for Li_xTiO_2 for $x = 0.03$ and 0.07 are identical, showing the presence of rutile and brookite phases. These XRDs have sharp and broad peaks, high intensities and high signal to background noise. The presence of rutile is shown by a match of the peaks at $2\theta = 39, 41, 44$ and 54° and the presence of peaks at $2\theta = 25, 26$ and 32° indicated that the nanosheet

contains the brookite phase. These XRDs of low and high lithium concentrations differ mainly in intensities of peaks.

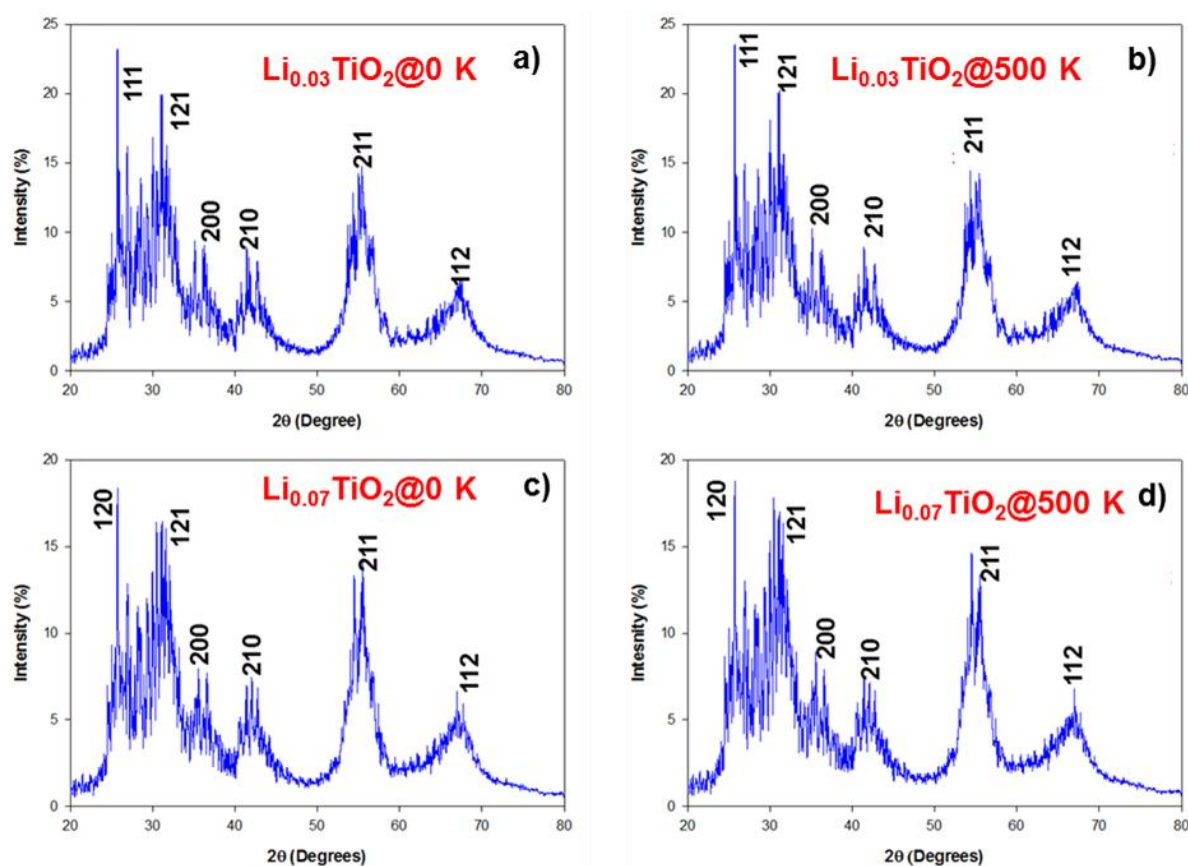


Figure 39: Calculated XRD patterns for nanosheet Li_xTiO_2 (0.03 and 0.07 Li ion concentrations) at 0 and 500 K.

Figure 40 indicates the XRD patterns of the nanoporous structure with sharp peaks of same intensities both at low and high Li concentrations run at 0 and 500 K. The many peaks correlate well with the 2θ angles of all three phases of TiO_2 shown in figure 38. It also shows that the same pattern persists for both lithium concentrations and temperatures. The XRD patterns for bulk Li_xTiO_2 at 0 and 500 K with $x = 0.03$ and 0.07, in figure 41, have one sharp, very broad peak with low signal to background noise peaks. A brookite polymorph is observed here, which coincide well with peak at $2\theta = 25, 26$ and 58° in figure 38.

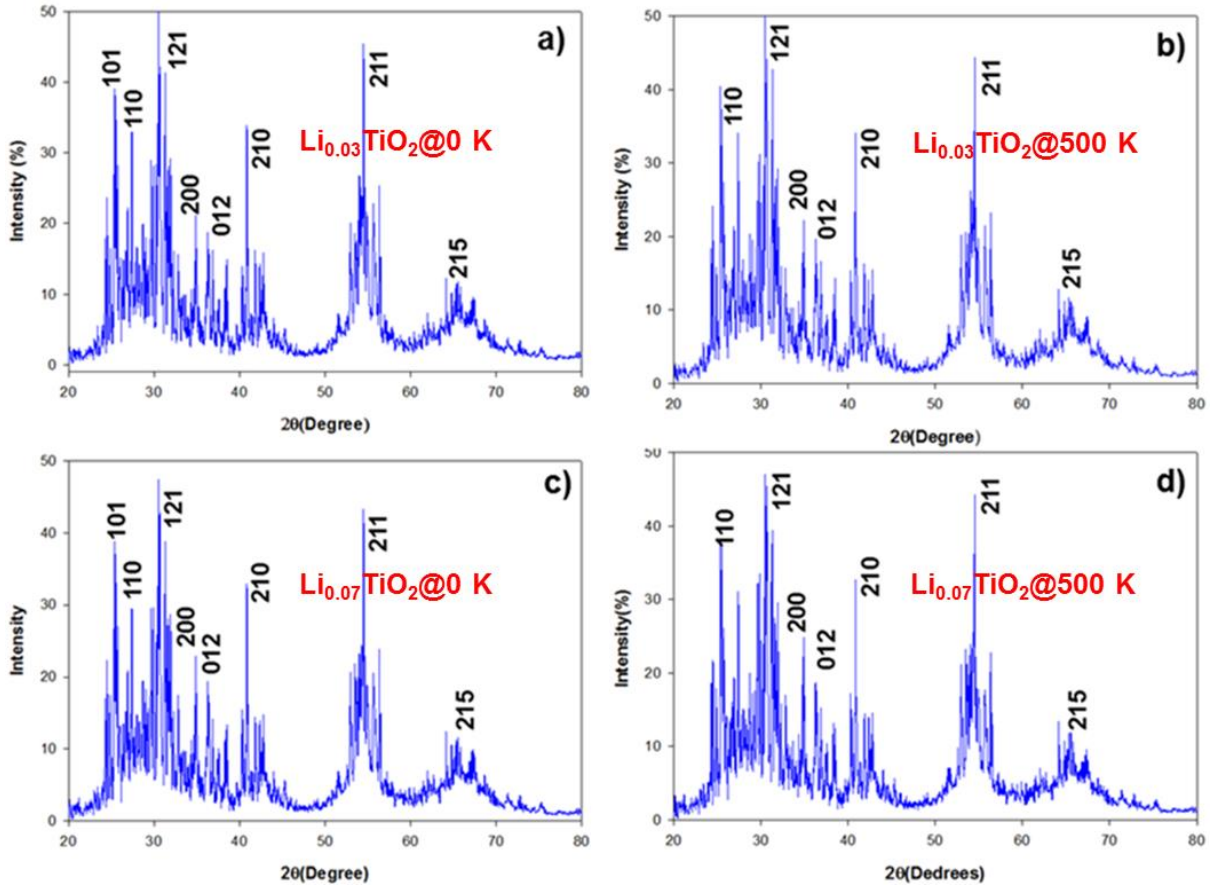


Figure 40: Calculated XRD patterns for nanoporous Li_xTiO_2 (0.03 and 0.07 Li ion concentrations) at 0 and 500 K.

There is slight possibility of the presence of orthorhombic ramsdellite-type crystal structure but the results are not conclusive because the spectrum is noisy and very poor, hence complicating differentiation of peaks. All four XRDs patterns have the strongest peak at $2\theta = \sim 26^\circ$ but broad a peak at $2\theta = \sim 48^\circ$ is only observed on 0.03 lithium concentration it and disappears at 0.07 lithium concentration.

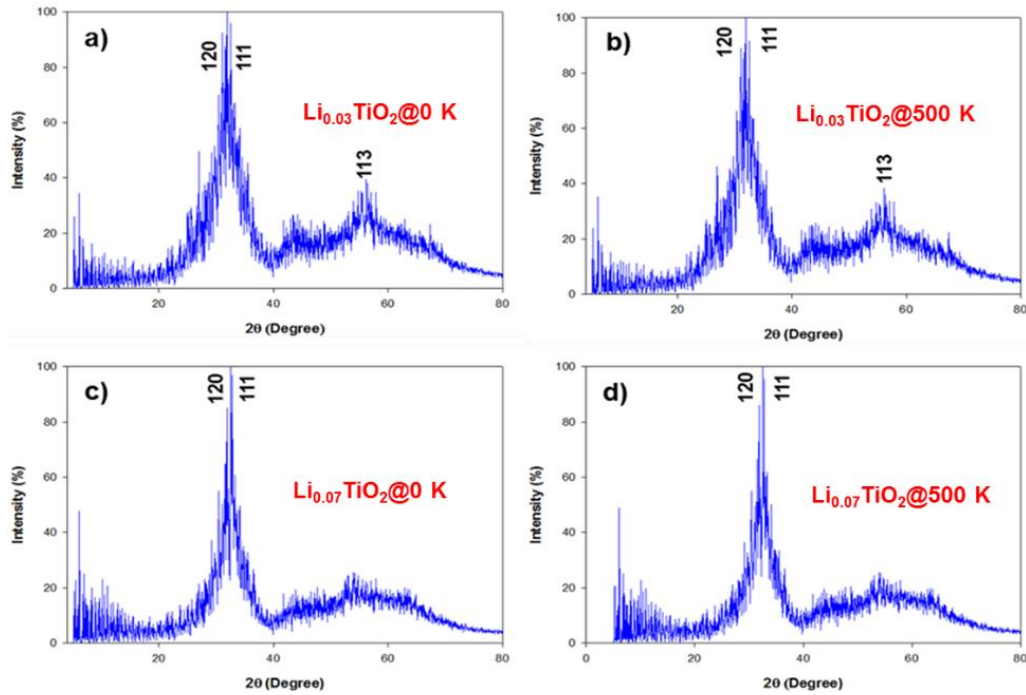


Figure 41: Calculated XRD patterns for bulk Li_xTiO_2 (0.03 and 0.07 Li ion concentrations) at 0 and 500 K.

3.1.6 Microstructures

In order to depict the presence of internal interfaces of grain boundaries evolving due to recrystallisation and phase transition, microstructural snapshots of cooled structures at 0 K and higher temperatures of 500 K will be subsequently shown. In figure 42, the blue colour is associated with the upper layer of Ti^{4+} octahedra while the white colour is the lower layer of Ti^{4+} octahedra. The presence of zigzag chains indicates the brookite domain whilst the straight chains show twinned rutile phases. Figure 44 depicts snapshot of the cut slices for TiO_2 nanosphere at low (0 K) and high (500 K) temperatures with (a) 0.03, (b) 0.04 and (c) 0.07 lithium ion concentrations. The microstructures have patterns of straight tunnels shown by blue circles, which are associated with twinned rutile structure and zigzag tunnels shown by hexagonal black shape, which is associated with the brookite polymorph. This is in agreement with the XRD patterns in figure 38.

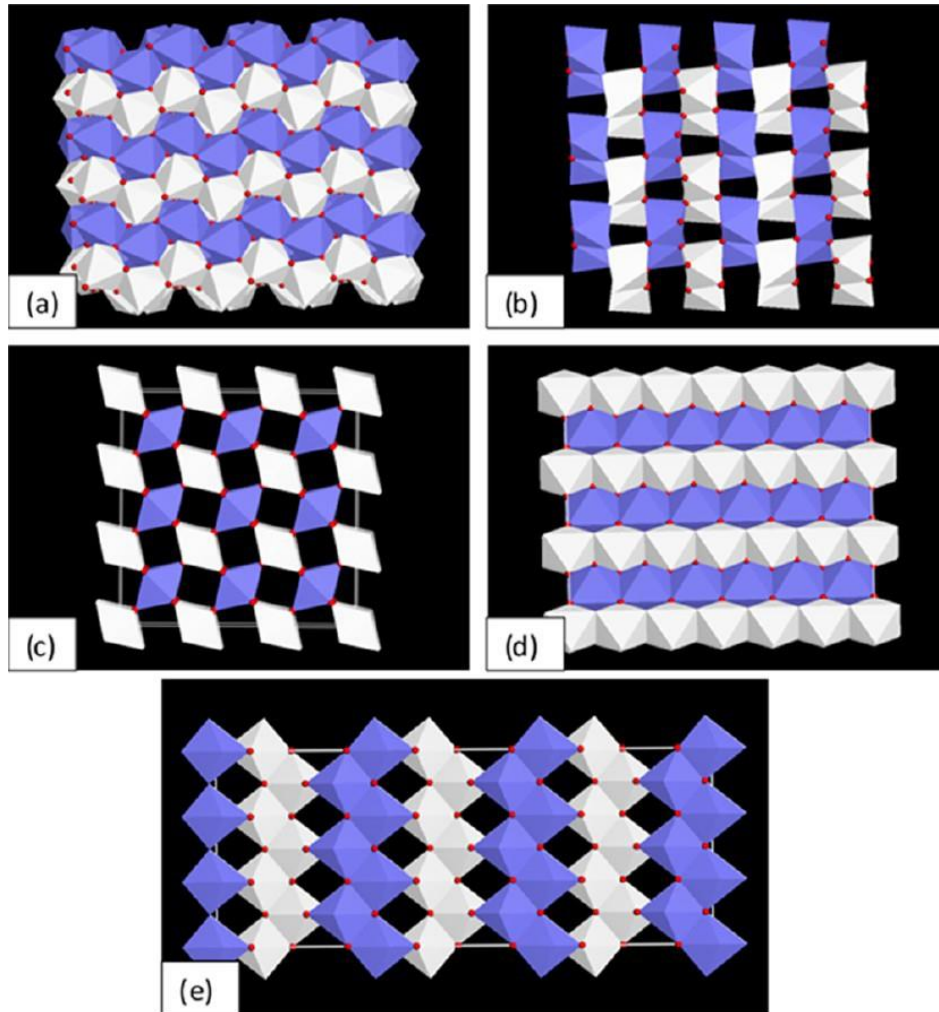


Figure 42: Polymorphic crystal structures of brookite (a,b), rutile (c,d), and anatase (e), showing the zigzag (brookite) and straight (rutile) 1×1 tunnels. Views depict: (a) brookite [100]; (b) brookite [001]; (c) rutile [001]; (d) rutile [100]; (e) anatase [100].[77]

Vacancies filled with lithiums in yellow are shown by a rounded red rectangle shape and the ramesdellite- LiTi_2O_4 pattern in a regular green pentagon shape are observed on (a) and (b). However, (c) has no patterns indicating a disordered system. A low lithium concentration nanosphere can be a good anode battery material candidate, however, one with higher concentrations may not be suitable, this observation holds for 0 and 500 K.

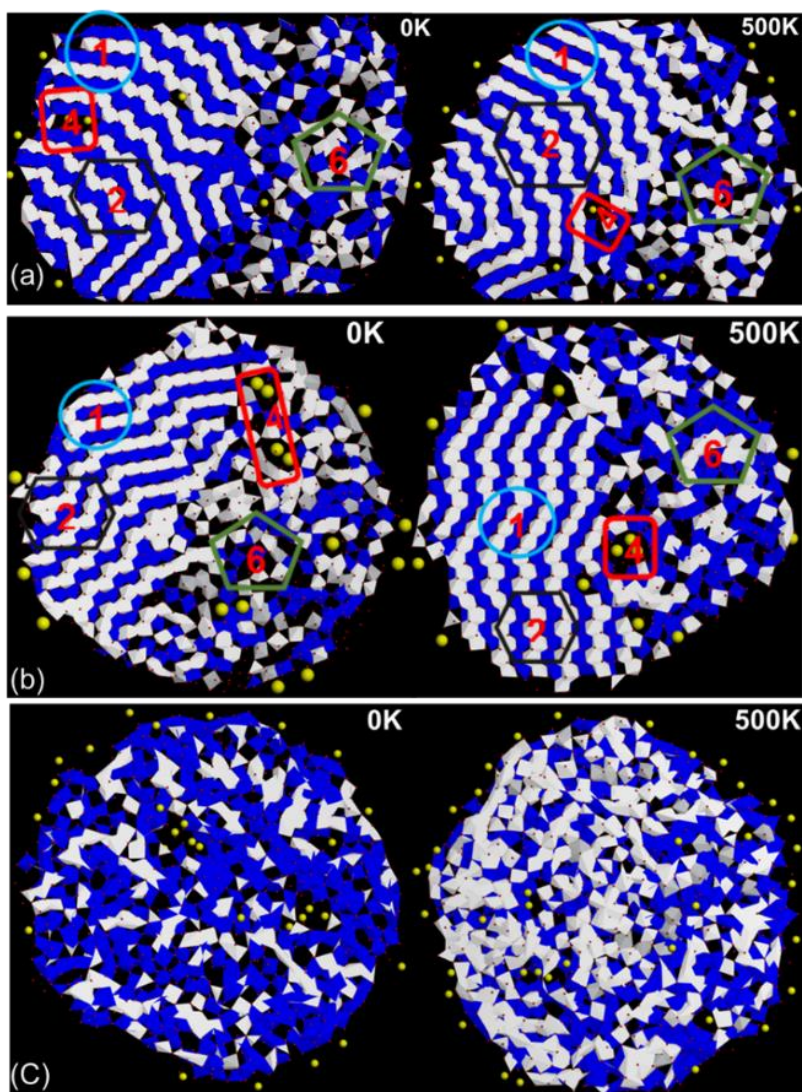


Figure 43: Microstructures of nanosphere TiO_2 at 0 and 500 K with a) 0.03, b) 0.04 and c) 0.07 Li ion concentrations.

Figure 44 depicts graphical representation of a cut slices for TiO_2 nanosheet at 0 K and 500 K with a) 0.03, b) 0.04 and c) 0.07 lithium ion concentrations. The slices have partly a crystalline phase with straight tunnels¹ associated with twinned rutile structure, zigzag tunnels² related to the brookite polymorph, this are the same patterns observed on the XRDs in figure 39 and vacancies filled with few lithiums⁴. Such composite patterns are maintained at different temperatures and lithium concentrations of the nanosheet. In addition, within these microstructures change of orientation of grains is observed at low and high temperatures.

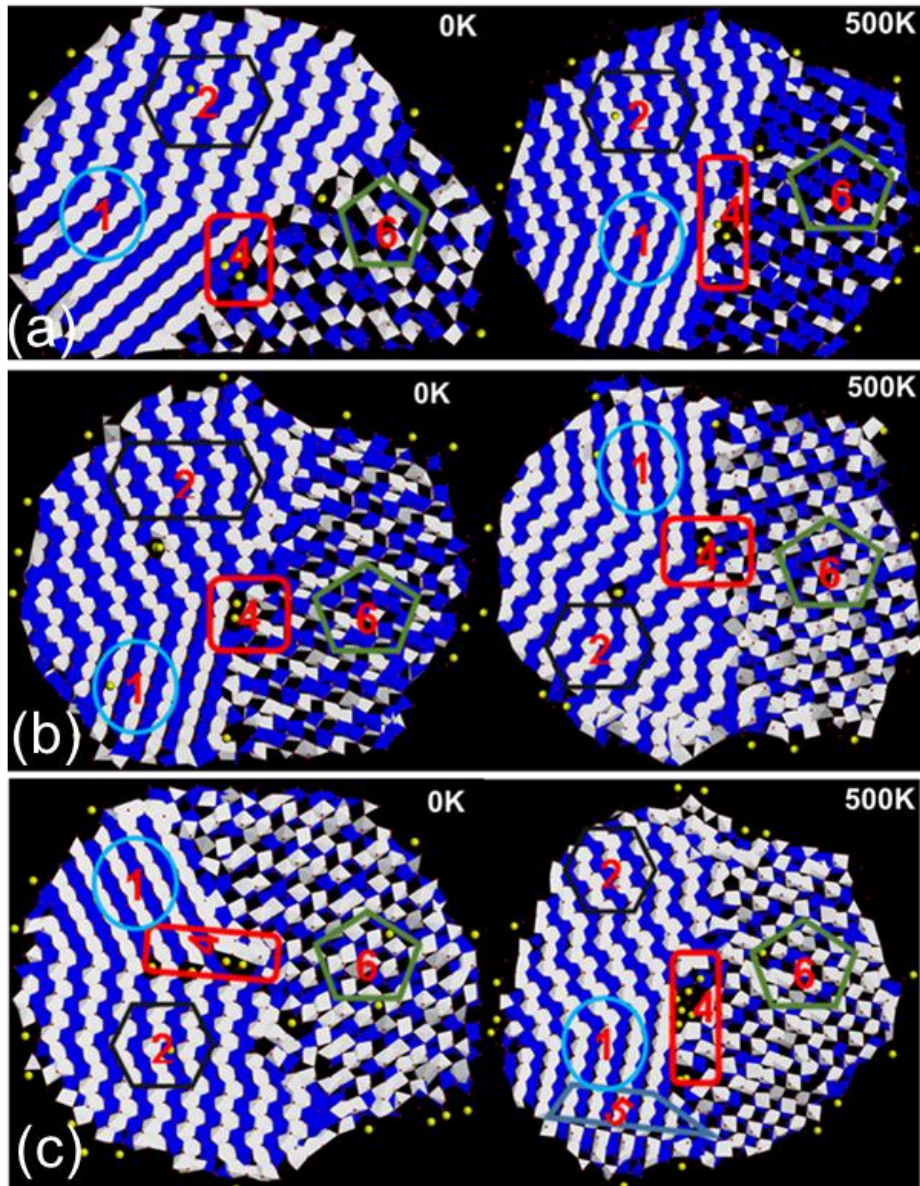


Figure 44: Microstructures of nanosheet TiO₂ at 0 and 500 K with a) 0.03, b) 0.04 and c) 0.07 Li ion concentrations.

The microstructures of the nanoporous TiO₂ with a) 0.03, b) 0.04 and 0.07 lithium ion concentrations at 0 and 500 K are shown in figure 45. The slices reflect a composite crystalline phase with straight tunnels¹ related with twinned rutile structure, zigzag tunnels² associated to the brookite polymorph, vacancies³ and stack defect⁵ where some vacancies are filled with lithiums⁴.

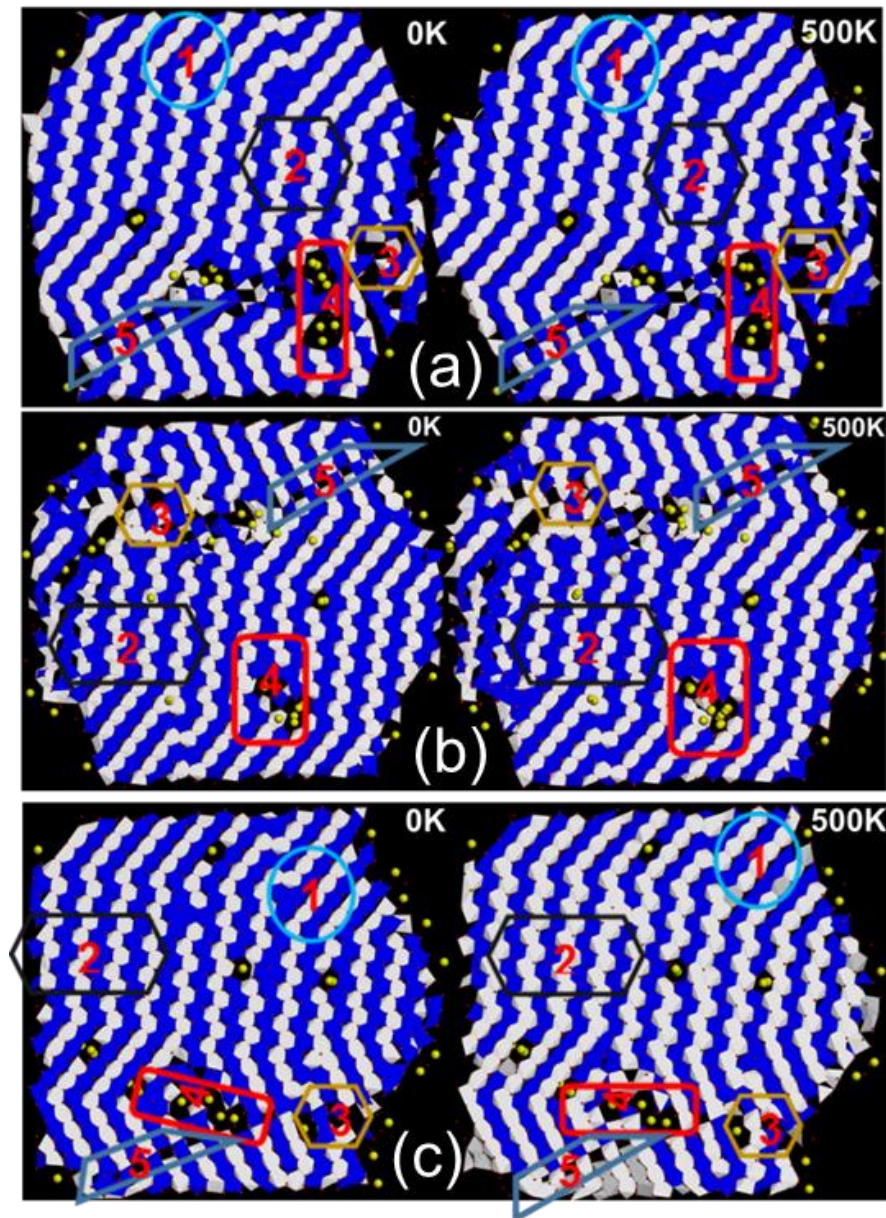


Figure 45: Microstructures of TiO₂ nanoporous at 0 and 500 K with a) 0.03, b) 0.04 and c) 0.07 Li ion concentrations.

The crystal phases are exactly similar to those in figure 40. The concentration of lithium appears to have no effect on the presence of the polymorphs, although the arrangements of the tunnels are altered. This verifies that the tunnels can withstand higher temperatures and lithium concentrations in the TiO₂ nanoporous architectures. Hence rendering it suitable for anode Li ion batteries.

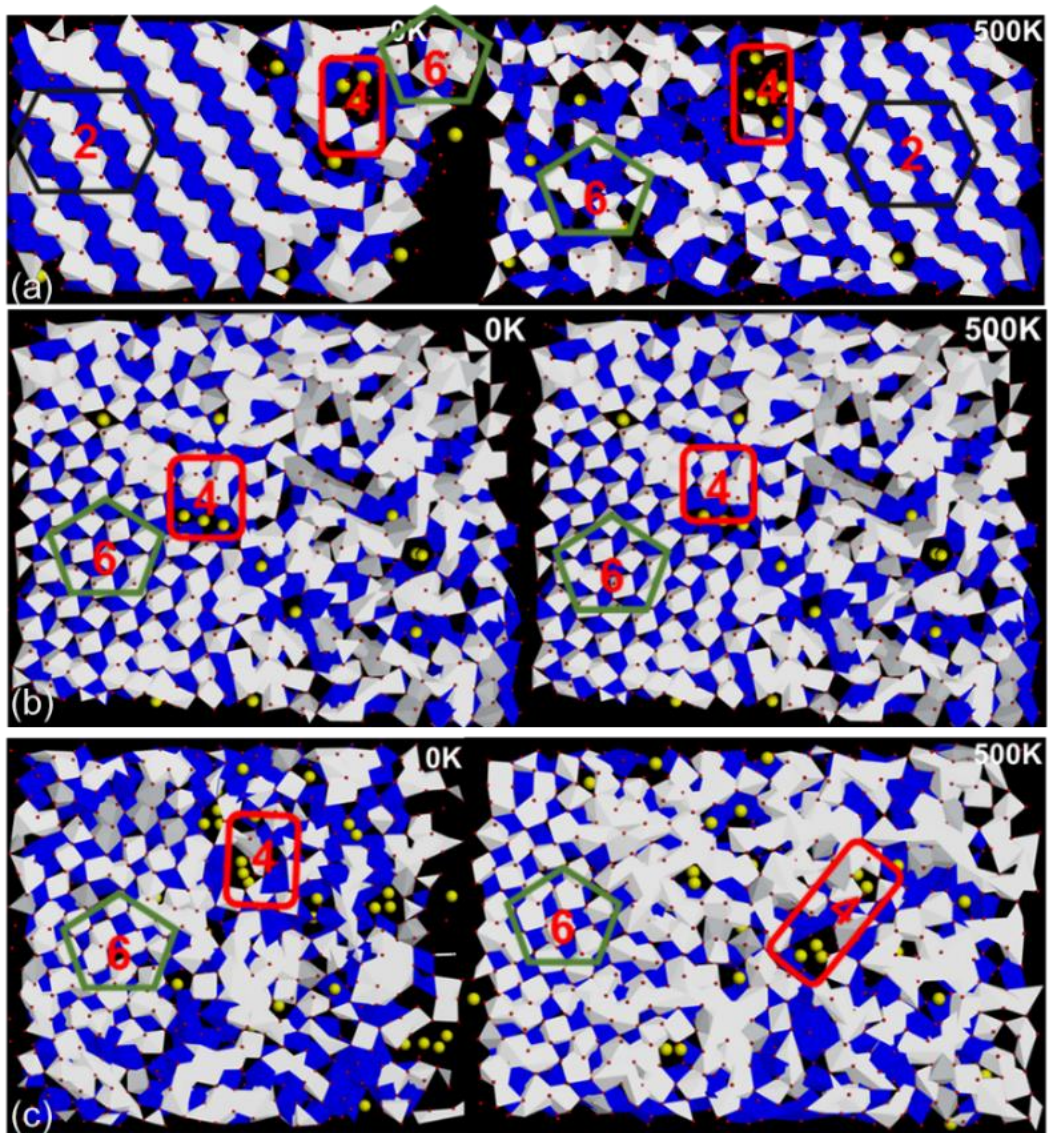


Figure 46: Microstructures of bulk TiO_2 at 0 and 500 K with a) 0.03, b) 0.04 and c) 0.07 Li ion concentrations.

Figure 46 depicts microstructures of the bulk TiO_2 at 0 and 500 K with a) 0.03, b) 0.04 and c) 0.07 lithium ion concentrations containing few internal interfaces. The slices have zigzag tunnels² associated with the brookite polymorph, vacancies filled with lithiums⁴ and ramsdellite- LiTi_2O_4 ⁶ pattern are observed at 0 and 500 K with 0.03 lithium ions in (a). The complex microstructures in figure 46 correlate well with the calculated XRDs in figure 41. Higher temperatures and number of lithiums have both affected the microstructure. Whereas (a) is fully crystalline and with partly defined

tunnels, (b) and (c) are significantly disordered with limited pathways for lithiums. The bulk structure is consequently, not suitable for use as anode in lithium ion batteries.

3.1.7 Transportation

Examination of the Li-ion transport properties of Li_xTiO_2 is of vital importance when considering electrode kinetics. Of primary interest, here is information on the atomistic mechanism in lithium-ion diffusion, which is difficult to probe purely by experimental methods. Molecular dynamics (MD) techniques are well suited to probing transport mechanism, especially cooperative or correlated ion motion. Here, MD calculations over a long simulation time scale were carried out at temperatures, more than typical battery operating temperatures, to study the motions of both anion and cations for the three Li compositions.

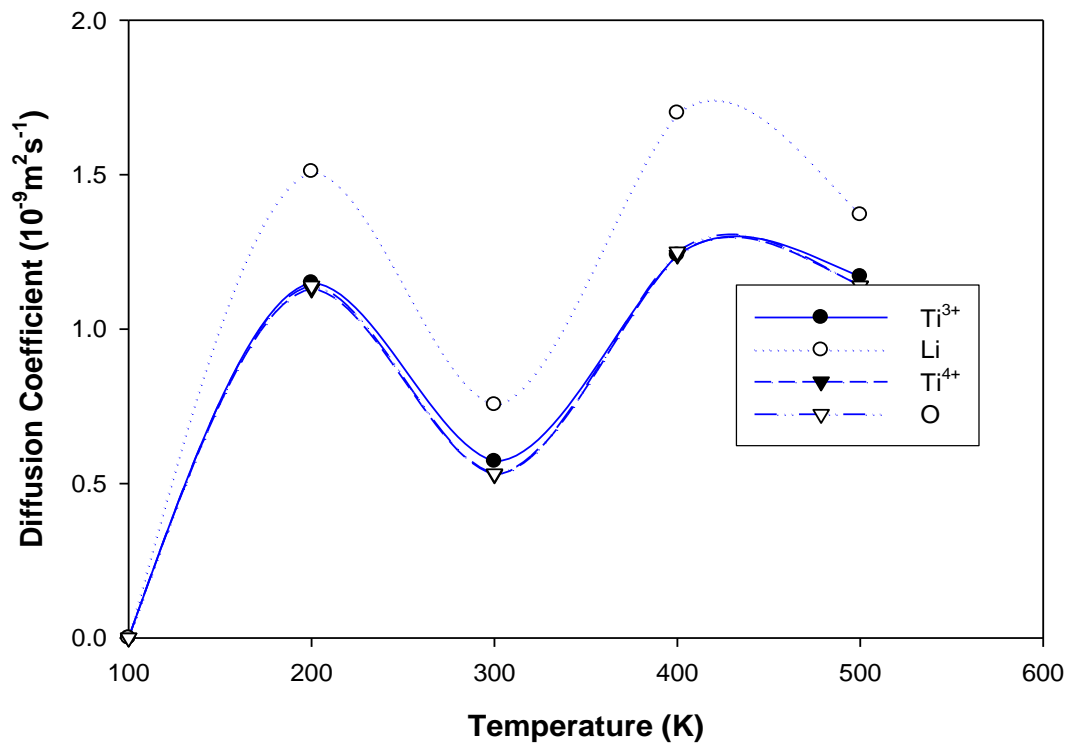


Figure 47: Variation of Ti^{3+} , Li, Ti^{4+} and O diffusion coefficient with temperature in the nanosphere of TiO_2 with 0.03 Li ion concentration.

Figures 47 to 58 show diffusion coefficients of Ti^{3+} , Li, Ti^{4+} and O ions in a nanosphere, nanosheet, nanoporous and bulk structure at various temperatures for different lithium content.. As illustrated in figure 47, the diffusion coefficients (DC) of all ions in a $\text{Li}_{0.03}\text{TiO}_2$ nanosphere follow a near sinusoidal curve as the temperature is increased, with a maxima occurring at around 300 and 400 K, and a minimum close to 300 K. This could only imply that this structure cannot withstand this temperature range. The Li ions diffusion reflects a similar trend but with enhanced diffusion coefficient.

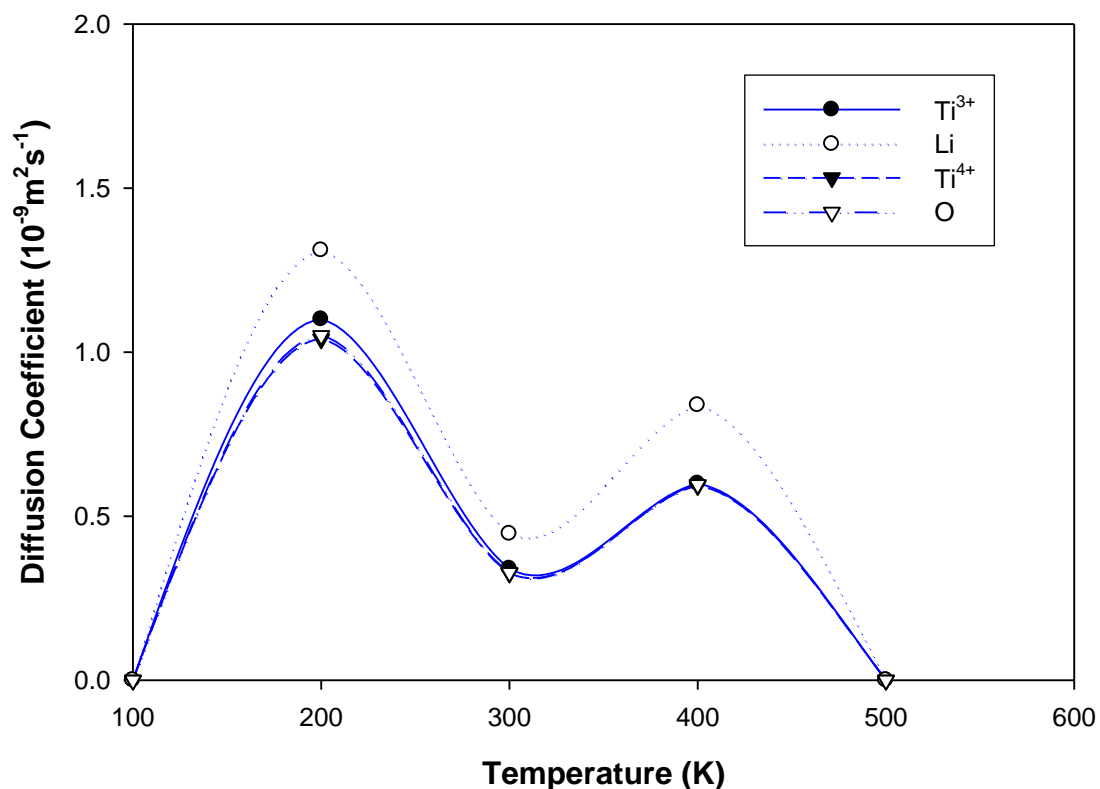


Figure 48: variation of Ti^{3+} , Li, Ti^{4+} and O diffusion coefficients with temperatures in the nanosphere of TiO_2 with 0.04 Li ion concentration.

A similar shaped curve is observed in figure 48 for a nanosphere with 0.04 lithium ions where the minima and second maxima was reduced in magnitude. No diffusion is observed at 100 and 500 K at this Li concentration.

Figure 49 of the TiO₂ nanosphere with 0.07 Li, also depicts a near sinusoidal shape but with high ion diffusion coefficients at 100 K. Although this different behaviour is not fully understood, corresponding microstructures in figure 42 (c), show that the structure is completely disordered at 0 and 500 K, unlike those with 0.03 and 0.04 Li ion concentrations.

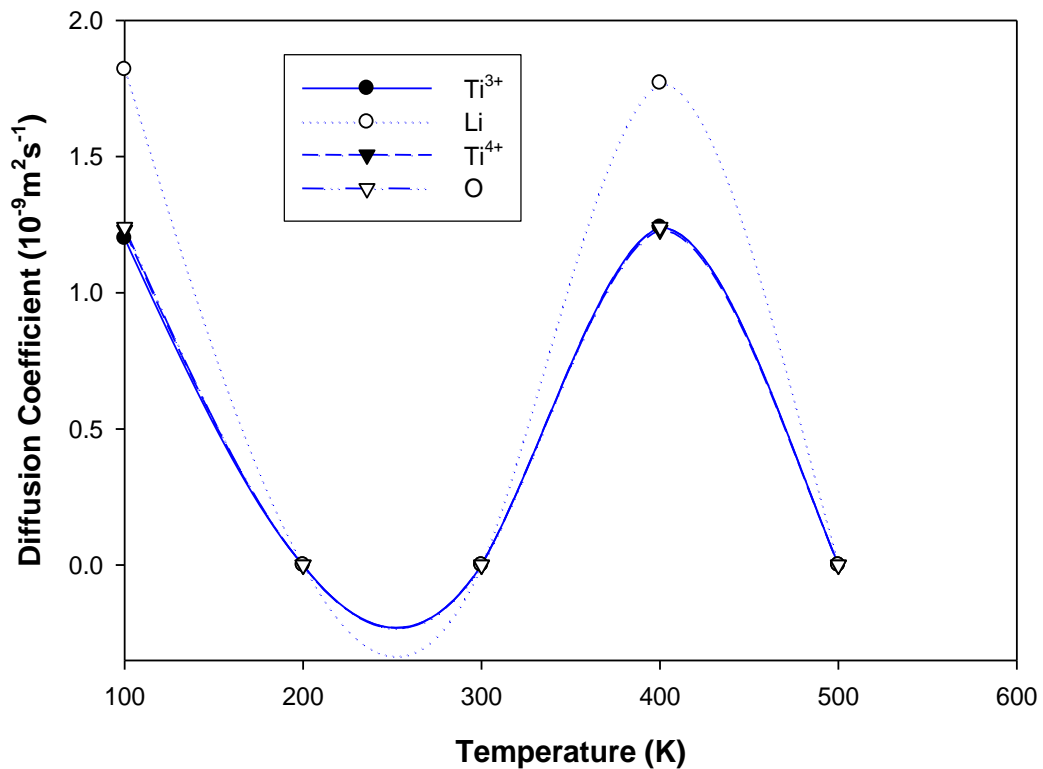


Figure 49: Variation of Ti³⁺, Li, Ti⁴⁺ and O diffusion coefficient with temperature in the nanosphere of TiO₂ with 0.07 Li ion concentration.

Figure 50 indicates that the Li ions of the TiO₂ nanosheet obviously start to diffuse rapidly at 300 K up to 500 K, while oxygen and titanium cations retain zero diffusion coefficient. Figure 51 of the TiO₂ nanosheet with 0.04 Li ions; show no diffusion of any ions from 100 to 200 K. However, Li ions start to diffuse very slowly from 200 to 400 K. The diffusion increases rapidly above 400 K while other ions do not diffuse up to 500 K. So 200 K is needed to initiate diffusion in a nanosheet TiO₂ structure inserted with 0.04 Li ion concentration after being cooled.

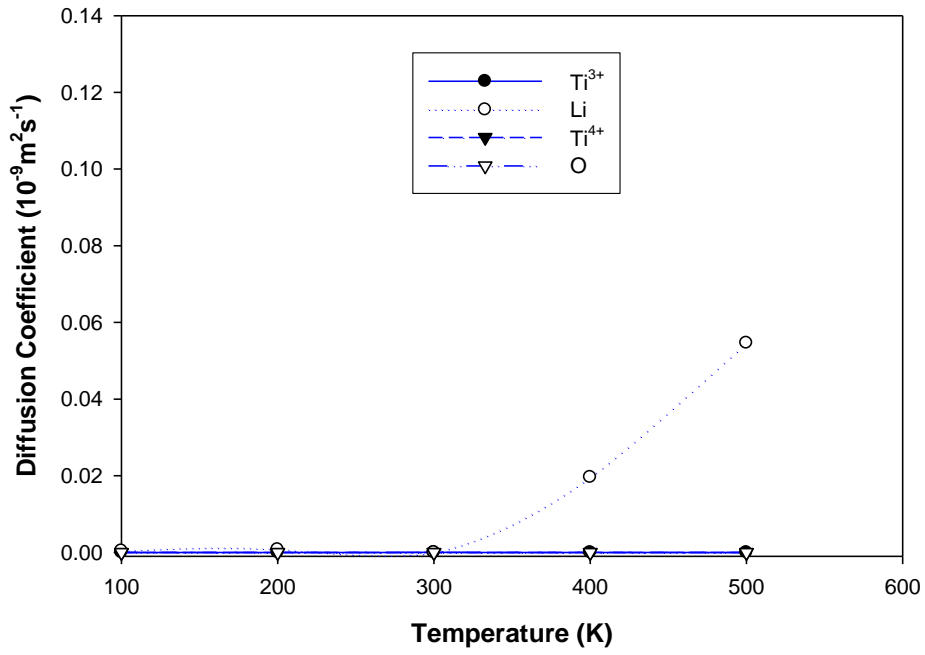


Figure 50: Variation of Ti³⁺, Li, Ti⁴⁺ and O diffusion coefficient with temperature in the nanosheet TiO₂ with 0.03 Li ion concentration.

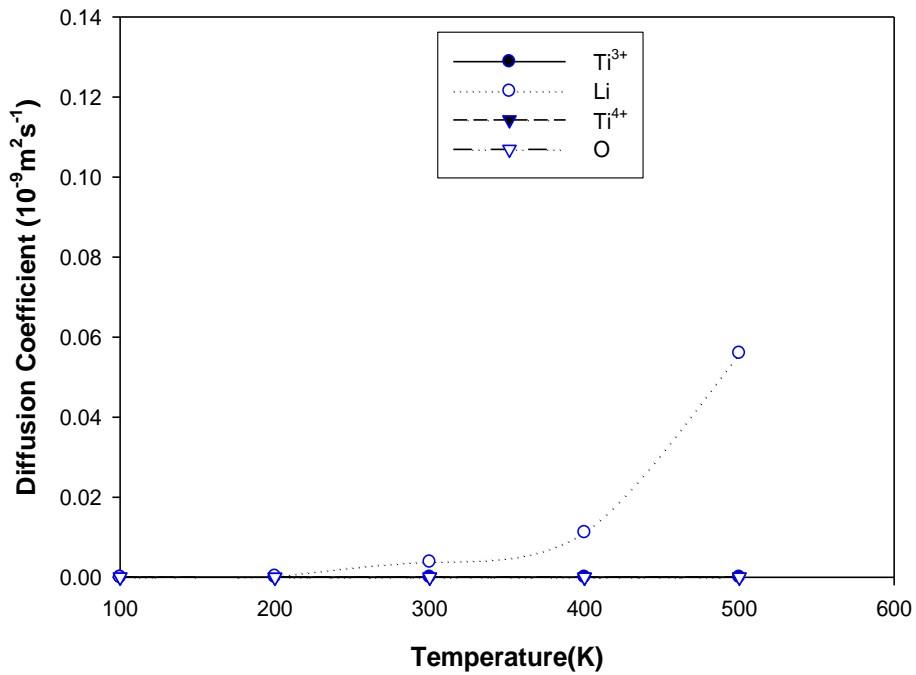


Figure 51: Variation of Ti³⁺, Li, Ti⁴⁺ and O diffusion coefficient with temperature in the nanosheet TiO₂ with 0.04 Li ion concentration.

Figure 52 has similar shape curve for variation of diffusion coefficient at increased temperature in the nanosheet TiO₂ with 0.07 Li ion concentration. Diffusion coefficient

of Li ions is rapidly enhanced at higher temperatures while keeping other atoms at zero. Increased temperatures and Li concentrations have raised diffusion of atoms in the nanosheet while maintaining its original structure; this is in agreement with the cut slices in figure 44 (a), (b) and (c).

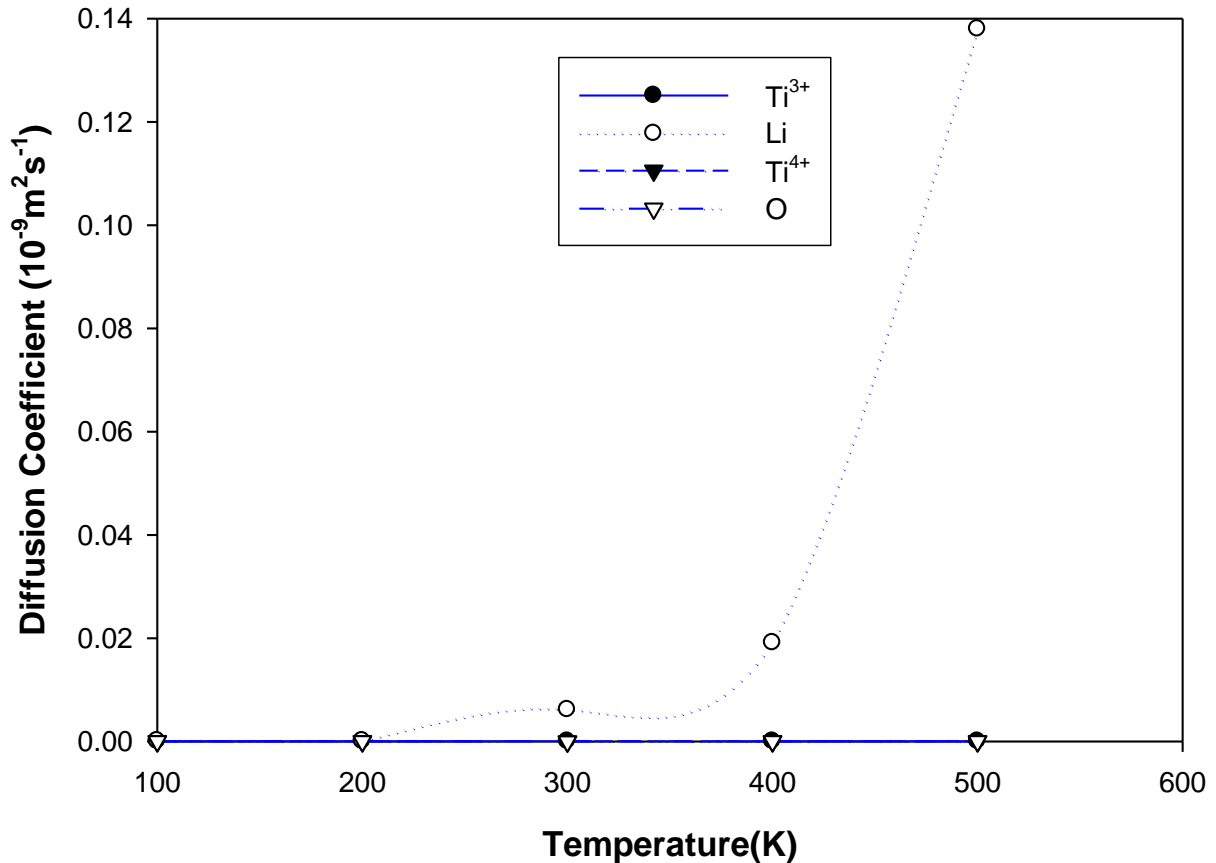


Figure 52: Variation of Ti³⁺, Li, Ti⁴⁺ and O diffusion coefficients with temperatures in the nanosheet TiO₂ with 0.07 Li ion concentration.

Figure 53 presents behaviour of diffusion coefficients as the temperature is increased in the nanoporous TiO₂ with 0.03 Li ion concentrations; Li diffusion commences at 200 K and increased linearly up to 400 K followed by an abrupt change at higher temperatures. The constant zero diffusion of other ions such as titanium and oxygen throughout given temperatures, confirms the presence of the crystalline phases in figure 45 (a).

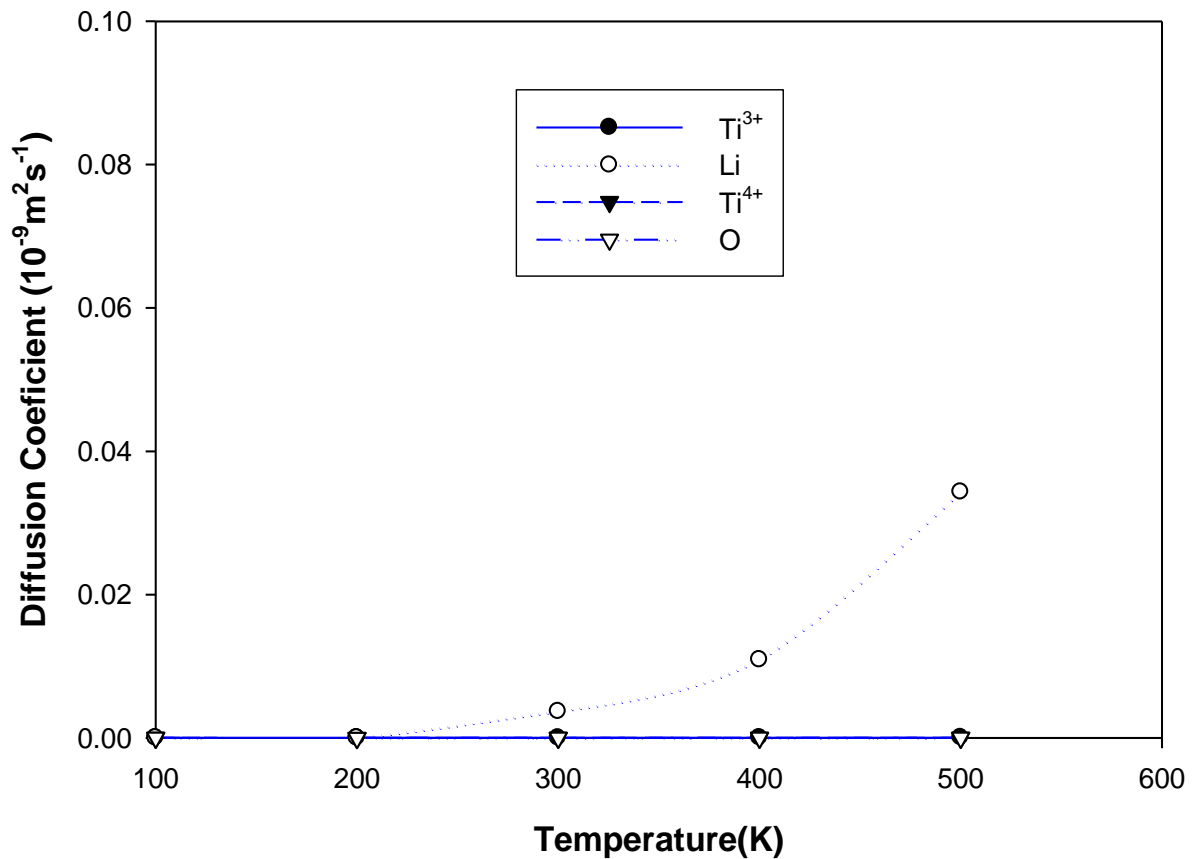


Figure 53: Variation of Ti³⁺, Li, Ti⁴⁺ and O diffusion coefficients with temperatures in the nanoporous TiO₂ with 0.03 Li ion concentration.

Insertion of 0.04 Li ion concentration into the TiO₂ nanoporous in figure 54 shows similar behaviour, however, at high rate diffusion coefficients. A stable structure throughout the applied temperatures, as that in figure 53 but with more Li ions filling all the vacancies, is anticipated. This assumption is really supported by the microstructure in figure 45 (b). There is no change in diffusion rate here in Figure 55 depicting diffusion coefficients of TiO₂ nanoporous with 0.07 Li ions at increased temperatures. However, the 0.07 Li ion concentrations have required more than 300 K to initiate diffusion.

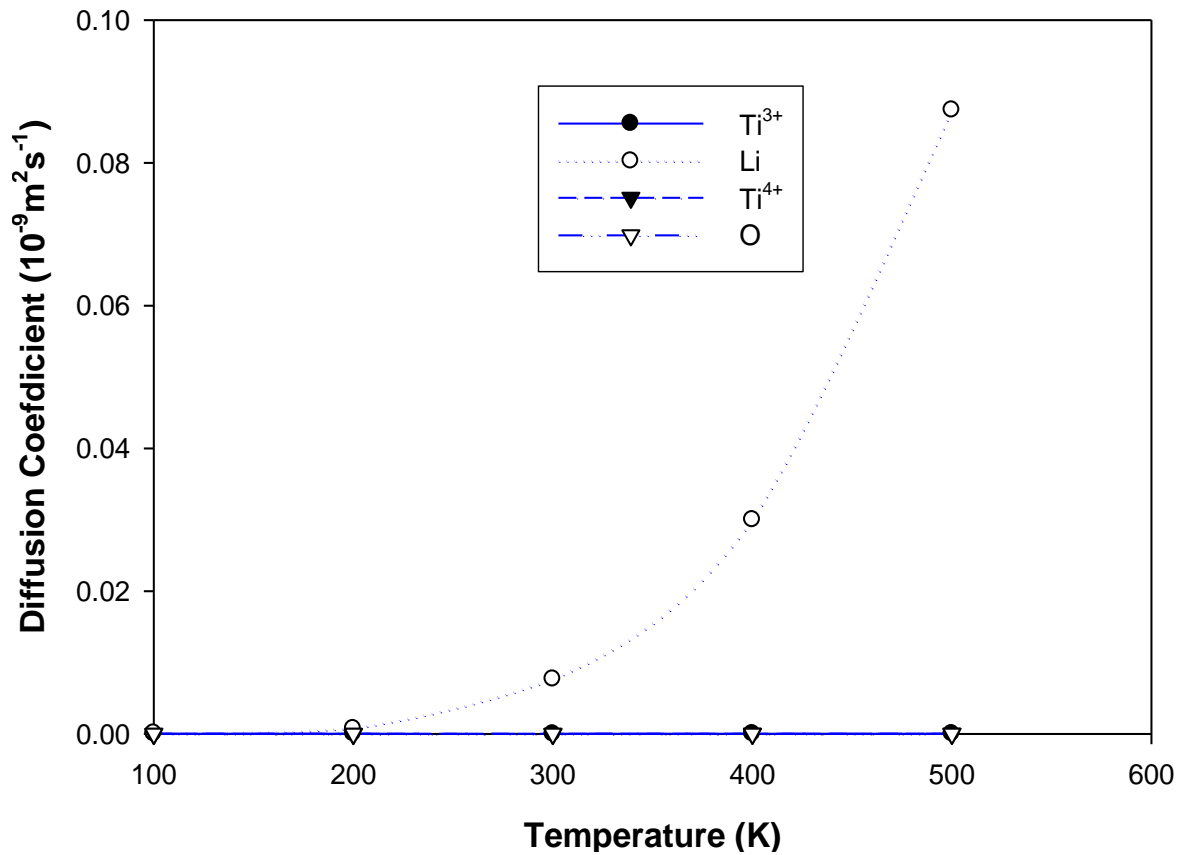


Figure 54: Variation of Ti³⁺, Li, Ti⁴⁺ and O diffusion coefficients with temperatures in the nanoporous TiO₂ with 0.04 Li ion concentrations.

Figure 56 depicts diffusion coefficients in a bulk Li_{0.03}TiO₂ that reflects a near sinusoidal curve as the temperature is raised, having a maxima occurring at 300 and 500 K for Li atoms including Ti³⁺ ions at 400 K. It should be noted that, unlike other nanostructures, the diffusion coefficients of Li the bulk is in exponential form, which is very small. Diffusion of other bulk TiO₂ atoms were hardly noticeable from 100 up to 300 K, however, with slight increase beyond 300 K. This behaviour illustrates that the all ions arrangements were altered between 0 and 500 K in concurrence with a trend seen in figure 46 (a).

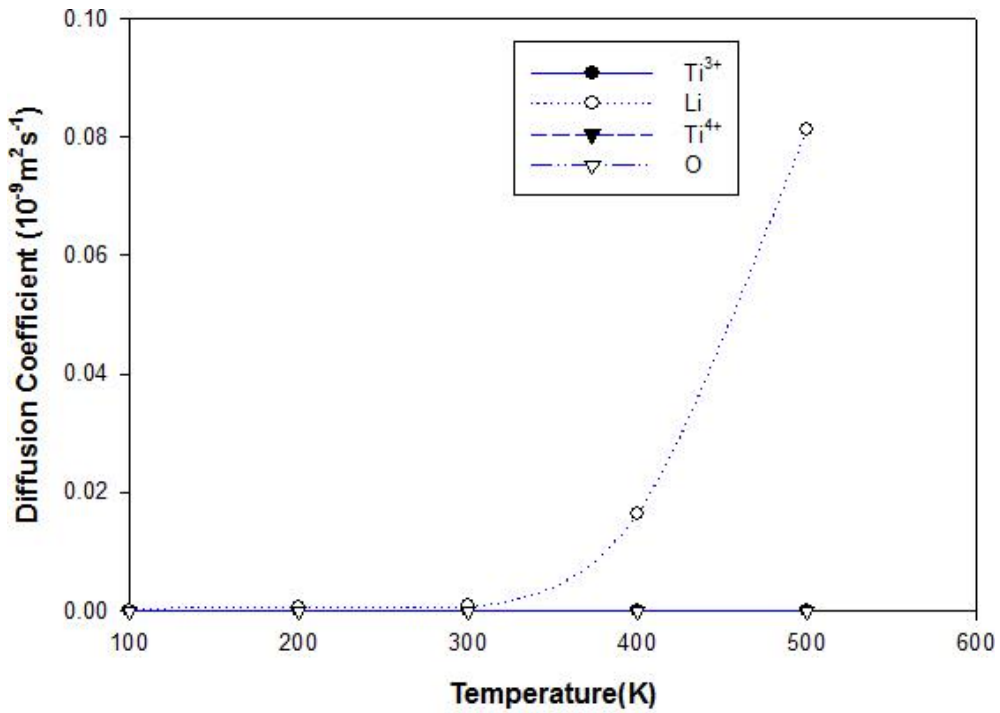


Figure 55: Variation of Ti³⁺, Li, Ti⁴⁺ and O diffusion coefficients with temperatures in the nanoporous TiO₂ with 0.07 Li ion concentrations.

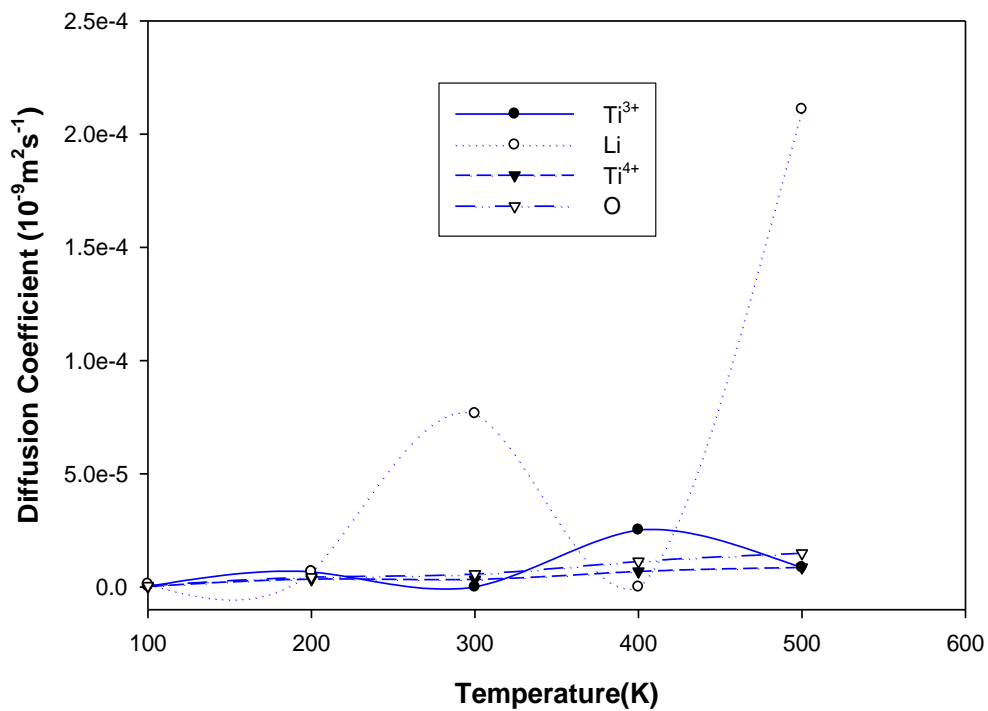


Figure 56: Variation of Ti³⁺, Li, Ti⁴⁺ and O diffusion coefficients with temperatures in the bulk TiO₂ with 0.03 Li ion concentrations.

Elevating temperature on bulk, TiO_2 with 0.04 Li ion concentrations shown in figure 57 have influenced high rate diffusion of all ions. This sinusoidal curve shows diffusion of Li atoms exactly at 100 K with maxima near 200 and 400 K and minima close to 300 K. This behaviour is influenced by the distorted patterns of ions viewed in 46 (b).

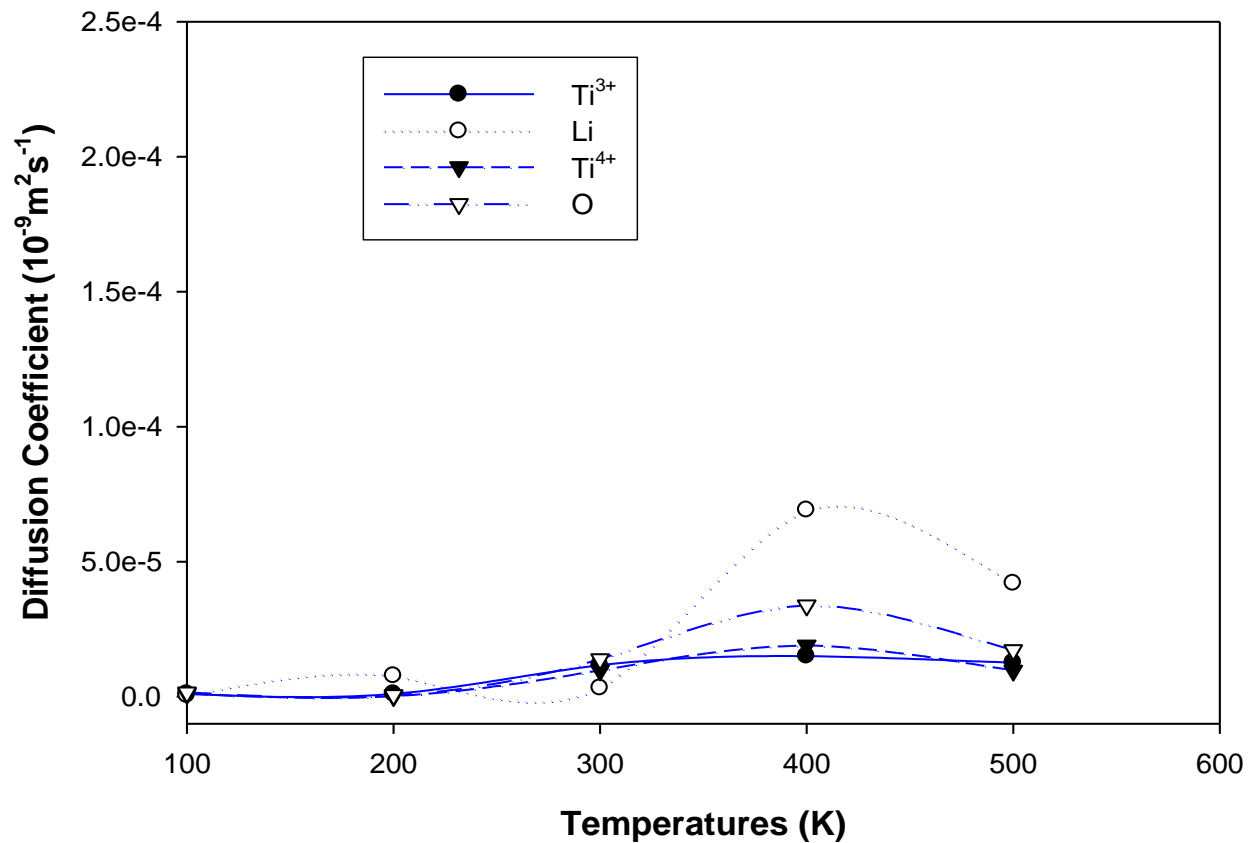


Figure 57: Variation of Ti^{3+} , Li, Ti^{4+} and O diffusion coefficients with temperatures in the bulk TiO_2 with 0.04 Li concentrations.

Figure 58 display diffusion coefficients in a bulk $\text{Li}_{0.07}\text{TiO}_2$ at elevated temperatures. A negative diffusion of Li atoms is detected between 100 and 200 K due to the close packed of atoms, however; beyond 200 K diffusion started increasing distinctly with an increase in temperature. Therefore, diffusion of Li atoms in TiO_2 is fully dependent on temperature and Li ion concentration.

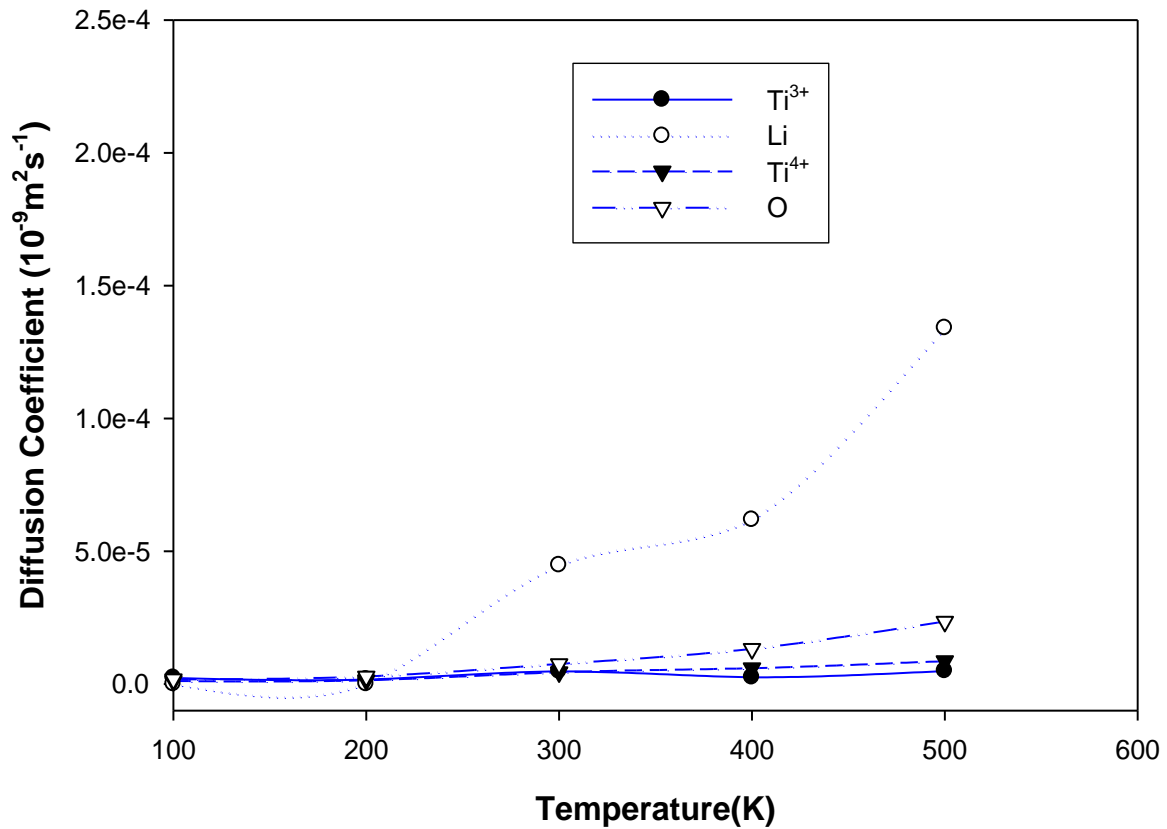


Figure 58: Variation of Ti³⁺, Li, Ti⁴⁺ and O diffusion coefficients with temperatures in the bulk TiO₂ with 0.07 Li ion concentrations.

Figure 59 shows diffusion coefficients inside the sphere, sheet, porous and bulk nano-architectures with 0.03 Li ion concentration at increased temperature. The nanosphere has the highest diffusion coefficient when compared to other nano-architectures, which however, fluctuate anomalously. Figures 60 and 61 show diffusion coefficients inside the sphere, sheet, porous and bulk nano-architectured with 0.04 and 0.07 Li ion concentrations respectively at increased temperatures. The nanosphere still have the highest diffusion rate, the three nano-architectures have a split in diffusion coefficients right above 400 K. In all concentrations, the diffusion coefficients of bulk structure are near zero.

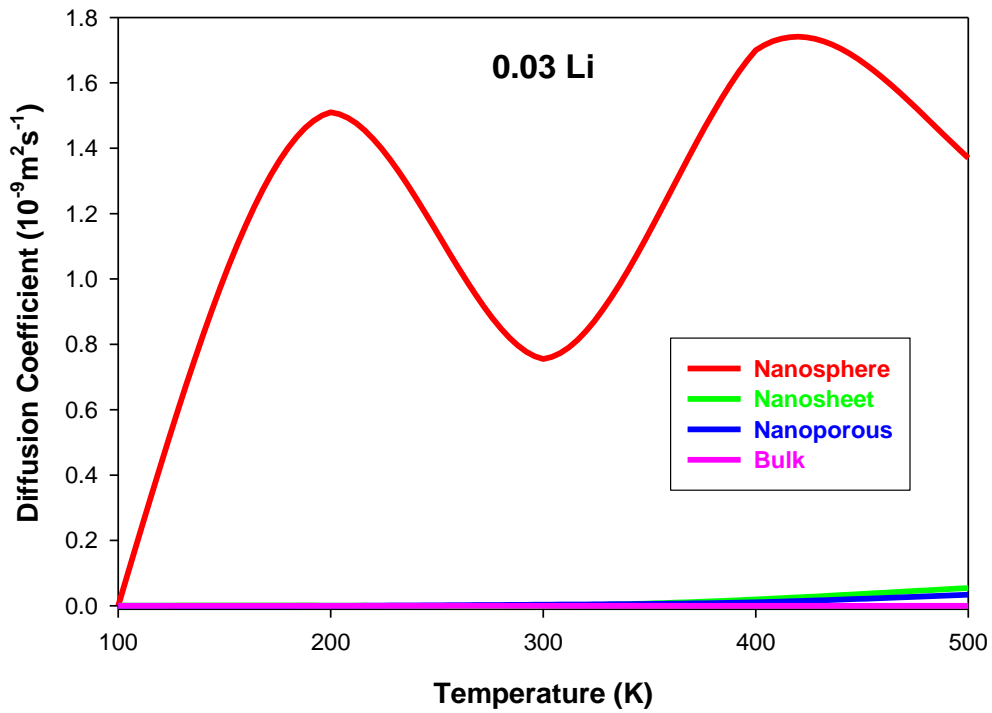


Figure 59: Variation of Li diffusion coefficient with temperature in the nanosphere, nanosheet, nanoporous and bulk TiO_2 inserted with 0.03 Li ions.

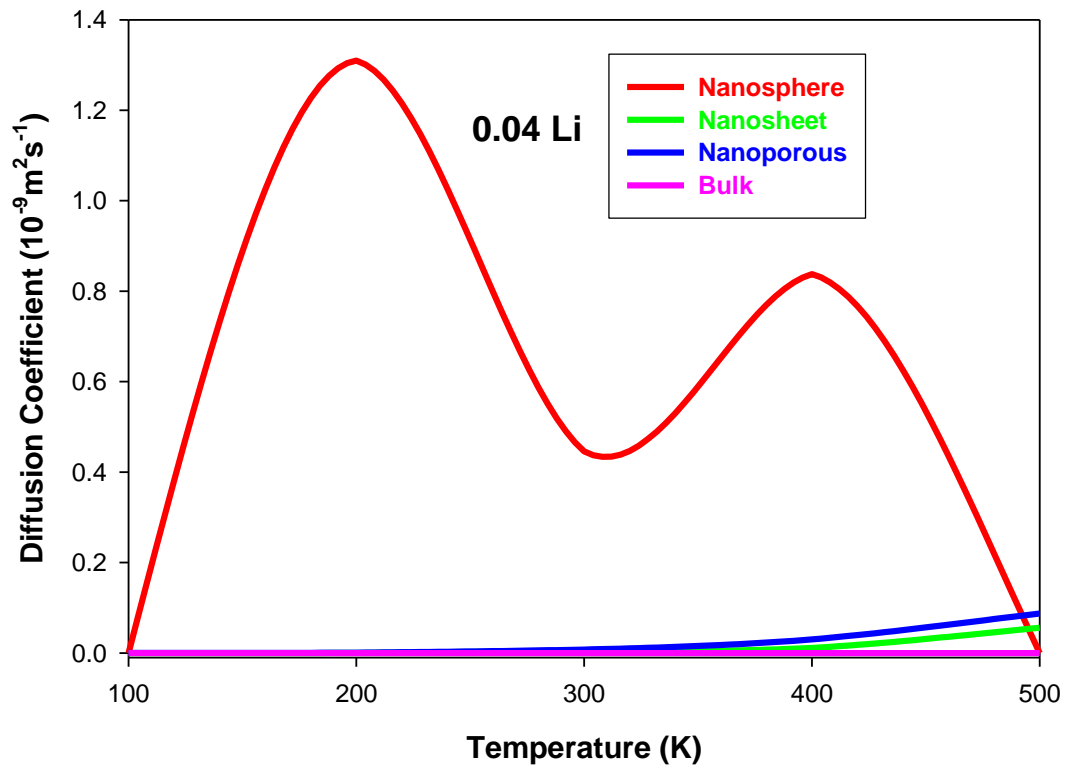


Figure 60: Variation of Li diffusion coefficient with temperature in the nanosphere, nanosheet, nanoporous and bulk TiO_2 inserted with 0.04 Li ions.

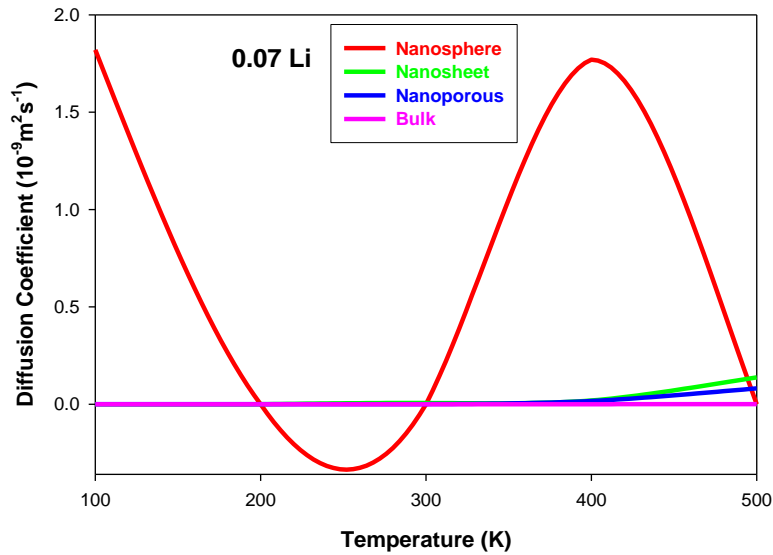


Figure 61: Variation of Li diffusion coefficients with temperatures in the nanosphere, nanosheet, nanoporous and bulk TiO₂ with 0.07 Li ion concentrations.

Figure 62 illustrates Li diffusion for 0.03, 0.04 and 0.07 Li ion concentrations within the nanosphere at increased temperature. Although the diffusion coefficients appear to be lowered when the Li concentration is increased in the nanosphere, this cannot be confirmed with certainty owing to its anomalous change with temperature.

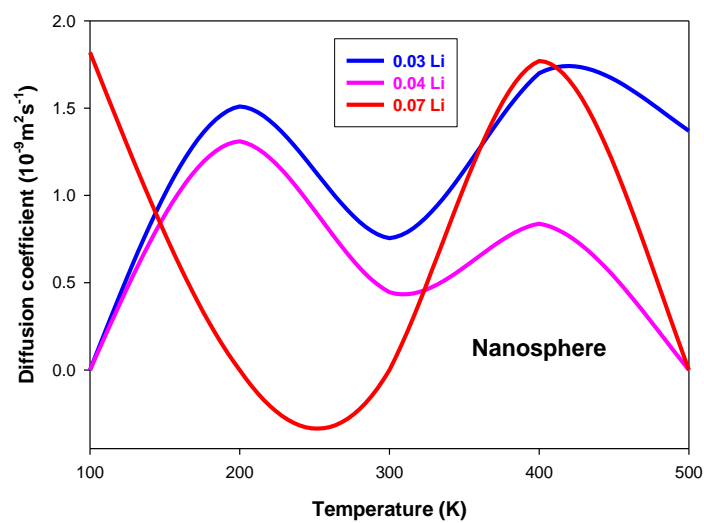


Figure 62: Variation of Li diffusion coefficients with temperatures in the nanosphere TiO₂ with 0.03, 0.04 and 0.07 lithium ion concentrations.

Figure 63 shows Li diffusion for 0.03, 0.04 and 0.07 Li ion concentrations within the nanosheet at increased temperature. An increase in diffusion coefficients with Li concentration is noted between 200 and 320 K, however beyond 320 K the diffusion coefficient have yielded an inconsistent behaviour with regard to Li concentrations. The diffusion coefficients in the nanosheet shown in figure 63 are quasi-linear suggesting diffusion between channels that are interconnected by pairs. This quasi-linear diffusion is expected to be of brookite polymorphs as seen from XRDs and microstructures figure 40 and 45 respectively.

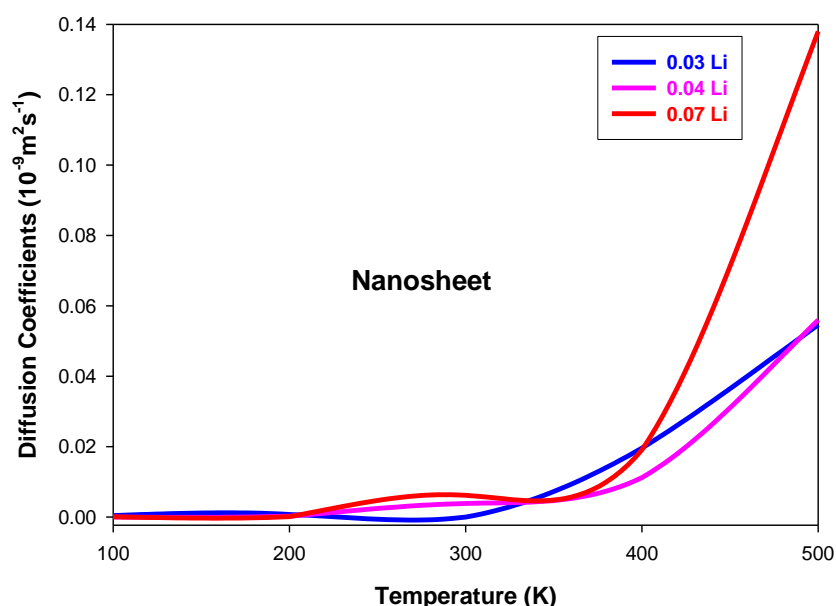


Figure 63: Variation of Li diffusion coefficients with temperatures in the nanosheet TiO_2 with 0.03, 0.04 and 0.07 lithium ion concentrations.

Figure 64 illustrates Li diffusion for 0.03, 0.04 and 0.07 Li ion concentrations within the nanoporous at increased temperature. Higher Li concentrations give high diffusion coefficient while low Li atoms gives low diffusion coefficient in the nanoporous architecture beyond 400 K. The smooth linear diffusion coefficients for nanoporous in figure 64 indicates a dominant of a rutile phase that is also evident on the XRDs and microstructures figure 40 and 45 respectively.

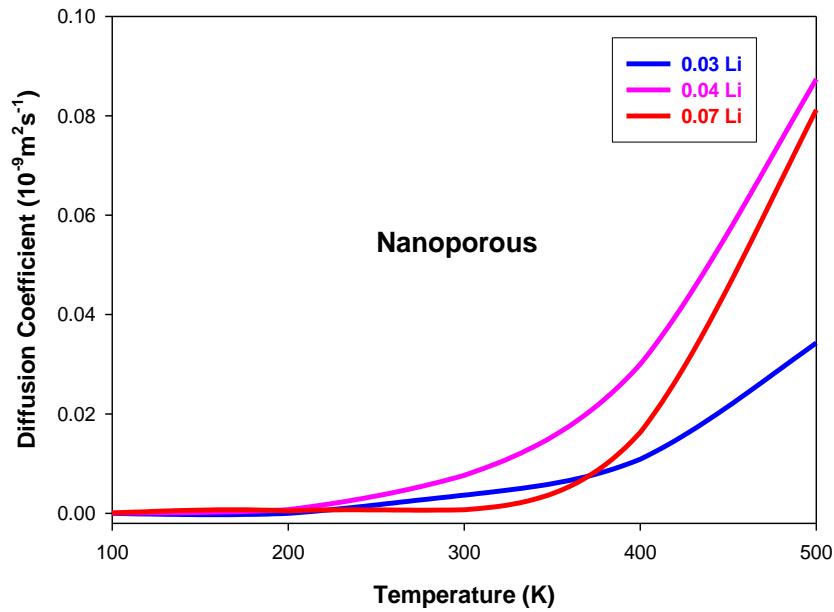
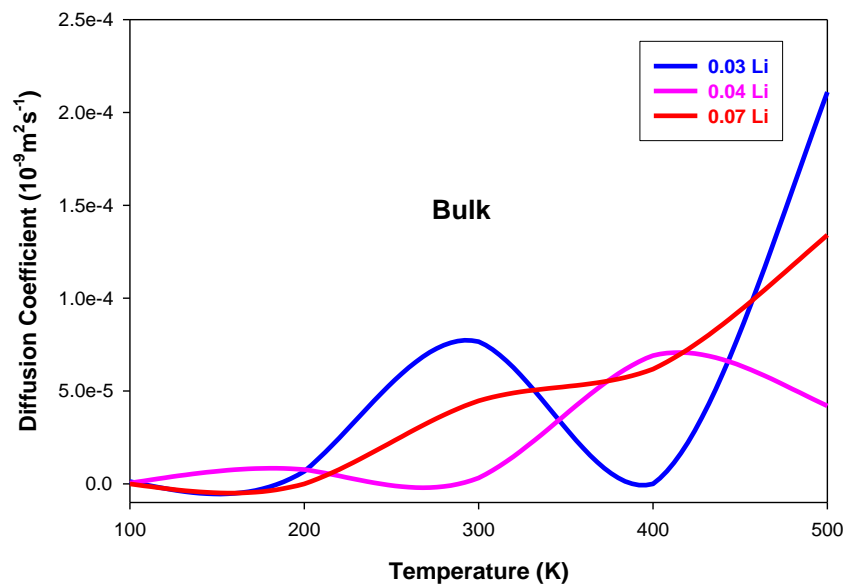


Figure 64: Variation of Li diffusion coefficients with temperatures in the nanoporous TiO₂ with 0.03, 0.04 and 0.07 lithium ion concentrations.

Figure 65 illustrates Li diffusion for 0.03, 0.04 and 0.07 Li ion concentrations within the bulk at increased temperatures. In the bulk structure, negligible Li diffusion is noted at



increased temperatures.

Figure 65: Variation of Li diffusion coefficients with temperatures in the bulk TiO₂ with 0.03, 0.04 and 0.07 lithium ion concentrations.

3.2 Discussions

Various nano-architected structures of lithium TiO_2 and their properties have been studied extensively due to their potential use in the Li-ion battery applications. In these study four nano-architectures, namely nanosphere, nanosheet, nanoporous and bulk were inserted with 0.03, 0.04 and 0.07 Li ion concentrations. The Li^+ ions settled in a TiO_2 crystal lattice, forming a Li_xTiO_2 , with composite brookite and rutile polymorphs. The goal was to insert as many lithium ions as possible into the nano-architectures, but their number are limited by the repulsive, coulombic interactions hence 0.03, 0.04 and 0.07 Li concentration were achieved. This amount of Li in a TiO_2 has proved that the brookite and rutile crystal structures can accommodate a maximum of Li ions greater than that of $x=0.07$ at elevated temperature using molecular dynamics techniques. It has, however, been observed that the lithiated nanosheet and nanoporous architectures were partially crystalline before crystallisation. Such partial crystallinity is confirmed by an almost constant plot of configuration energy as a function of time.

All lithiated nanostructures were successfully crystallised and cooled towards 0 K as evidenced by their configuration energy vs. time and RDFs plots. All cooled nanostructures were then heated to temperatures between 100 and 500 K at intervals of 100 K. After recrystallisation, most Li ions are located within systems, which indicates that TiO_2 nano-architectures can really host more Li ions. Li_xTiO_2 crystallises into the rutile and brookite structures, and as Ti or O species evolve from amorphous to crystalline phase, the Li ions are then pushed out of the systems. However, upon cooling, more tunnels were created and have enabled some Li ions to re-enter the structure whilst others remain on the surfaces. The retention of lithium ions in various Li_xTiO_2 nano-architectures were as follows. For the nanosphere, after recrystallisation of the 0.03 lithium ion concentration system: 0.006 lithium ion concentration moved out

and 0.024 remained within the structure; for the 0.04 lithium ions system: 0.009 lithium ion concentration moved out and 0.031 remained within the structure and with the 0.07 lithium ion concentration system: 0.015 lithium ion concentration moved out and 0.055 were retained within the structure. For the nanosheet, after recrystallisation for 0.03 lithium concentration: 0.004 lithium ion concentration moved out and 0.026 remained within the structure; for the 0.04 lithium ion concentration: 0.004 lithium ion concentration moved out and 0.036 remained in the structure; and for 0.07 the lithium ion concentration: 0.008 lithium ion concentration moved out and 0.062 remained. In case of the nanoporous structure, after recrystallisation of the 0.03 lithium ion concentration system: 0.004 lithium ion concentration moved out and 0.026 remained within the structure. As for 0.04 lithium ion concentration system: 0.004 lithium ion concentration moved out and 0.036 remained in the structure; and for 0.07 lithium ions system: 0.007 ion concentration moved out and 0.063 remained in the system. For bulk structure, all lithium ions were contained in the structure for all given concentrations. Configurational energy vs time plots for all nano-architectures of TiO_2 recrystallised with three lithium concentrations were compared, they indicate short nucleation period in the initial stage, which appears to be diminished in the latter stage, which suggest that lithiation have increased crystallisation, especially for the 0.03 Li ions system.

Moreover, when the lithium ion concentration is increased to 0.04 and 0.07, crystallisation appears to be suppressed which is evidenced by the decreased slope of the energy vs. time plots. The prolonged delay of crystallisation through lithiation is quite distinct in the bulk system than in the nanosphere system of LiTiO_2 . As seen from their plots, extended nucleation phases tend to increase with increasing Li content. Full crystallisation was achieved on the nanosheet and nanoporous that were crystalline. After recrystallizing, all nano-architectures were cooled from 1500 to 0 K, at intervals

of 500 K, and their structures were subsequently analysed using the radial distribution functions (RDF's) for $\text{Ti}^{4+} - \text{O}^{2-}$ and $\text{Ti}^{3+} - \text{O}^{2-}$ interactions. The results suggest a crystalline form in the $\text{Ti}^{3+} - \text{O}^{2-}$ interactions of nanosphere with 0.03 Li concentration and the rest were in their amorphous state on all concentrations and atom-atom pair. The nanosheet and nanoporous showed a crystalline pattern at all Li-concentrations and $\text{Ti}^{x+} - \text{O}^{2-}$ atom interactions except for nanoporous with 0.07 Li ion concentration. In the bulk system, the amorphous phase tends to be more dominant as the Li content was increased. So all crystallised nano-architectures appear to have undergone significant structural changes as temperature increases, over the timescale of the simulations.

Further structural characterization was deduced from the X-ray diffraction patterns, where calculated XRDs of simulated nanosphere, nanosheet, nanoporous and bulk TiO_2 display indexed peaks which accord well with the brookite and rutile arrangements. Superimposed XRDs of lithiated nanosphere and bulk appear to be most affected by the increase of Li concentration where peaks at higher angles especially 58 and 68° , appear to be much broader (associated with reduced crystallinity) at higher lithium concentrations. Furthermore, for nanoporous and nanosheet XRD peaks tend to shift to lower values of θ with increasing lithium content, which might be partly ascribed to an increase of the rutile phase.

Again, concerning the bulk Li_xTiO_2 the first peak at 30° associated with the brookite structure disappears at higher lithium concentrations. In addition, peaks at 58 and 68° shift to lower values and a new peak emerges on the right of the latter; all such changes suggest an increase of the rutile polymorph, in agreement with observed changes on the microstructures of the bulk TiO_2 . The layering of the Ti^{4+} and Ti^{3+} octahedron was

evident from the microstructures of Li_xTiO_2 nano-architectures when compared at 0 and 500 K. The observed microstructures reveal various patterns; twinned straight and zigzag tunnels and vacancies. Bulk TiO_2 , with 0.03 Li, shows twinned patterns that are not obvious when compared to the nanoporous and nanosheet. However, bulk TiO_2 , with 0.04 and 0.07 Li, show Li ions that are trapped in tunnels and have a melted structure. It appears high Li content shortens tunnels of Ti octahedra which seem not to accommodate more Li ions and tend to be located in the Ti vacancies. An increase in the brookite polymorph with concentration is in good agreement with calculated XRD results that suggest enhanced brookite peaks. Microstructures of the nano- sphere, sheet and porous TiO_2 architectures respond differently to Li insertion when compared to the bulk. Straight and zigzag tunnels associated with the twinned rutile and brookite polymorphs respectively were mostly observed. These patterns seemed to be retained after lithiation with i.e. from 0.03 to 0.07 Li concentrations. The Li ions are mostly contained in tunnels, as demonstrated by both upper and lower layers formed by Ti octahedral. This suggest that the tunnels of the nano-architectures are flexible enough to accommodate and transport such amounts of Li ions which further allowed more passages for fast diffusion. The bulk nano-architecture appears to be not conveniently providing such path, hence its poor performance when used in electrodes for Li-ion batteries.

Molecular dynamics simulations also allowed us to investigate the ion diffusion coefficients in Li_xTiO_2 nanostructures for ($x = 0.03, 0.04$ and 0.07) at temperatures ranging from 100 to 500 K. Although confined in tunnels, ions were observed to diffuse faster in the nanosphere, nanosheet and nanoporous architectures than in bulk structures. Such enhanced in plane ion diffusion could be attributed to reduced ion concentration/ion pairing, open crystal structures and lower melting temperatures.

Even at the same concentrations, the Li^+ ions in the nanosphere, sheet and porous presented larger diffusion coefficients than those in bulk, indicating the significant role of the temperature-concentration dependence. When increasing Li content, the ion diffusion was strongly affected by coulombic forces and ion-ion correlations leading to smaller diffusion coefficients mainly on bulk systems compared with those in nanosphere, sheet and porous architectures. Ions enter channels then exhibit small diffusion coefficients. Generally the diffusion coefficients of Li^+ in channels decreased with a decreased in channel width this is all evident on microstructures in section 3.1.6. An increase in temperature on all nanostructures has led to high-enhanced vibrant thermal motion of ions. Comparing microstructures at 0 and 500 K for all nanostructures, Li^+ ion diffusion in channels are more sensitive to temperature.

Chapter 4

4 Conclusions and Recommendations

4.1 Conclusions

Simulated amorphisation recrystallization method, based on classical molecular dynamics using Buckingham potentials, was successfully employed to generate different TiO₂ nano-architectures with different lithium concentrations. In particular, calculations were carried out on TiO₂ nanosphere, nanosheet, nanoporous and bulk architectures at various lithium concentrations and temperatures and configurational energy time plots, structures, XRDs, RDFs, microstructures and diffusion of lithium ions were determined.

All nano-architectures of Li_xTiO₂ were successfully crystallised, at elevated temperatures under the NVT ensemble, as deduced from the variation of configuration energies with time, final structures and microstructures. However, those of the nanosheet and nanoporous structures were partially crystallised during their formation, when the supercell lattice box was reduced under the NPT ensemble. The crystallised structures were subsequently annealed to 0K. An analysis of the XRD patterns of the nano-architectures depicts the presence of two TiO₂ polymorphs i.e. the rutile and brookite phases. The composite TiO₂ is further confirmed by simulated microstructures of Li_xTiO₂ which show straight and zigzag tunnels corresponding to the rutile and brookite polymorphs respectively. Such tunnels are more explicit in the nanoporous and nanosheet structures but are not always evident in the bulk structures. Composite structures with multiple polymorphs have been reported experimentally for TiO₂.

Another interesting aspect of the study is the impact of lithiation on crystallisation of Li_xTiO₂. From the variation of the configuration energy with time, it is evident that the

nucleation process, occurring in the amorphous phase, is extended with an increase of lithium content. Such behaviour was also reported from previous X-ray studies [56] where it was shown that TiO_2 brookite framework tends to amorphise on lithiation. This was ascribed to the flexibility of the structure, since the connectivity of the framework remains in tact.

A further unique feature of the study was to systematically investigate recrystallised nano-architectures from zero to 500 K. Structural insights were gained at an atomistic scale that explain Li ion transport mechanisms at elevated temperatures. It was noted that the Li diffusion coefficient, for all Li concentrations, increases with temperature particularly in the nanoporous and nanosheet structures. The corresponding XRDs and microstructures suggest the presence of rutile and brookite type tunnels at all Li concentrations and temperatures. In nanospheres, anomalous variation of diffusion with temperature, which is sinusoidal in shape, is noted and could be related to structural changes and re-arrangements. XRDs indicate defined structures at lower Li content for all temperatures and an absence of structures at higher Li concentration for all temperatures. Related microstructures depict rutile and brookite type tunnels at 0.03 and 0.05 Li concentrations and the absence of tunnels at higher concentrations for all temperatures. For the bulk structure, Li diffusion coefficients at all concentrations and temperatures are insignificant compared to other nano-architectures. This is consistent with the scenario shown by microstructures, where clear tunnels and pathways for the Li transport are not too apparent, particularly at higher Li concentrations.

Insights into transport mechanism in microstructures of nanostructures, supported by XRDs, could be valuable and instructive in developing strategies for optimizing anode materials for Li_xTiO_2 with good performance over a wide range of temperatures.

4.2 Recommendations

It is recommended that studies of Li concentrations higher than 0.07 in TiO_2 be attempted and a better understanding of conditions that inhibit crystallisation at such concentration be established. It will also be valuable to increase the temperature beyond 500 K since this will provide better insights of Li transport during charging and discharging at elevated temperatures. Diffusion coefficients at such temperatures will enable calculations of migration activation energies which can depict rate capabilities.

Prediction of lithium transport in various nano-architectures of Li_xTiO_2 have been made it will be important to explore such studies experimentally.

References.

- [1] J. Li. C. Daniel and D. Wood., 2011, Materials Processing for Lithium-ion Batteries., *J. Power Sources.*, **5**, 2452 - 2460.
- [2] D. Lindel and T. B. Reddy., 2009, Handbook of Batteries in Third Edition., N.Y., McGraw Hill, Inc., 315 - 353.
- [3] D. Howell, T. Duong, J. B. Deppe, and I. Weinstock., 2008, U.S. Department of Energy's Materials Research for Advanced Lithium Ion Batteries., *Mater. Mat.*, **3.4**, 100 -109.
- [4] G. Zheng, S.W. Lee, Z. Liang, H.W. Lee, K. Yan, H. Yao, H. Wang, W. Li, S. Chu, and Y. Cui., 2014, Interconnected Hollow Carbon Nanospheres for Stable Lithium Metal Anodes., *Nat Nano.*, **9**, 618 - 623.
- [5] D. Howell, T. Duong, J. B. Deppe, Irwin Weinstock, D. Linden and T. B. Reddy., 2008, Research for Advanced Lithium Ion Batteries., *Mater. Mat.*, **100**, 3 - 4.
- [6] D. H. C. Wong, J. L. Thelen, Y. Fu. D. Devaux, A. A. Pandya, V. S. Battaglia, N. P. Balsara, and J.M. DeSimone., 2014, Nonflammable Perfluoropolyether-Based Electrolytes for Lithium Batteries., *Proc. Nation. Acad. Sci.*, **9**, 3327 - 3331.
- [7] Y. Tang, Y. Zhang, J. Deng, J. Wei, H.L. Tam, B.K. Chandran, Z. Dong, Z. Chen, and X. Chen., 2014, Nanotubes: Mechanical Force-Driven Growth of Elongated Bending TiO₂-based Nanotubular Materials for Ultrafast Rechargeable Lithium Ion Batteries., *Adv.Mat.*, **35**, 6046 - 6046.
- [8] D. A. H. Hanaor, and C. C. Sorrell., 2011, Review of Anatase to Rutile Phase Transformation, *J. Mater. Sci.*, **46**, 855 - 874.
- [9] K. Amine, Z. H. Chen, Z. Zhang, J. Liu, W. Q. Lu, Y. Qin, J. Lu, L. Curtis and Y. K. Sun., 2011, New Class of Nonaqueous Electrolytes for Long-Life and Safe Lithium-Ion Batteries., *J. Mater. Chem*, **21**, 17754 -17759.
- [10] J.M. Tarascon and M. Armand., 2001, Issues and Challenges Facing Rechargeable Lithium Batteries., *Nat.*, **414**, 359 - 368.
- [11] B.J. Landi, M. J. Ganter, C.D. Cress, R.A. Dileo and R.P. Raffaele., 2009, Carbon Nanotubes for Lithium Ion Batteries, *Energy Environ. Sci.*, **2**, 638 - 654.

- [12] Z. H. Chen, I. Belharouak, K. Amine and Dr. Y. K. Sun., 2013, Highly Crystalline Lithium Titanium Oxide Sheets Coated with Nitrogen-Doped Carbon Enable High-Rate Lithium-Ion Batteries., *Adv. Funct. Mater.*, **23**, 959 - 969.
- [13] B. Rogers, J. Adams, and S. Pennathu., 2013, The Whole Story, Boca Raton: Taylor and francis., *Nanotechnology.*, 6 - 7.
- [14] J.N. Tiwari, R.N. Tiwari and K.S. Kim., 2012, Zero-Dimensional, One-Dimensional, Two-Dimensional and Three-Dimensional Nanostrured Materials for Advanced Electrochemical Energy Devices., *Prog. Mat. Sci.*, **57**, 724 - 803.
- [15] G. Schmid, W. J. Parak, L. Manna, F. C. Simmel, D. Gerion and P. Alivisatos., 2005, Nanoparticles: From Theory to Application., *Wil. Weinheim.*, Chapter 2.
- [16] E.I. Goresy, A.Chen, M. Gillet, P. Dubrovinsky, L. Graup, G. A. Rajeev., 2001, A natural shock-induced dense polymorph of rutile with α -PbO₂ structure in the suevite from the Ries crater in Germany., *Earth. Planet. Sci. Lett.*, **4**, 484 - 485.
- [17] R. Marchand, L. Brohan and M. Tournoux.,1980, A New Form of Titanium Dioxide and the Potassium Octatitanate K₂Ti₈O₁₇., *Mat. Research Bulletin.*, **15**, 1129 - 1133.
- [18] M. Lacroche, L. Brohan, R. Marchand, and R. Tournoux.,1989, New Hollandite Oxides: TiO₂(H) and K_{0.06}TiO₂., *J. of Solid State Chem.*, **81**, 78 - 82.
- [19] J. Akimoto, Y. Gotoh, Y. Oosawa, N. Nonose, T. Kumagai, K. Aoki and H. Takei., 1994, Topotactic Oxidation of Ramsdellite-Type Li_{0.5}TiO₂, a New Polymorph of Titanium Dioxide: TiO₂(R)., *J. Solid State Chem.*, **13**, 27 - 36.
- [20] P. Y. Simons and F. Dachele., 1967, The Structure of TiO₂(II), a High-Pressure Phase of TiO₂., *Acta Crystallogr., Sect. B: Struct. Sci.*, **23**, 334 - 336.
- [21] H. Sato, S. Endo, M. Sugiyama, T. Kikegawa, O. Shimomura and K. Kusaba., 1991, Baddeleyite-Type High-Pressure Phase of TiO₂., *Sci.*, **251**, 786 - 788.
- [22] N.A. Dubrovinskaia, L.S. Dubrovinsky, R. Ahuja, V.B. Prokopenko, V. Dmitriev, H.P. Weber, J.M. Osorio-Guillen and B. Johansson., 2001, Experimental and Theoretical Identification of a New High-Pressure TiO₂ Polymorph., *Phys. Rev. Lett.*, **87**, 275501 - 275501.
- [23] M. Mattesini, J.S. de Almeida, L. Dubrovinsky, L. Dubrovinskaia. B. Johansson and R. Ahuja., 2004, High-Pressure and High-Temperature Synthesis of the Cubic TiO₂ polymorph., *Phys. Rev. B.*, **70**, 212101 - 212102.

- [24] L.S. Dubrovinsky, N.A. Dubrovinskaia, V. Swamy, J. Muscat, N.M. Harrison, R. Ahuja, B. Holm and B. Johansson., 2001, Materials Science: The hardest known oxide., *Nat.*, , vol. 410, **6829**, 653 - 654.,
- [25] A.R. Oganov and A.O. Lyakhov., 2010, Towards the Theory of Hardness of Materials., *J. Superhard. Mat.*, **32**, 143 - 147.
- [26] D. Nishio-Hamane, A. Shimizu, R. Nakahira, K. Niwa, A. Sano-Furukawa, T. Okada, T. Yagi and T. Kikegawa., 2010, The stability and Equation of State for the Cotunnite Phase of TiO₂ up to 70 GPa., *Phys. Chem. Miner.*, **37**, 129 - 136.
- [27] E. John., 2001, Nature's Building Blocks: An A–Z Guide to the Elements., *Oxford: Oxford University Press.*, 451 - 53.
- [28] E.I. Goresy, A.Chen, M. Gillet, P. Dubrovinsky, L. Graup and G. A. Rajeev., 2001, A natural shock-induced dense polymorph of rutile with α -PbO₂ structure in the suevite from the Ries crater in Germany., *Earth. Planet. Sci. Lett.*, **4**, 484 - 485.
- [29] N.N. Greenwood, A. Earnshaw., 1984, Chemistry of the Elements., Oxford: Pergamon Press., 1117-19.
- [30] J.F. Banfield, D.R. Veblen and D.J. Smith.,1991,The Identification of Naturally Occurring TiO₂ (B) by Structure Determination Using High-Resolution Electron Microscopy, Image Simulation and Distance–Least–Squares Refinement., *Am. Mineral.*,**76**, 342 - 343.
- [31] A. Kohno, T. Gondo, K. Kogi and T.Tajiri., Structural and Optical Characterization of TiO₂ nanoparticles-containing mesoporous Silica (SBA-15) thin films. *Mat. Scie. Eng.* **24**.
- [32] B. Liu, D. Deng, J. Y. Lee. and E. S. Aydil., 2010, Oriented Single-crystalline TiO₂ nanowires on titanium foil for lithium ion batteries., *J. Mater. Res.*, **25**, 1588 – 1594.
- [33] H. Liu, Z. Bi , X-G. Sun, R. R. Unocic, M. P. Paranthaman, S. Dai and G. M. Brown.,2011,Mesoporous TiO₂-B Microspheres with Superior Rate Performance for Lithium Ion Batteries., *Adv. Mater.*, **23**, 3450 – 3454.
- [34] S. Liu, J. Li, Q. Shen, Y. Cao, X. Guo, G. Zhang, C. Feng, J. Zhang, Z. Liu, M.L. Steigerwald, D. Xu and C. Nuckolls, 2009, Mirror-Image Photoswitching of Individual Single-Walled Carbon Nanotube Transistors Coated with Titanium Dioxide., *Angew Chem Int Ed*, **48**, 4759 – 4762.

- [35] B. O'Regan and M. Gratzel., 1991, A Low-Cost, High-Efficiency Solar Cell Based on Dye-Densitized Colloidal TiO₂ films. *Nature*. 353, 737 – 740.
- [36] A. Fujishima and K. Honda., 1972, Electrochemical Photolysis of Water at a Semiconductor Electrode. *Nature*. 238, 37 - 38.
- [37] X. Chen and S. Mao., 2007. Titanium Dioxide Nanomaterials: Synthesis, Properties, Modifications and Applications. *Chem. Rev.* **107**, 2891 - 2959.
- [38] Y. Zhang, Y. Tang, W. Li and X. Chen. 2016, Nanostructured TiO₂-Based Anode Materials for High-Performance Rechargeable Lithium-Ion Batteries. *Chem.Nano.Mat.* **2**, 764 – 775.
- [39] Y. Liu and Yefeng Yang, 2016, Recent progress of TiO₂-Based Anodes for Li Ion Batteries, *J Nano.* **2016**, 8123652 – 8123670.
- [40] L. Jabbour, R. Bongiovanni, D. Chaussy, C. Gerbaldi and D. Beneventi., 2013, Cellulose based Li-ion batteries: a review, *Cellulose*, **20**, 1523 - 1545.
- [41] P. Xiong, L. Peng, D. Chen, Y. Zhao, X. Wang and G. Yu, 2015, Two dimensional nanosheets based Li-ion batteries with high rate capability and flexibility. *Nano Energy*, **12**, 816 -823.
- [42] Z. Yang, D. Choi, S. Kerisit, K. M. Rosso, D. Wang, J. Zhang, G. Graff and J. Liu., 2009, Nanostructures and Lithium Electrochemical Reactivity of Lithium Titanates and Titanium Oxides: a review, *J. Power Sources*, **192**. 588 - 598.
- [43] X. Li. Y. Zhang, T. Li. Q. Zhong, H. Li and J. Huang., 2016, Graphene Nanoscrolls Encapsulated TiO₂ (B) Nanowires for Lithium Storage, *Journal. Power Sources.* **268**. 372-378.
- [44] J. Jin, S.-Z. Huang, J. Liu et al., 2014, Design of New Anode Materials Based on Hierarchical, Three Dimensional ordered Macro-Mesoporous TiO₂ for High Performance Lithium Ion Batteries, *J. Mat. Chem.*, **2**, 9699 - 9708.
- [45] R. Velma, J. Gangwar and A. K. Srivastava., 2017, Multiphase TiO₂ Nanostructures: a Review of Efficient Synthesis, Growth Mechanism, Probing Capabilities and Applications in Bio-Safety and Health, *RSC.*, **7**. 44199-44224.
- [46] D. Ma, Z. Cao, and A. Hu., 2014, Si-based Anode Materials for Li-ion Batteries: a Mini Review, *Nano-Micro Letters*, **6**, 347–358.
- [47] Y.Y. Bai, D. Yan, C. Yu, L. Cao, C. Wang, J. Zhang H. Zhu, Y.S. Hud, S. Dair, J. Lu and W. Zhanga., 2016, Core-Shell Si@TiO₂ nanosphere anode by atomic layer deposition for Li-ion batteries., *J. Power Sources.*, **308**, 75 - 82.
- [48] J.M. Wu, T.W. Zhang, Y.W. Zeng, S. Hayakawa, K. Tsuru and A. Osaka., 2005, Large-Scale Preparation of Ordered Titania Nanorods with Enhanced Photocatalytic Activity., *Langmuir.*, **21**, 6995 – 7002.

- [49] Y.H Wu, M.C Long, W. M Cai, S.D Dai, C. Chen, D.Y Wu, J. Bai., 2009, Preparation of Photocatalytic Anatase Nanowire Films by in Situ Oxidation of Titanium Plate. *Nanotechnology.*, **20**, 185703 - 185708.
- [50] G.L. Li, G. H. Wang and J. M. Hong, 1999, Synthesis and Characterization of Rutile TiO₂ nanowhiskers, *J. Mat. Research.* **14**, 3346 - 3354.
- [51] H. Ming, Z. Ma, H. Huang, S. Lian, H. Li, X. He, H. Yu, K. Pan, Y. Liu and Z. Kang, 2011, Nanoporous TiO₂ Spheres with Narrow Pore Size Distribution and Improved Visible Light Photocatalytic Abilities., *Chem. Commun.*, **47**, 8025 – 8027.
- [52] J. Yu, J. Fan and K. Lv, 2010, Anatase TiO₂ Nanosheets with Exposed (001) Facets: Improved Photoelectric Conversion Efficiency in Dye-Sensitized Solar Cells., *Nanoscale.* **2**, 2144 - 2149.
- [53] M. Gotić, M. Ivanda, A. Sekulića, S. Musić, S. Popović, A. Turković, K. Furić, 1996, Microstructure of Nanosized TiO₂ Obtained by Sol-Gel Synthesis., *Mat. Lett.* **28**, 225 - 229.
- [54] M. A. Reddy, M. S. Kishore, V. Pralong, V. Caignaert, U. V Varadaraju and B. Raveu., 2006, Room Temperature Synthesis and Li insertion into Nanocrystalline Rutile TiO₂., *Electrochem. Commun.* **8**, 1299 - 1303.
- [55] M. A. Reddy, V. Pralong, U.V. Varadaraju and B. Raveau., 2008, Crystallite Size Constraints on Lithium Insertion into Brookite TiO₂. *Electrochem., Solid-State Lett.*, **11**, A132 – A134.
- [56] D. Dambournet, K.W. Chapman, M. V. Koudriachova, P. J. Chupas, I. Belharouak, and K. Amine, 2011, Combining the Pair Distribution Function and Computational Methods To Understand Lithium Insertion in Brookite (TiO₂)., *Inorg. Chem.*, **50**, 5855 - 5857.
- [57] H. Fox, K. E. Newman, W. F. Schneider and S. A. Corcelli., 2010, Bulk and Surface Properties of Rutile TiO₂ from Self-Consistent-Charge Density Functional Tight Binding., *J. Chem. Theory Comput.*, **6**, 499–507.
- [58] H. S. Zhou, D. L. Li, M. Hibino and I. Honma., 2005. A self-Ordered, Crystalline-Class, Mesoporous Nanocomposite for Use as a Lithium-Based Storage Device with Both High Power and High Energy Densities., *Angew. Chem. Int. Edit.*, **44**, 797 – 802.
- [59] I. Moriguchi, R. Hidaka R, H. Yamada, T. Kudo, H. Murakami and N.Nakashima., 2006, A Mesoporous Nanocomposite of TiO₂ and Carbon nanotubes as a high-rate Li-intercalation Electrode Material., *Adv. Mater.*, **18**, 69 - 73.

- [60] H. Zhang and J. Banfield., 2000, Understanding Polymorphic Phase Transformation Behaviour During Growth of Nanocrystalline Aggregates: Insights from TiO₂., *J. Phys. Chem. B.*, **104**, 3481 – 3487.
- [61] Y. Yu, P. Zhang, L. Guo, Z. Chen, Q. Wu, Y. Ding, W. Zheng, and Y. Cao., 2014, The Design of TiO₂ Nanostructures (Nanoparticle, Nanotube, and Nanosheet) and Their Photocatalytic Activity., *J. Phys. Chem. C.*, **118**, 12727–12733.
- [62] D. C. Sayle, T. X. T. Sayle., 2007, High-Pressure Crystallisation of TiO₂ Nanocrystals., *J. Comput. Theor. Nanosci.* **4**, 299–308.
- [63] A.T. Stamps, C.E. Holland, R.E. White and E.P. Gatzke., 2005, Analysis of Capacity Fade in a Lithium Ion Battery., *J. Power Sourc.*, **150**, 229 - 239.
- [64] W. Smith and I. T. Todorov., 2006, A Short Description of DL_POLY, *Mol. Simul.*, **32**, 935 - 943.
- [65] M.M. Born and K. Huang., 1954, Dynamic Theory of Crystal Lattices., *Oxford University Press*.
- [66] H.Z. Zhang and J.F. Banfield., 2004, Aggregation, Coarsening and Phase Transformation in ZnS Nanoparticles Studied by Molecular Dynamics Simulations, *Nano Lett.*, **4**, 713 - 718.
- [67] D. Frenkel and B. Smit., 1996, Understanding Molecular Simulations from Algorithms to Applications, *San Diego: Academic Press*, 61 - 62.
- [68] W. Smith and T.R. Forester., 1996, DL_POLY_2.0: A General-Purpose Parallel Molecular Dynamics Simulation Package., *J. Molec. Graphic.*, **14**, 136 - 341.
- [69] L. Verlet., 1967, Computer Experiments on Classical Fluids. I. Thermodynamical Properties of Lennard-Jones molecules., *Phys. Rev.*, **159**, 98 - 103.
- [70] J.M. Holender., 1990, Molecular-Dynamics Studies of the Thermal Properties of the Solid and Liquid fcc Metals Ag, Au, Cu, and Ni Using Many-Body Interactions,” *Phys. Rev. B. Condens. Matt.*, **41**, 8054 - 8061.
- [71] M.P. Allen and D.J. Tildesley., 1987, Computer Simulation of Liquids., *Oxford Scientific Publishing UK.*, 66.
- [72] D.C. Sayle, J.A. Doig, S.A. Maicaneanu and G.W. Watson., 2002, The Atomistic Structure of oxide Nanoparticles Supported on an Oxide Substrate. *Phys. Rev. B. Condens. Matt.*, **65**, 245413 - 245414.

- [73] W. Kob., 1999, Computer simulations of Supercooled Liquids and Glasses., *J. Phys. Condens. Matt.*, **11**, 84 - 85.
- [74] P.M. Oliver, G.W. Watson and S.C. Parker., 1995, Molecular dynamics simulations of nickel oxide Surfaces., *Phys. Rev. B: Condens. Matt.*, **52**, 5323 - 5329.
- [75] D.C. Sayle and G.W. Watson., 2002a, Amorphisation and Recrystallisation of an MgO Cluster Supported on BaO(100)., *J. Phys. Chem. B.*, **106**, 3916 - 3925.
- [76] A. P. Sutton and R.W. Balluffi., 1987, Overview no. 61: On Geometric Criteria for Low Interfacial Energy., *Acta Metal*, **35**, 2177 – 2201.
- [77] T.X.T. Sayle, C.R.A. Catlow, D.C. Sayle, S.C. Parker and J.H. Harding., Computer Simulation of Thin Heteroepitaxial Ceramic Interfaces Using a Near-Coincidence-Site Lattice Theory., *Mag. A.*, **68**, 565 - 573.
- [78] D.C. Sayle and G. W. Watson., 2001a, Structural Exploration of Thin-Film Oxide Interfaces via Simulated Amorphisation and Recrystallisation., *Surf. Sci.*, **437**, 97 - 107.
- [79] D.C. Sayle and G.W. Watson., 2001b, The Atomistic structures of MgO/SrTiO₃(001) and BaO/SrTiO₃(001) using simulated amorphisation and recrystallisation, *J. Phys. Chem. B.*, **105**, 5506 - 5514.
- [80] D.C. Sayle and R.L. Johnston., 2003, Evolutionary Techniques in Atomistic Simulation: Thin Films and Nanoparticles., *Curr. Opin. Solid State Mater. Sci.*, **7**, 3 - 12.
- [81] D.C. Sayle, S.A. Maicaneanu and G.W. Watson., 2002c, Atomistic Models for CeO₂ (111), (110) and (100) Nanoparticles, Supported on yttrium stabilised zirconia., *J. Am. Chem. Soc.*, **124**, 11429 - 11439.
- [82] T.X.T. Sayle, C.R.A. Catlow, R.R. Maphanga, P.E. Ngoepe and D.C. Sayle., 2006, Evolving microstructure in MnO₂ using Amorphisation and recrystallisation, *J. Cryst. Growth.*, **294**, 118 - 129.
- [83] T.X.T. Sayle, S.C. Parker and D.C. Sayle, 2004, Shape of CeO₂ Nanoparticles using Simulated Amorphisation and Recrystallisation., *Chem. Commun.*, **21**, 2438 - 2439.
- [84] R.R. Maphanga, P.E. Ngoepe, T.X.T. Sayle and D.C. Sayle., 2010, Amorphisation and Recrystallisation Study of Lithium Insertion in Manganese Dioxide., *Phys. Chem. Chem. Phys.*, **13**, 1307 - 1313.

- [85] M.G. Matshaba, D.C. Sayle, T.X.T. Sayle and P.E. Ngoepe., 2016, Structure of Surface Entrance Sites for Li Intercalation Into TiO₂ Nanoparticles, Nanosheets and Mesoporous Architectures with Applications for Li ion Batteries., *J. Phys. Chem. C.*, **26**, 14001 -14008.

Appendix A

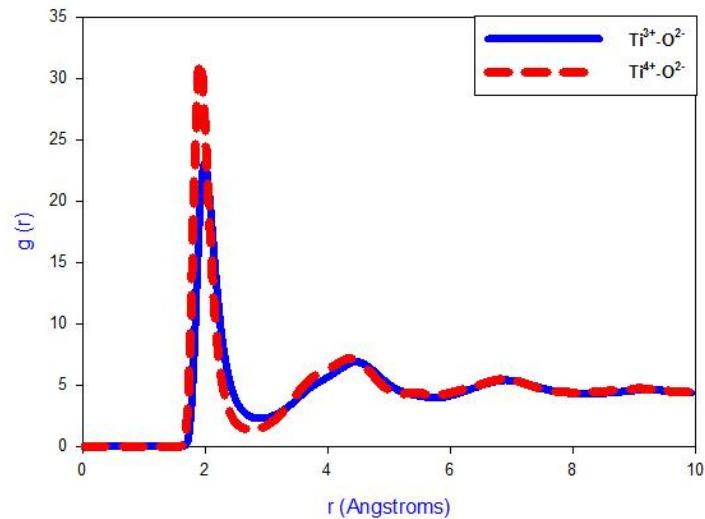
Posters and talk presented at the conferences

1. B.N. Rikhotso, M.G. Matshaba and P.E. Ngoepe, "Computational modelling studies of pure and lithiated TiO_2 nano-architected structures at different temperatures for energy storage applications", Centre for High Performance Computing Conference, 1-5 December 2014, Kruger National Park, Mpumalanga.
2. B. N. Rikhotso, M.G. Matshaba and P.E. Ngoepe, "Computational modelling studies of recrystallised nano-architected TiO_2 structures at different lithium concentration and temperatures for energy storage applications", South African Institute of Physics, 60th Annual Conference, 28 June-3 July 2015, NMMU Port Elizabeth.
3. B. N. Rikhotso, M.G. Matshaba and P.E. Ngoepe, "Atomistic Simulations studies on the structural change in Li_xTiO_2 (x: 2.82, 3.76, 6, 57) at high temperatures for energy storage in Lithium-ion Battery Applications.", South African Institute of Physics, 61st Annual Conference, 4-8 July 2016, University of Cape Town.
4. B.N. Rikhotso, M.G. Matshaba and P.E. Ngoepe, "Structural changes of Li_xTiO_2 (x: 2.82, 3.76, 6, 57) at high temperatures for energy storage in Lithium-ion Battery Applications", Centre for High Performance Computing Conference (CHPC) national meeting, 5 - 9 December 2016, East London ICC.
5. B. N. Rikhotso, M.G. Matshaba and P.E. Ngoepe, "Structural evolution and ion diffusion of $\text{Li}_{350}\text{TiO}_2$ nanosheet at different temperatures for anode material lithium ion batteries.", South African Institute of Physics, 62nd Annual Conference, 3-7 July 2017, Stellenbosch University .

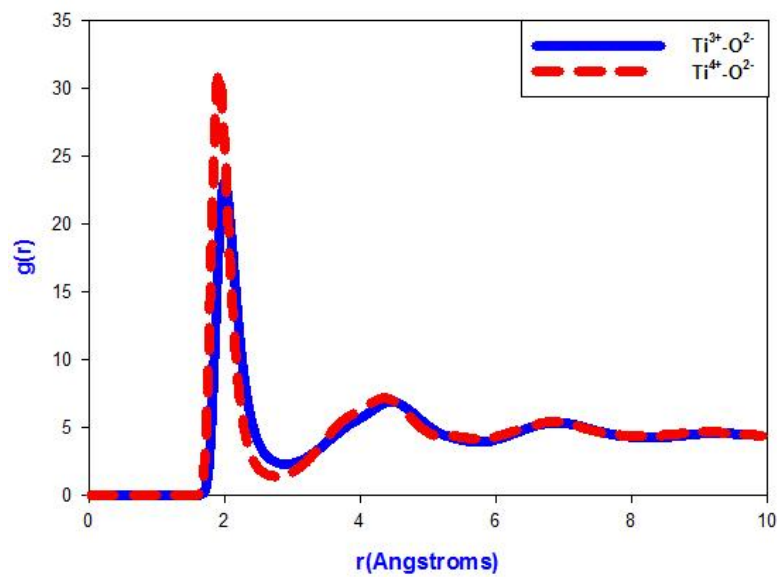
Appendix B

Radial distribution functions of lithiated nanostructures after recrystallisation and during cooling

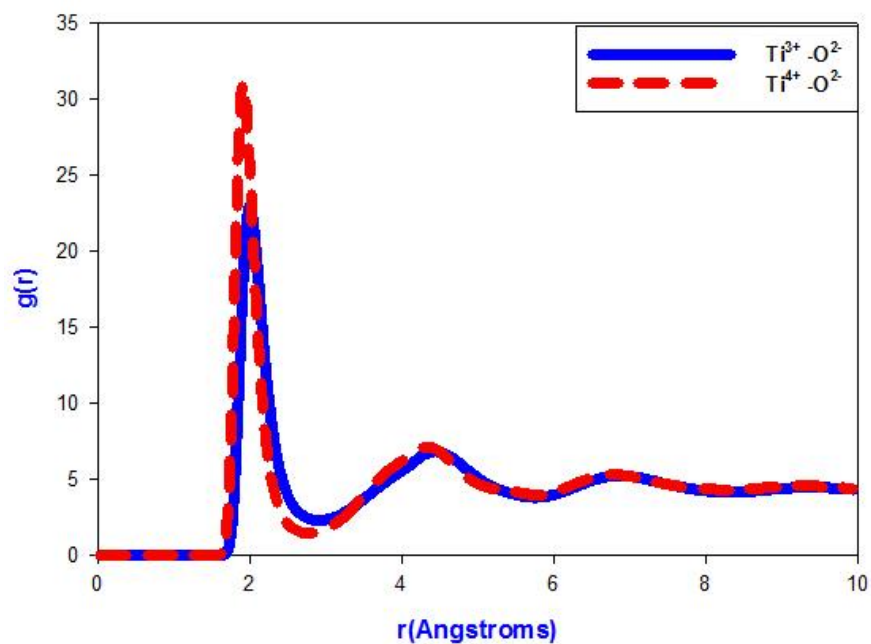
B1: RDFs of the TiO₂ nanosphere structure with 0.03 Li ions after recrystallisation at 2000 K.



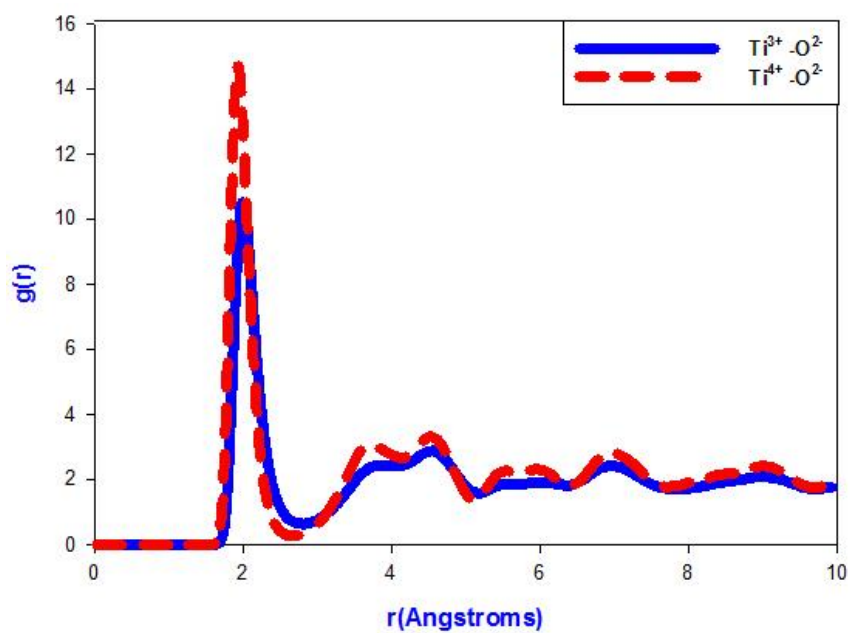
B2: RDFs of the TiO₂ nanosphere structure with 0.04 Li ions after recrystallisation at 2000 K.



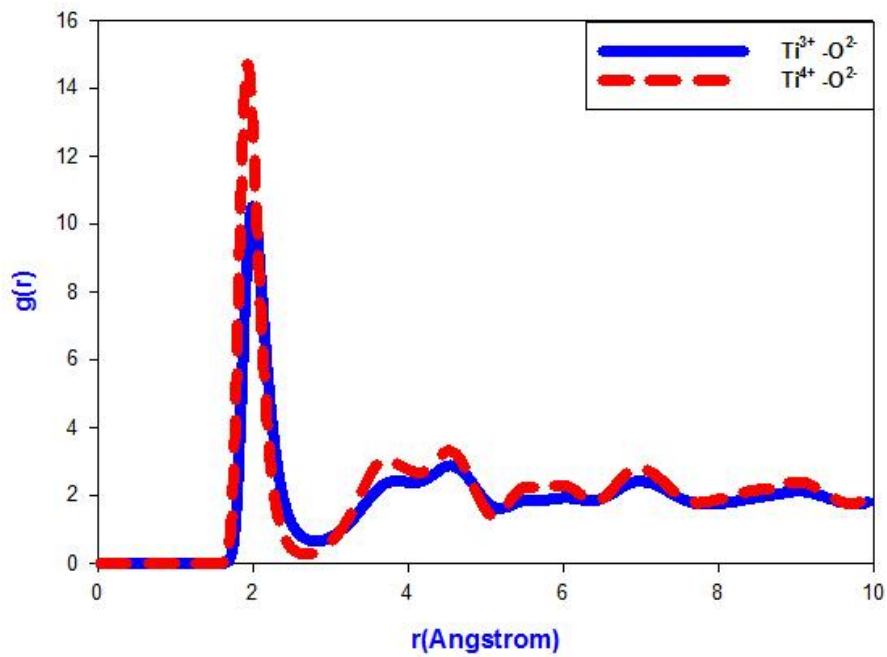
B3: RDFs of the TiO₂ nanosphere structure with 0.07 Li ions after recrystallisation at 2000 K.



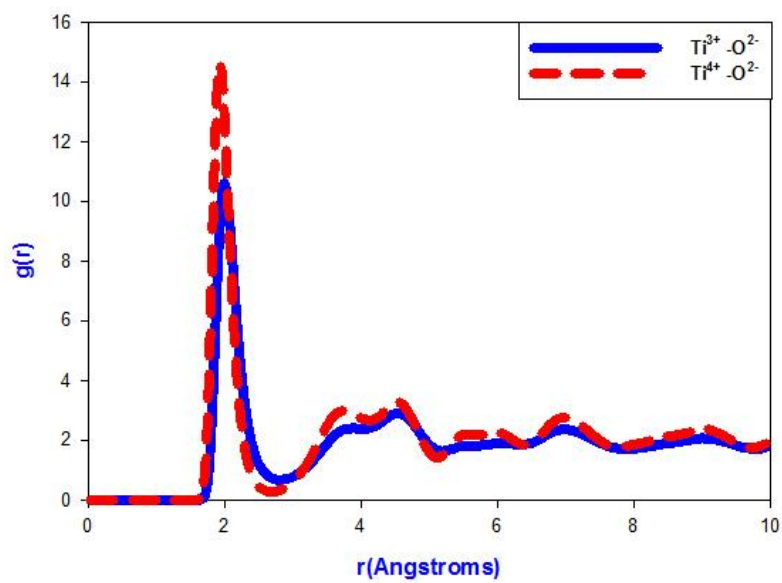
B4: Total RDFs of the nanosheet TiO₂ with 0.03 Li ions after recrystallisation at 2000 K.



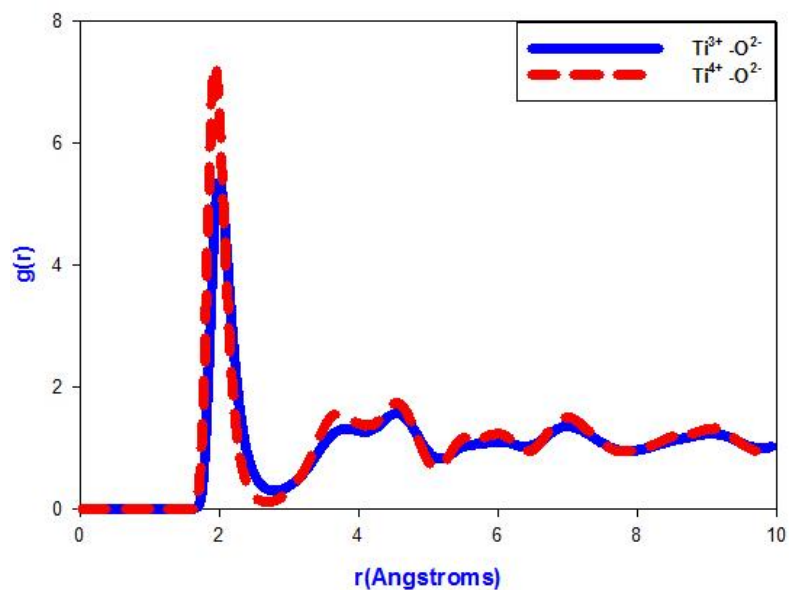
B5: Total RDFs of the nanosheet TiO₂ with 0.04 Li ions after recrystallisation at 2000 K.



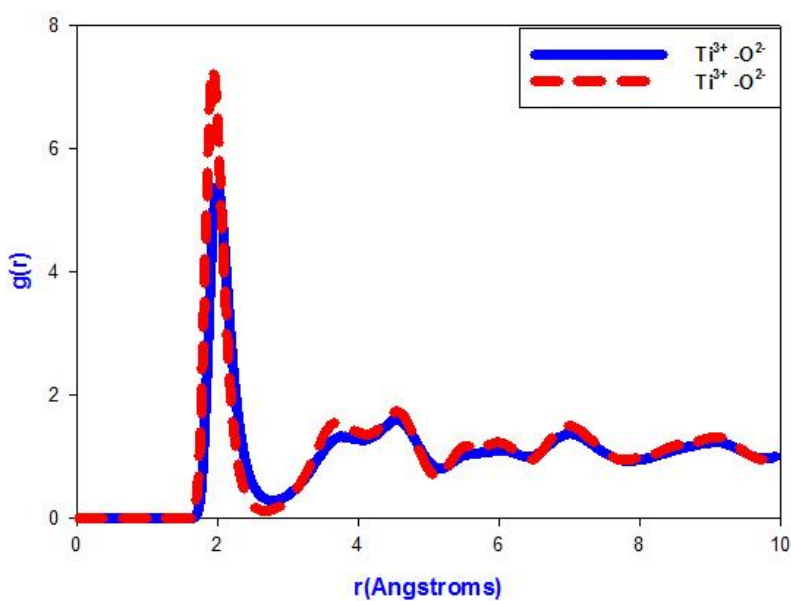
B6: Total RDFs of the nanosheet TiO_2 with 0.07 Li ions after recrystallisation at 2000 K.



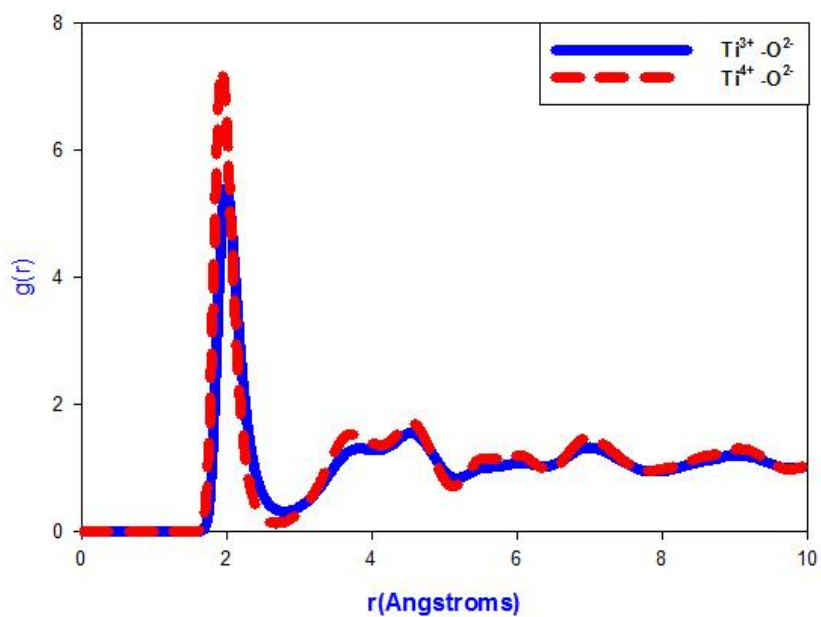
B7: Total RDFs of the nanoporous TiO_2 with 0.03 Li ions after recrystallisation at 2000 K.



B8: Total RDFs of the nanoporous TiO₂ with 0.04 Li ions after recrystallisation at 2000 K.

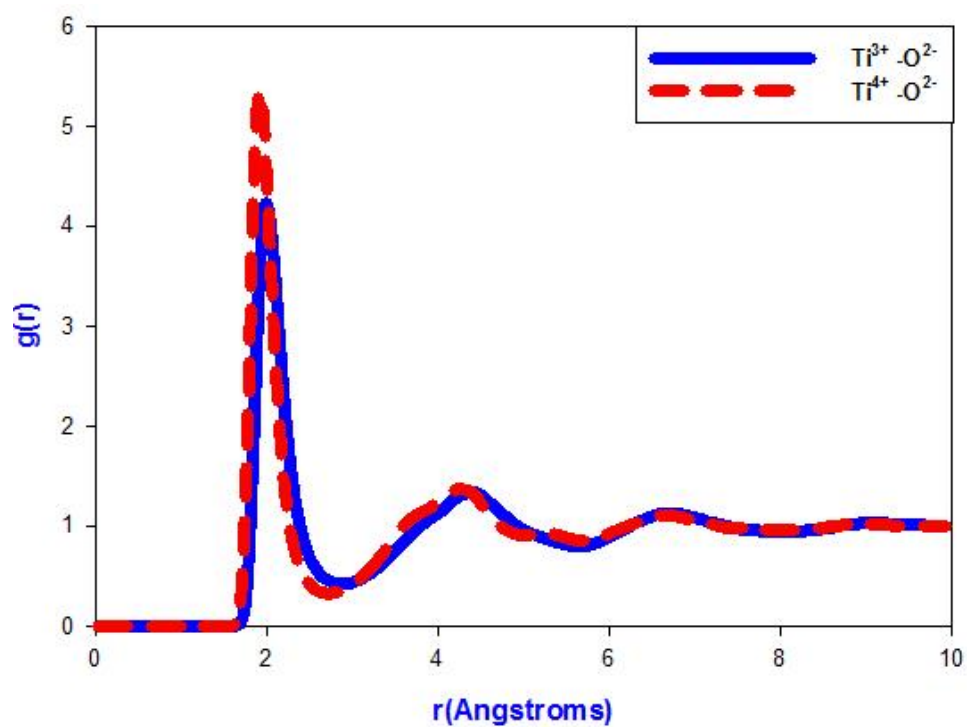


B9: Total RDFs of the nanoporous TiO₂ with 0.07 Li ions after recrystallisation at 2000 K.



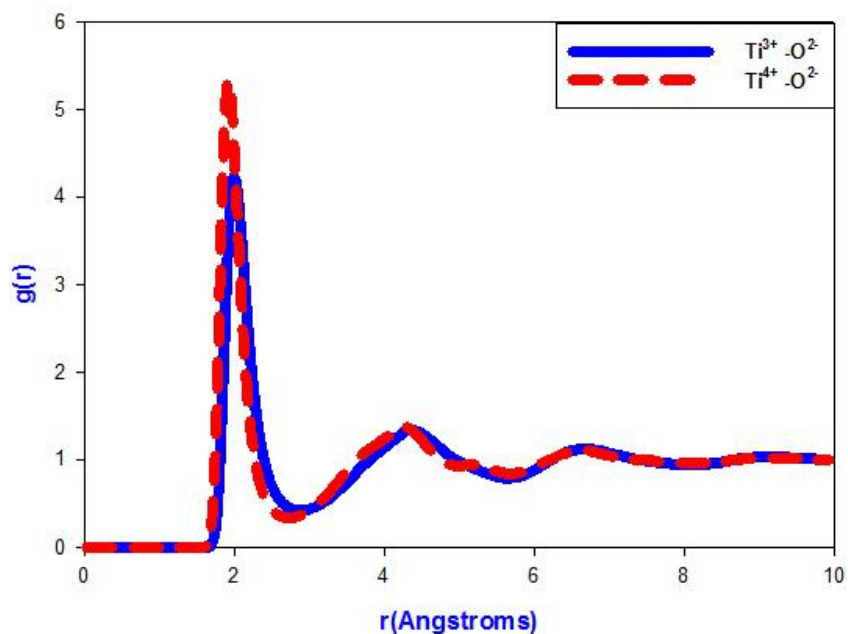
B10: Total RDFs of the bulk TiO₂ with 0.03 Li ions after recrystallisation at 2000

K.

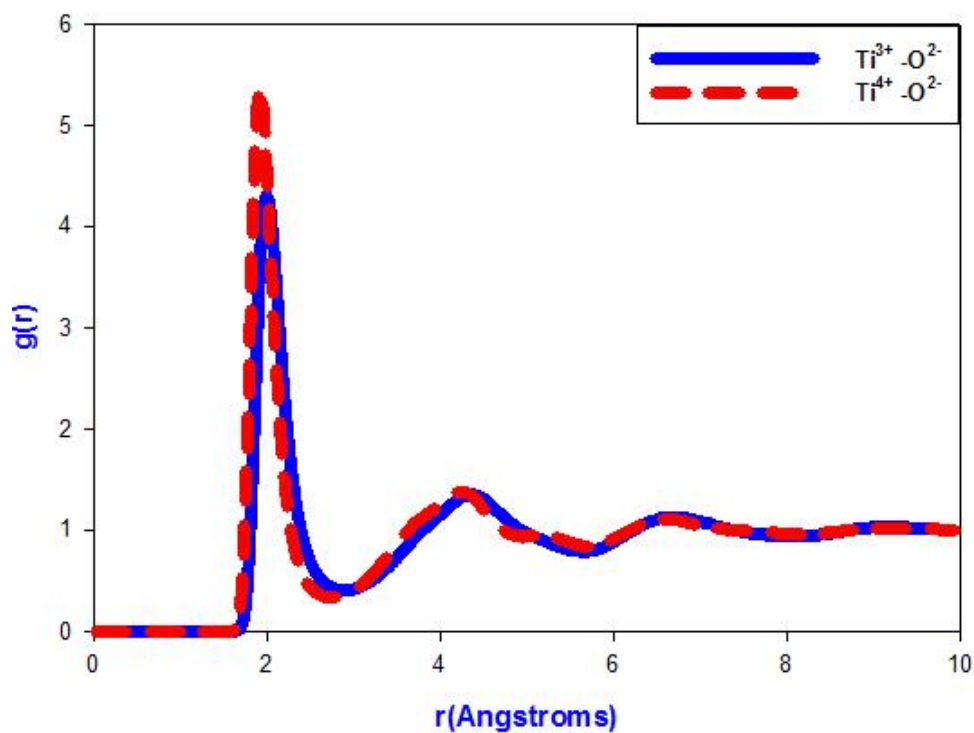


B11: Total RDFs of the bulk TiO₂ with 0.04 Li ions after recrystallisation at 2000

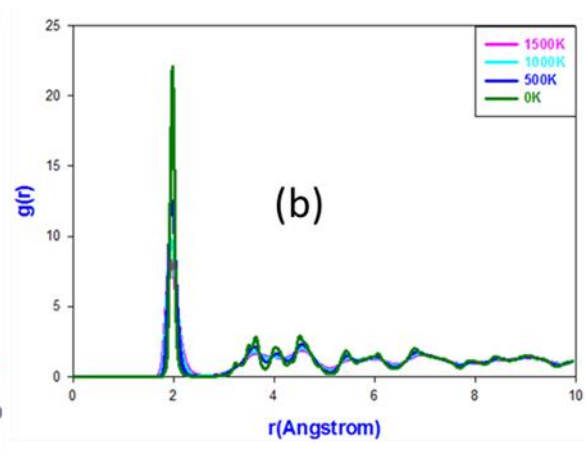
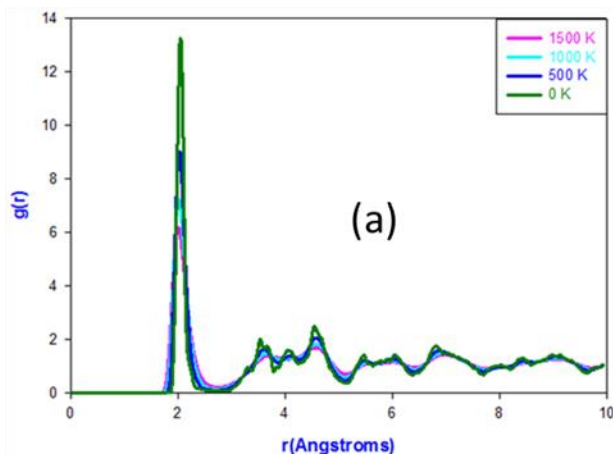
K.



B12: Total RDFs of the bulk TiO_2 with 0.07 Li ions after recrystallisation at 2000 K.



B13: Total RDFs of TiO_2 for the $\text{Ti}^{3+}-\text{O}^{2-}$ interaction at different temperatures, in a cooled nanoporous structure, with 0.04 Li ions.



B14: Total RDFs for the $\text{Ti}^{3+}-\text{O}^{2-}$ interaction at different temperatures, in the cooled bulk structure, with 0.04 Li ions.

